

LAKEHEAD UNIVERSITY

Piezoelectric Energy Harvesting with a Nonlinear Energy Sink

By

Yu Zhang

A THESIS

SUBMITTED TO THE FACULTY OF GRADUATE STUDIES
IN PARTIAL FULFILMENT OF THE REQUIREMENT FOR THE
DEGREE OF MASTER OF SCIENCE

MECHANICAL ENGINEERING

THUNDER BAY, ONTARIO

DECEMBER, 2016

© Yu Zhang 2016

ABSTRACT

Energy transfer from one system to another system, or vice versa, is happening constantly in many processes with various forms. Vibration in machines or structures can be considered as a form of energy transfer from a source to a receiver. In general, such vibration is unwanted. Vibration suppression is of importance in order to protect machines or structures. To monitor vibration of a large system such as building or bridge, a network of sensors is used. Supply of power to these sensors is challenging due to various difficulties such as accessibility or cost. Energy harvesting using ambient vibration is motivated to make sensors autonomous. Vibration energy can be converted into electric energy through electromagnetic transduction or piezoelectric effect. This research proposes a method to achieve simultaneous vibration suppression and energy harvesting in the broadband manner.

A nonlinear energy sink (NES) is a special vibration absorber that is capable of sinking or localizing vibration energy from a primary system. Unlike a linear or nonlinear vibration absorber, the NES's spring is essentially nonlinear. In this research, a variant NES is developed to achieve vibration suppression and energy harvesting in a broad frequency band. The developed apparatus consists of a fixed-fixed composite beam acting as the NES spring and two magnets attached at the middle of the beam acting as the NES mass. The composite beam is formed by a thin steel beam and two piezoelectric bimorphs attached at the ends of the steel beam. The piezoelectric bimorphs convert the NES vibration energy into electric one. The system modeling is presented. System identification is conducted to determine the parameter values. The transient behaviours of the system are investigated numerically and experimentally. It has shown that the developed apparatus demonstrates the characteristics similar to those of the NES. The harmonically forced responses of the system are examined. The approximate analytical solutions of the steady-state responses are derived. The Matcont is used to obtain the frequency responses plots for various cases. An experimental study has been conducted. Both the numerical solutions and experimental results show that the developed apparatus is capable of harvesting energy while suppressing vibration in a wide frequency band.

ACKNOWLEDGMENTS

First, I would like to express my sincere gratitude to my supervisor Dr. Kefu Liu who saw the potential in me and also encouraged me during the course of this research. His guidance helped me in all aspects including thesis research and writing. I could not have imagined having a better advisor and mentor for my master study.

I would like to also thank Kailash Batia for his assistance in the machine shop.

I would also like to thank my parents: Yurong Zhang, Heping Zhang, and Peter T. Fairchild for supporting me in the spiritual way throughout this study and thesis writing and also my life in general.

Table of Contents

ABSTRACT.....	i
ACKNOWLEDGMENTS	ii
Table of Contents	iii
List of Figures	v
List of Tables	x
Chapter 1 Introduction.....	1
1.1 Overview and motivation of the research	1
1.2 Literature review	4
1.2.1 Passive vibration absorption.....	4
1.2.2 Nonlinear energy sink.....	4
1.2.3 Energy harvesting.....	7
1.3 Objectives and contributions	9
1.4 Thesis outline.....	10
Chapter 2 Apparatus, modelling, and parameter identification.....	11
2.1 Apparatus	11
2.2 Modelling.....	13
2.3 System parameter identification	13
2.3.1 Primary system parameter identification.....	13
2.3.2 NES system parameter identification	15
2.4 Conclusion	19
Chapter 3 Transient responses.....	20
3.1 Introduction.....	20
3.2 Simulation results	20
3.3 Experimental results	26
3.4 Nonlinear normal mode analysis	31
3.5 Comparison of three systems.....	38
3.6 Conclusion	48

Chapter 4 Harmonically forced responses.....	49
4.1 Analytical solution of harmonically forced responses.....	49
4.2 Simulation results	55
4.2.1 Frequency response plot.....	55
4.2.2 Frequency sweeping direction.....	58
4.2.3 Interpretation of FRPs	59
4.2.4 Energy harvesting.....	62
4.3 Experiment results	64
4.4 Conclusion	70
Chapter 5 Conclusion	71
References.....	73
Appendix A.....	80

List of Figures

Figure 1.1 Schematic of two vibration problems: (a) transient response due to initial disturbance; (b) harmonic base excitation.	1
Figure 1.2 Transient response of the primary system: $x_p(0) = 0.003 \text{ m}$ and $\dot{x}_p(0) = 0 \text{ m/s}$, $m_p = 0.839 \text{ kg}$, $k_p = 3799.3 \text{ N/m}$, and $c_p = 1.129 \text{ Ns/m}$	2
Figure 1.3 Displacement ratio of system: $f_n = 10.71 \text{ Hz}$	3
Figure 1.4 Schematic of a NES attached to a primary system subjected to base excitation.....	5
Figure 2.1 Schematic of apparatus.....	12
Figure 2.2 Schematic of testing system	12
Figure 2.3 Experimental result of primary system: (a) Primary system free response with curve fitted damping curve; (b) FFT plot of free response $f_p = 10.71 \text{ Hz}$	15
Figure 2.4 Restoring force $F(z, \dot{z})$ vs. relative displacement z and relative velocity \dot{z}	16
Figure 2.5 Restoring force $F(z, 0)$ vs. displacement z (circle: measured data; line: fitted curved)	17
Figure 2.6 Restoring force $F(0, \dot{z})$ vs. velocity \dot{z} (circle: measured data; line: fitted curved).....	18
Figure 2.7 Piezoelectric energy harvester voltage vs. relative displacement $z = x_a - x_p$	19
Figure 3.1 Simulation results with $X = 0.52 \text{ mm}$: (a) displacements (Solid line: primary; Dotted line: NES), (b) the the percentage of instantaneous energy in NES, and (c) open circuit voltage of PEH.....	22
Figure 3.2 Wavelet transform spectra for simulation results with $X = 0.52 \text{ mm}$: (a) x_p and (b) x_a	22
Figure 3.3 Simulation results with $X = 1.42 \text{ mm}$: (a) displacements (Solid line: primary system; Dotted line: NES), (b) the percentage of instantaneous energy in NES, and (c) open circuit voltage of PEH.....	23
Figure 3.4 Wavelet transform spectra for simulation results with $X = 1.42 \text{ mm}$: (a) x_p and (b) x_a	23
Figure 3.5 Simulation results with $X = 2.65 \text{ mm}$: (a) displacements (Solid line: primary system; Dotted line: NES), (b) the percentage of instantaneous energy in NES, and (c) open circuit voltage of PEH.....	24

Figure 3.6 Wavelet transform spectra for simulation results with $X = 2.65$ mm: (a) x_p and (b) x_a	24
Figure 3.7 Simulation results with $X = 4.45$ mm: (a) displacements (Solid line: primary system; Dotted line: NES), (b) the percentage of instantaneous energy in NES, and (c) open circuit voltage of PEH.	25
Figure 3.8 Wavelet transform spectra for simulation results with $X = 4.45$ mm: (a) x_p and (b) x_a	25
Figure 3.9 Simulation results with $X = 4.45$ mm: (a) the percentage of instantaneous energy in NES, (b) accumulated energy in NES, and (c) ratio of accumulated energy in NES to maximum of kinetic energy of NES.	26
Figure 3.10 Testing apparatus setup	27
Figure 3.11 Experimental results with $X = 0.52$ mm: (a) displacements (Solid line: primary system; Dotted line: NES), (b) the percentage of instantaneous energy in NES, and (c) open circuit voltage of PEH.	27
Figure 3.12 Wavelet transform spectra for experimental results with $X = 0.52$ mm: (a) x_p and (b) x_a	28
Figure 3.13 Experimental results with $X = 1.42$ mm: (a) displacements (Solid line: primary system; Dotted line: NES), (b) the percentage of instantaneous energy in NES, and (c) open circuit voltage of PEH.	28
Figure 3.14 Wavelet transform spectra for experimental results with $X = 1.42$ mm: (a) x_p and (b) x_a	29
Figure 3.15 Experimental results with $X = 2.65$ mm: (a) displacements (Solid line: primary system; Dotted line: NES), (b) the percentage of instantaneous energy in NES, and (c) open circuit voltage of PEH.	29
Figure 3.16 Wavelet transform spectra for experimental results with $X = 2.65$ mm: (a) x_p and (b) x_a	30
Figure 3.17 Experimental results with $X = 4.45$ mm: (a) displacements (Solid line: primary system; Dotted line: NES), (b) the percentage of instantaneous energy in NES, and (c) open circuit voltage of PEH.	30
Figure 3.18 Wavelet transform spectra for experimental results with $X = 4.45$ mm: (a) x_p and (b) x_a	30
Figure 3.19 Experimental results with $X = 4.45$ mm: (a) the percentage of instantaneous energy in NES, (b) accumulated energy in NES, and (c) ratio of accumulated energy in NES to maximum of kinetic energy of NES.	31

Figure 3.20 Frequency energy plot: backbone curves $S_{11\pm}$	35
Figure 3.21 Frequency energy plots and wavelet transforms of relative displacement $x_a - x_p$ from the simulation results for $f_p = 10.71$ Hz: (a) low initial energy $X = 0.52 \times 10^{-3}$ (m); (b) medium initial energy $X = 1.42 \times 10^{-3}$ (m); (c) medium-high initial energy $X = 2.65 \times 10^{-3}$ (m) and; (d) high initial energy $X = 4.45 \times 10^{-3}$ (m).....	37
Figure 3.22 Frequency energy plots and wavelet transforms of relative displacement $x_a - x_p$ from the experimental results for $f_p = 10.71$ Hz: (a) low initial energy $X = 0.52 \times 10^{-3}$ (m); (b) medium initial energy $X = 1.42 \times 10^{-3}$ (m); (c) medium-high initial energy $X = 2.65 \times 10^{-3}$ (m) and; (d) high initial energy $X = 4.45 \times 10^{-3}$ (m).....	38
Figure 3.23 Simulation results of non-dimensional system: (a) the percentage of instantaneous energy in NES, (b) accumulated energy in NES, (c) ratio of accumulated energy in NES to maximum of kinetic energy in NES, and (d) ratio of accumulated energy in NES to total system energy, (solid blue line: $\eta = 0.3$ or $f_p = 15$ Hz, dash green line: $\eta = 0.5$ or $f_p = 9$ Hz, and red dotted line: $\eta = 1$ or $f_p = 4.5$ Hz).....	42
Figure 3.24 Experimental results of non-dimensional system: (a) the percentage of instantaneous energy in NES, (b) accumulated energy in NES, (c) ratio of accumulated energy in NES to maximum of kinetic energy in NES, and (d) ratio of accumulated energy in NES to total system energy, (solid blue line: $\eta = 0.3$ or $f_p = 15$ Hz, dash green line: $\eta = 0.5$ or $f_p = 9$ Hz).....	43
Figure 3.25 Frequency energy plot: backbone curves $S_{11\pm}$ for (a) $f_p = 9$ Hz, (b) $f_p = 15$ Hz.....	44
Figure 3.26 Frequency energy plots and wavelet transform of relative displacement $x_a - x_p$ from the simulation results for $f_p = 9$ Hz: (a) low initial energy $X = 0.52 \times 10^{-3}$ (m); (b) medium initial energy $X = 1.42 \times 10^{-3}$ (m); (c) medium-high initial energy $X = 2.65 \times 10^{-3}$ (m) and (d) high initial energy $X = 4.45 \times 10^{-3}$ (m).	45
Figure 3.27 Frequency energy plots and wavelet transforms of relative displacement $x_a - x_p$ from the experimental results for $f_p = 9$ Hz: (a) low initial energy $X = 0.52 \times 10^{-3}$ (m); (b) medium initial energy $X = 1.42 \times 10^{-3}$ (m); (c) medium-high initial energy $X = 2.65 \times 10^{-3}$ (m) and (d) high initial energy $X = 4.45 \times 10^{-3}$ (m).....	46
Figure 3.28 Frequency energy plots and wavelet transforms of relative displacement $x_a - x_p$ from the simulation results for $f_p = 15$ Hz: (a) low initial energy $X = 0.312 \times 10^{-3}$ (m); (b) medium initial energy $X = 0.852 \times 10^{-3}$ (m); (c) medium-high initial energy $X = 1.59 \times 10^{-3}$ (m) and (d) high initial energy $X = 2.67 \times 10^{-3}$ (m).....	47
Figure 3.29 Frequency energy plots and wavelet transforms of relative displacement $x_a - x_p$ from the experimental results for $f_p = 15$ Hz: (a) low initial energy $X = 0.312 \times 10^{-3}$ (m); (b) medium initial energy $X = 0.852 \times 10^{-3}$ (m); (c) medium-high initial energy $X = 1.59 \times 10^{-3}$ (m) and (d) high initial energy $X = 2.67 \times 10^{-3}$ (m).....	48

Figure 4.1 FRP for $A_y = 0.6 \text{ m/s}^2$ and $R = 1000 \Omega$: (a) primary displacement X_p and (b) relative displacement Z . Blue line indicates stable periodic orbits. Red lines are unstable indicating non-periodic orbits. Black squares are Hopf bifurcation points and green triangles are Limit points. Red circles are from numerical integration of Equations (4.1) to (4.3)	56
Figure 4.2 Time response of strongly modulated response with $A_y = 0.6 \text{ m/s}^2$, $R = 1000 \Omega$, and $\Omega = 10.58 \text{ Hz}$: (a) amplitudes by solving Equations (4.32) to (4.35) with Matcont; (b) reconstituted responses defined by Equations (4.36) and (4.37); (c) responses by numerically integrating Equations (4.1) to (4.3).....	58
Figure 4.3 FRPs obtained by forward frequency sweeping with $A_y = 0.6 \text{ m/s}^2$: arrows indicate the response path. (a) X_p/X_{pst} , (b) Z/X_{pst}	59
Figure 4.4 FRPs obtained by backward frequency sweeping with $A_y = 0.6 \text{ m/s}^2$: arrows indicate the response path. (a) X_p/X_{pst} , (b) Z/X_{pst}	59
Figure 4.5 Comparison of FRPs for two excitation levels at $R = 1000 \Omega$. Curve A obtained with $A_y = 1.8 \text{ m/s}^2$; curve B obtained with $A_y = 0.6 \text{ m/s}^2$. Green line represents the FRP of the primary system with NES detached.....	60
Figure 4.6 Comparison of FRPs for three excitation levels.....	60
Figure 4.7 Closed island and FRP at $A_y = 0.6 \text{ m/s}^2$. (a) X_p/X_{pst} , (b) Z/X_{pst} . Green line represents the primary system with NES detached.	61
Figure 4.8 Closed island and FRP at $A_y = 0.3 \text{ m/s}^2$. (a) X_p/X_{pst} , (b) Z/X_{pst} . Green line represents the primary system with NES detached.	61
Figure 4.9 Relative displacement and peak power at acceleration $A_y = 0.6 \text{ m/s}^2$. (a) FRP for relative displacement and (b) peak power as a function of frequency at $R = 0, 1000, 10^5, 10^7 \Omega$	63
Figure 4.10 Relative displacement and peak power with $A_y = 1.8 \text{ m/s}^2$. (a) FRP for relative displacement and (b) peak power as a function of frequency at $R = 0, 1000, 10^5, 10^7 \Omega$	64
Figure 4.11 Testing apparatus setup	65
Figure 4.12 Comparison of the analytic T.R. and experimental T.R. of the primary system with $A_y = 0.6 \text{ m/s}^2$	66
Figure 4.13 Test results with $A_y = 0.6 \text{ m/s}^2$ and $R = 1000 \Omega$. (a) X_p/X_{pst} , blue line indicates the experiment results with the NES removed; (b) Z/X_{pst} ; (c) the average harvested power. (Red circle: forward frequency sweeping; Blue square: backward frequency sweeping.)...	66
Figure 4.14 Test results with $A_y = 0.6 \text{ m/s}^2$ and $R = 2000 \Omega$. (a) X_p/X_{pst} , blue line indicates experiment results with NES removed; (b) Z/X_{pst} ; (c) the average harvested power. (Red circle: forward frequency sweeping; Blue square: backward frequency sweeping.).....	67

- Figure 4.15 Experiment results of displacement response at acceleration $A_y = 0.6 \text{ m/s}^2$ and $R = 2000 \Omega$ and excitation frequency $\Omega = 12 \text{ Hz}$ 68
- Figure 4.16 Test results with $A_y = 1.2 \text{ m/s}^2$ and $R = 1000 \Omega$. (a) X_p/X_{pst} , blue line indicates experiment results with NES removed; (b) Z/X_{pst} ; (c) the average harvested power. (Red circle: forward frequency sweeping; Blue square: backward frequency sweeping.)..... 69
- Figure 4.17 Test results with $A_y = 1.8 \text{ m/s}^2$ and $R = 1000 \Omega$. (a) X_p/X_{pst} , blue line indicates experiment results with NES removed; (b) Z/X_{pst} ; (c) the average harvested power. (Red circle: forward frequency sweeping; Blue square: backward frequency sweeping.)..... 70

List of Tables

Table 2.1 Parameters of NES.....	12
Table 2.2 Estimated parameter values of the primary system	15
Table 4.1 Initial condition for Matcont time domain (P_O) simulation.....	62
Table 4.2 Steady-state point for Matcont equilibrium (EP_EP) simulation.	62

Chapter 1 Introduction

1.1 Overview and motivation of the research

The motivation of this research is to study the behaviour of Piezoelectric Energy Harvester (PEH) coupled with a Nonlinear Energy Sink (NES) that is used to perform vibration reduction along with energy harvesting. Vibration can be caused by numerous ways, such as earthquake, unbalanced mass of rotating machines, or impulsive forces. This undesirable vibration can result in structural damages, machine failures, and human being discomfort. Therefore, it is very important to suppress vibration.

Energy harvesting approaches that transform this vibrational kinetic energy to electrical energy offering the potential of renewable power sources which can be used to directly replace or augment the battery in wireless sensor applications. Such renewable energy sources could reduce environmental impact of disposable batteries. Kinetic energy is typically converted into electric energy by electromagnetic, electrostatic, or piezoelectric transduction mechanisms [1, 2]. In this research, piezoelectric energy harvesting coupled with a nonlinear energy sink is proposed.

Two common problems occurring in machines and structures are dealt with: (a) the transient response of the system and (b) the harmonically forced response of the system. Figure 1.1 shows that the general schematic of these two vibration problems where $x_p(t)$ is the displacement of primary system, m_p , k_p and c_p are the mass, stiffness and the damping coefficient of the primary system.

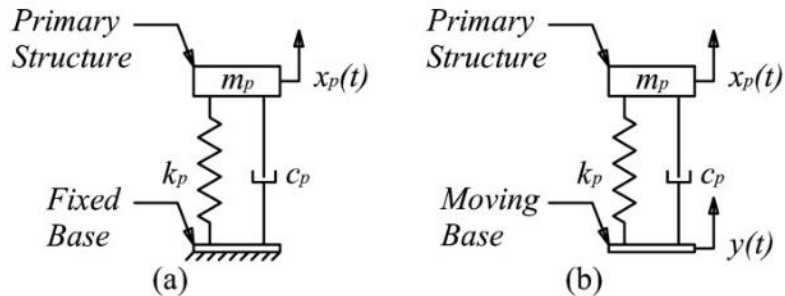


Figure 1.1 Schematic of two vibration problems: (a) transient response due to initial disturbance; (b) harmonic base excitation.

For the system that is demonstrated in Figure 1.1(a), the equation of motion is defined by Equation (1.1),

$$\begin{cases} m_p \ddot{x}_p + c_p \dot{x}_p + k_p x_p = 0 \text{ or } \ddot{x}_p + 2\zeta\omega_n \dot{x}_p + \omega_n^2 x_p = 0 \\ x_p(0), \dot{x}_p(0) \end{cases} \quad (1.1)$$

$$\omega_n = \sqrt{\frac{k_p}{m_p}} \quad (1.2)$$

where x_p , \dot{x}_p , \ddot{x}_p are the displacement, velocity, and acceleration of the primary mass. m_p , k_p and c_p are the mass, stiffness, and the damping coefficient of the primary system. ζ and ω_n are the damping ratio and natural frequency of the primary system respectively.

Figure 1.2 shows a typical transient response for the system with a low damping ratio. As the damping is low, it takes a long time for the response to die out. This extended duration of vibration is not desirable. Therefore, the goal of vibration control is to suppress this oscillation and settle the mass in a much quicker manner.

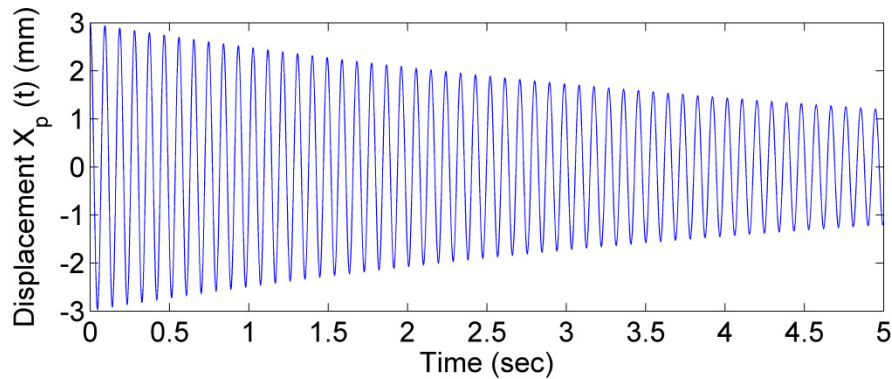


Figure 1.2 Transient response of the primary system: $x_p(0) = 0.003 \text{ m}$ and $\dot{x}_p(0) = 0 \text{ m/s}$, $m_p = 0.839 \text{ kg}$, $k_p = 3799.3 \text{ N/m}$, and $c_p = 1.129 \text{ Ns/m}$

The equations of motion for the second type of problem shown in Figure 1.1(b) is given by,

$$\begin{cases} m_p \ddot{x}_p + c_p \dot{x}_p + k_p x_p = k_p y + c_p \dot{y} \\ y = Y \cos(\Omega t) \end{cases} \quad (1.3)$$

where Ω is the harmonic base excitation frequency. In this scenario, the initial force due to the base acceleration becomes an exciting force applied to the primary mass. The steady-state response of the system is concern. Because of the low damping coefficient of the system, vibration displacement of the primary mass tends to attenuate for extended period of time. Figure 1.3 shows the displacement ratio of amplitude of x_p over excitation amplitude Y for the system having natural frequency $f_n = 10.71$ Hz.

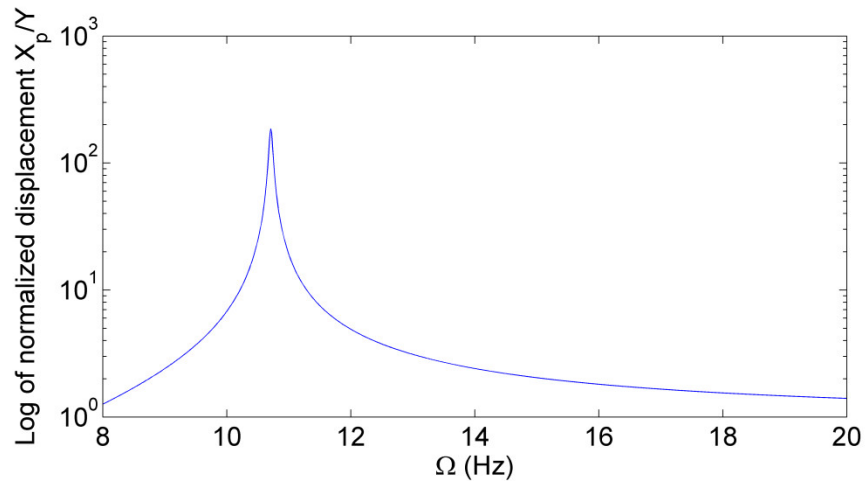


Figure 1.3 Displacement ratio of system: $f_n = 10.71$ Hz

In Figure 1.3, it can be seen that when the excitation frequency approaches the natural frequency of the system, the displacement ratio is greatly increased. And, it reaches a peak when the excitation frequency equals to the natural frequency of the system. This is known as the resonance. The suppression of harmonically forced responses is one of the major objectives of this research.

With the vibration problem identified, it draws attention to investigate at a different view angle and explore if there are any benefits of this. The cause of any vibration in either transient or steady-state case is the energy added into the system. This added energy could be harvested. This research intends to explore a way of achieving simultaneous vibration suppression and energy harvesting.

1.2 Literature review

1.2.1 Passive vibration absorption

Passive attenuation method presents an approach to control undesired vibrations [3, 4, 5, 6]. One particular method is to use passive vibration absorbers which has been studied in the past and widely used in vibration control. Passive vibration absorbers consist of a mass attached to a structure via a spring or a combination of spring and damper. Passive vibration absorbers are often constructed with elastomeric materials installed between the structure and a proof mass. The primary goal of passive vibration absorbers is to increase the effective dynamic stiffness of a structure over a narrow frequency range. In practice, passive vibration absorbers are typically used at a specific frequency to minimize vibration. The advantage of using passive vibration absorbers are low cost, low weight, and easy setup. The limitation of passive vibration absorbers is that it is only effective at a single frequency. By adding a passive vibration absorber, the combined system now has two degree of freedom and two natural frequencies [7, 8]. If the external excitation frequency changes, the structure will have amplified vibrations at those two natural frequencies. In this research, passive vibration absorbers are not main focus.

1.2.2 Nonlinear energy sink

In the past, nonlinear energy sink (NES) has been studied and researched [9, 10, 11]. In contrary to a linear vibration absorber, a NES consists of a small mass, a linear damper, and a spring which has only essential nonlinear stiffness, and it is attached to a linear primary structure shown in Figure 1.4.

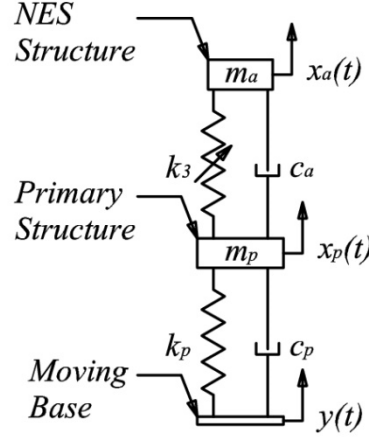


Figure 1.4 Schematic of a NES attached to a primary system subjected to base excitation.

In comparison to a nonlinear vibration absorber, the nonlinear stiffness of the NES does not possess a linear stiffness term [12]. From Figure 1.4, the equations of motion are formulated in Equation (1.4) below. Note that it has a nonlinear stiffness term k_3 and lacks of a linear stiffness term k_1 . In this research, the nonlinear restoring force is approximated as a cubic function $F = k_1x + k_3x^3$ to provide smooth fitting from parameter identification experiment data, and yet it provides a strong nonlinearity.

$$\begin{cases} m_p \ddot{x}_p + c_p \dot{x}_p + k_p x_p - \left[c_a (\dot{x}_a - \dot{x}_p) + k_3 (x_a - x_p)^3 \right] = k_p y + c_p \dot{y} \\ m_a (\ddot{x}_a - \ddot{x}_p) + (1 + \mu) \left[c_a (\dot{x}_a - \dot{x}_p) + k_1 (x_a - x_p) + k_3 (x_a - x_p)^3 + \frac{\theta^2}{C^S} (x_a - x_p) \right] \\ - \mu [c_p \dot{x}_p + k_p x_p] = 0 \end{cases} \quad (1.4)$$

A previous research [13, 14] examined the behaviours of a linear primary structure attached with an essential nonlinear system. And, it showed the effectiveness of such a setup to absorb vibration energy in passive way from the linear primary structure. This energy transfer is defined as energy pumping which is defined as an irreversible transfer of energy from a linear or linearized structure to a nonlinear energy sink (NES) with relatively small mass [15], and it is caused by internal 1:1 resonance. The internal 1:1 resonance is a special case that a nonlinear oscillator matches its own oscillation frequency to the oscillation frequency of the linear primary structure. And, energy pumping is also explained as a

controlled one-way energy channelling in an irreversible manner. This phenomenon is considered as transferring vibration energy to a passive nonlinear “sink”, and the transferred energy is localized and dissipated due to damping effect. Hence, this leads such a device named nonlinear energy sink (NES). In [16], analytical analysis was conducted to further examine the energy channelling and 1:1 resonance. The study compared the NES with the traditional TMD, and showed that the former has a better performance and robustness than the latter. This stored energy in NES can be utilized by incorporating electrical circuits [17, 18, 19] for an optimized power output.

In [20, 21], the phenomenon of one-way energy transfer was referred to as targeted energy transfer (TET). An essential nonlinear oscillator is attached to a linear primary structure to reduce the vibration. This results in transferring the vibrational energy to the essential nonlinear oscillator. The study in [20, 21] explained the reason for the benefit and robustness of the NES as lacking a dominant natural frequency due to absence of a linear stiffness. In consequence, a certain initial energy level is required to set the NES into nonlinear oscillation in the transient response scenario. This implies that there is an energy threshold for the effectiveness of NES. In [22], a detailed study of the TET for the transient response was carried out in order to determine the effectiveness of the TET. Three different initial energy levels were defined to examine the effectiveness. It was found that the TET would not occur under low initial energy level. Thus, only a fraction amount of energy is transferred to NES and get dissipated. As the initial energy level increases, the TET occurs and the NES is able to dissipate between 90% to 95% of the total initial energy. Further increasing to high initial energy level, the TET still occurs but its effectiveness decreases. The NES could still dissipate a large portion of the total energy. The study in [22] showed that the design of NES was not pre-tuned or with a-priori knowledge. In [23], the design criteria of the NESs were extensively discussed in order to achieve the optimal performance by adjusting the mass, nonlinear stiffness, and the damping of the NES under a known initial input energy level.

In [9, 24, 25], an analytical solution for a NES attached to a linear structure was derived and three types of responses were investigated namely: common steady-state response, weakly modulated response, and strongly modulated response (SMR). A complexification averaging method is used to perform analysis to these responses in [22]. The dynamics of the system are

divided into two scales as slow time scale and fast time scale. Both the primary and NES systems are assumed in 1:1 resonance. The complexification averaging method is used to find saddle nodes and Hopf bifurcation nodes to represent the resulting equations [22]. A frequency response plot (FRP) is plotted to see system's response in wider frequency range. Similarly, saddle bifurcation nodes are found during the FRP and indicate that there exist multiple periodic solutions. The areas between the Hopf bifurcation nodes indicate a strongly modulated response, and this SMR is related to a called relaxation oscillation. The SMR can be considered as a part of repetitive TET under harmonic forcing.

NES has been proven in both theories and experimentally, but it is difficult to achieve zero linear stiffness. The NES proposed in [26] was achieved by attaching two coil springs to a mass that sits on a linear rail track. The other ends of both the coil springs were pivoted to the primary structure. When the springs are free of tension or compression, the setup results in an essential nonlinear stiffness. In [26], it presented a NES setup and demonstrated good experiment results which confirm with theoretical results. In [27, 28, 29], another approach of achieving an essential nonlinear stiffness was proposed in which two thin steel wires with zero tension were used. And, experiments of this approach of NES shows a good match to the theory. It has also shown the initial energy threshold exists in order for TET to occur. In [30], harmonic excitation is examined using the same device, however, experiment results are different from theoretical results. And, system consists of periodic solutions with noted saddle bifurcation nodes. It was also found that the experiment results differ from the theoretical results due to difficulty of modeling cubic stiffness, and this also leads to the difference in response amplitude.

1.2.3 Energy harvesting

The exciting potential to implement energy-autonomous portable electronics such as wireless sensors has attracted numerous research interests in vibration energy harvesting in recent years [31, 32]. Current solutions for vibration-to-electricity transduction are mostly accomplished via electrostatic, electromagnetic, or piezoelectric methods. Regardless of the conversion mechanisms, most of the harvesters are designed as linear oscillators as they provide large-amplitude responses when excited at resonance. However, linear resonant harvesters are

susceptible to a reduction in performance if the excitation conditions vary from the ideal sinusoidal form and resonant frequency.

Various methods have been attempted to address this issue. The natural frequency of tunable harvesters can be varied to resonate with varying frequency excitation [33, 34, 35, 36]. Tuning can be done on open-loop or closed-loop configurations. These harvesters have a more complex design and a low overall efficiency. A summary of the pros and cons of tunable harvesters can be found in [37]. A multimodal energy harvester is a multiple degree-of-freedom (DOF) system or distributed parameter system that is capable of resonating at multiple exciting frequencies. As multimodal energy harvesters do not require tuning, they are much easier to implement than the tunable counterparts [38, 39, 40, 41, 42, 43].

Nonlinear energy harvesters have attracted increasing attention as they offer some promising features [41, 42, 43, 44, 45, 46]. Nonlinear energy harvesters are usually classified as mono-stable and bi-stable harvesters. In the mono-stable system, the potential energy function of the system has a sole stable equilibrium state in the potential energy function, while in the bi-stable system, there are two stable equilibria separated by a potential barrier (an unstable saddle). The studies have shown that mono-stable devices have a large bandwidth over which the significant power can be harvested due to the bending in the resonant peak. However, the multi-value and jump phenomenon due to nonlinearity implies that its broadband feature is not guaranteed. For a bi-stable system, when excited by sufficient energy, it will overcome the potential barrier and escapes from one potential well to the other. This non-resonant behaviour permits coupling between the ambient excitation and the harvesters over a wide range of frequencies. Bi-stable oscillators may exhibit low-energy intrawell vibrations or periodic interwell vibrations. It has been shown that, when engaged in the periodic interwell vibrations or high-energy orbits, a bi-stable device can dramatically improve energy harvesting performance [46, 47].

There have been some reported attempts to employ the NES for energy harvesting. [48] presented an analytical study on the use of the NES for simultaneous vibration suppression and energy harvesting. The NES mass is attached to a vibrating host system and coupled with an electromagnetic energy harvester so that its effect can be represented by an

electromechanically induced damping term. The study found that the use of the NES for harvesting energy is advantageous as it does not require tuning and is suitable for low-level broadband vibration sources. [49, 50] extended their investigation to the performance of piezoelectric energy harvesting using essential nonlinearity and compared to the linear counterparts. However, these efforts focus on the dynamics and energy harvesting performance of the NES itself, instead of the behaviour of the NES coupled to a primary system. In [51], it has shown research and investigation of an energy harvesting system composed of two oscillators coupled with essential stiffness nonlinearity and subject to impulsive loading. Their conceptual design of the harvester consists of a piezoelastic cable attached to an oscillating mass. Due to the geometric/kinematic mechanical effects, the piezoelastic cable generates nonlinearized cubic stiffness nonlinearity. However, the design feasibility remains to be validated experimentally. In [52], it reported a conceptual study in the vibration control and energy harvesting for a free-free beam coupled with a piezoelectric energy harvesting NES. However, no prototype design and experimental study were presented. Another attempt was made to utilize the principle of the NES for simultaneous vibration suppression and energy harvesting by [53]. Different from the previous NES designs, the proposed device was not essentially nonlinear. Instead, it possessed a hardening spring in which its linear stiffness is made much lower than the stiffness of the primary system. Retaining this linear stiffness was necessary in order to minimize mechanical damping, which is a must for energy harvesting. The study showed that the apparatus behaved similarly as the NES and was capable of harvesting vibration energy while suppressing vibration of the primary system.

1.3 Objectives and contributions

From the previous literature review, it is noted that there have been few reports on experimental study of simultaneous vibration suppression and energy harvesting by employing the NES principle and piezoelectric energy harvesting. This study is motivated by combining the NES principle and piezoelectric energy harvesting to localize vibration energy in the NES and convert it into electrical energy via direct piezoelectric effect. In this way, the NES acts as both a vibration absorber and a piezoelectric energy harvester (PEH). The novelty of this study is

twofold: the use of no essential nonlinear spring to obtain the performance of the NES and the experimental validation of the numerical results.

The objectives of this study are as follows: (1) to develop an apparatus that possesses the NES characteristics for vibration suppression and energy harvesting; (2) to identify the system parameters; (3) to investigate the transient responses of the system; (3) to investigate the steady-state responses of the system subject to a harmonic base motion.

1.4 Thesis outline

The thesis is divided into the following chapters. Chapter 2 first presented the proposed apparatus and its modeling. Then it addressed parameter identification. Chapter 3 focused on the transient behaviours of the system. Numerical simulations of transient responses were carried out and the results were verified by an experimental study. A nonlinear normal mode (NNM) analytic study were performed to unveil the energy dependency of the NES under transient response. Chapter 4 focused on the harmonic excitation system response. The approximate steady-state responses were derived using a mixed Multiple scale/harmonic balance method. Then the frequency response plots were found via a continuation package Matcont. An experimental study was conducted. Chapter 5 summarized the findings of this research and present suggestions for the future study.

Chapter 2 Apparatus, modelling, and parameter identification

2.1 Apparatus

To investigate the performance of the PEH based on the NES, an apparatus is developed, which comprises three parts: a base, a primary system, and an energy harvesting NES. Figure 2.1 shows the schematic of the developed apparatus. The base is a slip table mounted on a pair of linear bearings which sit on a linear track. The primary system consists of a platform supported by two steel plates. The lower ends of the steel plates are fastened to the base. The NES consists of a fixed-fixed composted beam and two magnets. The composite beam, acting as the NES spring, is formed by a thin steel beam (1) and two piezoelectric bimorphs (MIDE Volture V21BL) (2). Piezoelectric bimorphs act as energy transduction components. The two magnets are attached to the middle of the beam by their own magnetic force, acting as the NES mass. The NES beam is fixed to a rigid cage that is fastened to the platform. The NES beam is axially prepressed so that it is slightly buckled. This will greatly reduce the linear stiffness of the NES spring to achieve quasi essentially nonlinear stiffness. In order to avoid a bi-stable configuration, another magnet is held by a bracket fixed to the platform and positioned collinearly to the oscillating magnets in a repelling manner. By adjusting the distance between this magnet and the oscillating magnets, the oscillating magnets (NES mass) are kept to the zero position. Two laser reflex sensors (RF) (Wenglor model CP24MHT80) are used to measure the displacement of the NES mass, the primary mass and the base, respectively. Key physical parameters are listed in Table 2.1.

Figure 2.2 shows the schematic of the testing system. The base is driven by a Brüel & Kjær shaker (model 2809) through a stinger. The shaker is driven by a Brüel & Kjær power amplifier (model 2718). A computer with dSPACE dS1104 data acquisition board is used to collect sensor data and voltage output across a variable load resistor and mean while send voltage signal to the power amplifier to drive the shaker. The control program is developed using Matlab Simulink which is interfaced with dSPACE ControlDesk Desktop software.

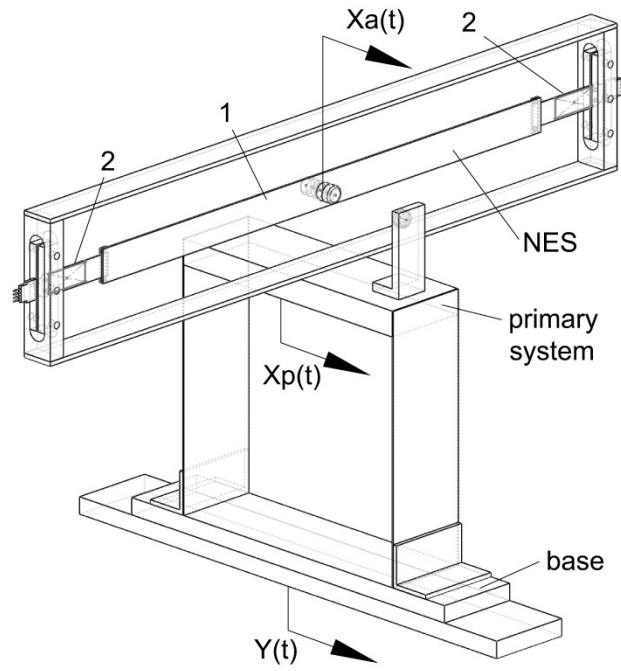


Figure 2.1 Schematic of apparatus

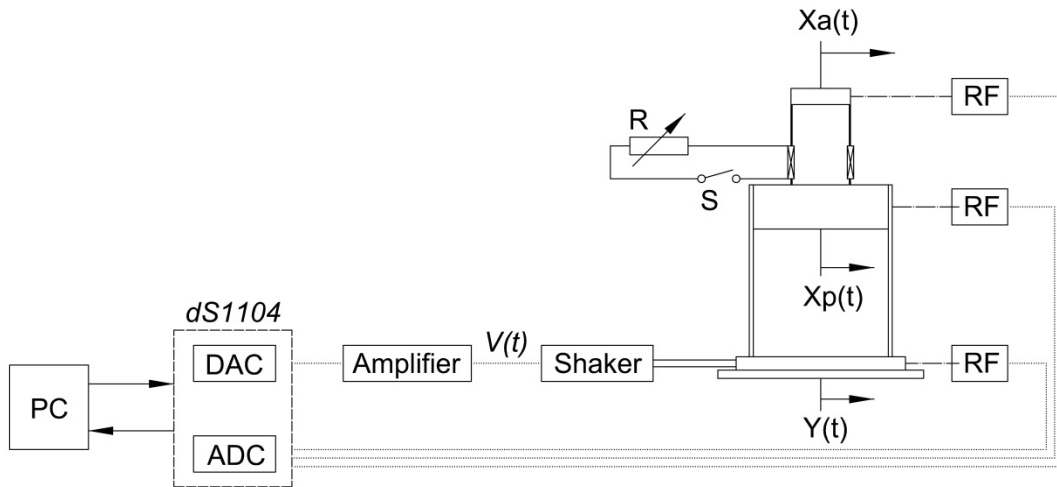


Figure 2.2 Schematic of testing system

Table 2.1 Parameters of NES

Beam		Oscillating magnet		Repelling magnet	
Length (mm)	393	Length (mm)	25.4	Length (mm)	3.175
Width (mm)	30	Width (mm)	12.7	Diameter (mm)	12.7
Thickness (mm)	0.52	Height (mm)	12.7	Material type	NdFeB (N40)
		Material type	NdFeB (N40)	Material type	NdFeB (N40)

2.2 Modelling

As shown in Figure 2.1, $x_p(t)$ and $x_a(t)$ represent the displacement of the primary mass and the NES mass, respectively, and $y(t)$ represents the displacement of the base. The governing equations of motion are given below,

$$m_p \ddot{x}_p + c_p (\dot{x}_p - \dot{y}) + k_p (x_p - y) - [c_a \dot{z} + (k_1 z + k_3 z^3) + \theta V] = 0 \quad (2.1)$$

$$m_a \ddot{z} + (1 + \mu) [c_a \dot{z} + (k_1 z + k_3 z^3) + \theta V] - \mu [c_p (\dot{x}_p - \dot{y}) + k_p (x_p - y)] = 0 \quad (2.2)$$

$$\frac{V}{R} + C^S \dot{V} - \theta \dot{z} = 0 \quad (2.3)$$

where m_p , c_p and k_p are the mass, the damping coefficient, and the stiffness of the primary system, respectively; m_a and c_a are the mass and damping coefficient of the NES, respectively, k_1 and k_3 are the linear stiffness and nonlinear stiffness of the NES spring, respectively; $z = x_a - x_p$ is the relative displacement between the NES mass and primary mass; $\mu = m_a / m_p$ is the mass ratio; parameter θ is the electromechanical coupling coefficient of the PEH and identified in Section 2.3.2 NES system parameter identification; V is the voltage across the resistive load R and C^S is the capacitance of the PEH. When the parallel connection is used, $C^S = 83.5 \times 10^{-9}$ F from the datasheet of piezoelectric transducer (MIDE Volture V21BL).

2.3 System parameter identification

2.3.1 Primary system parameter identification

The mass of the primary system is found to be $m_p = 0.839$ kg. The spring of the primary system is approximated as a linear spring. To determine its stiffness, the primary mass is set into free oscillation by an initial displacement. The response is recorded, and a Fast Fourier Transform (FFT) is applied. The natural frequency of the primary system is found to be 10.71 Hz. Under the assumption of a linear spring, the primary structure spring stiffness k_p is determined by the following equation:

$$k_p = \omega_p^2 m_p \quad (2.4)$$

The result is found to be $k_p = 3799.3$ N/m.

The damping coefficient is estimated using the logarithmic decrement method [7]. Figure 2.3 shows a typical free response of the primary mass. By measuring all the peak values, the damping ratio can be obtained by the following equations

$$\delta = \frac{1}{n} \ln \left(\frac{x(t)}{x(t+nT)} \right) \quad (2.5)$$

$$\zeta = \frac{\delta}{\sqrt{4\pi^2 + \delta^2}} \quad (2.6)$$

Where $x(t)$ is the first peak of the response, $x(t+nT)$ is the n^{th} peak of the response, and ζ is the damping ratio. The damping ratio is found to be $\zeta = 0.01$. The damping coefficient is found to be $c_p = 1.129$ Ns/m by using the following equation,

$$c_p = 2\zeta\omega_p m_p \quad (2.7)$$

All the parameters of the primary system are tabulated in Table 2.2.

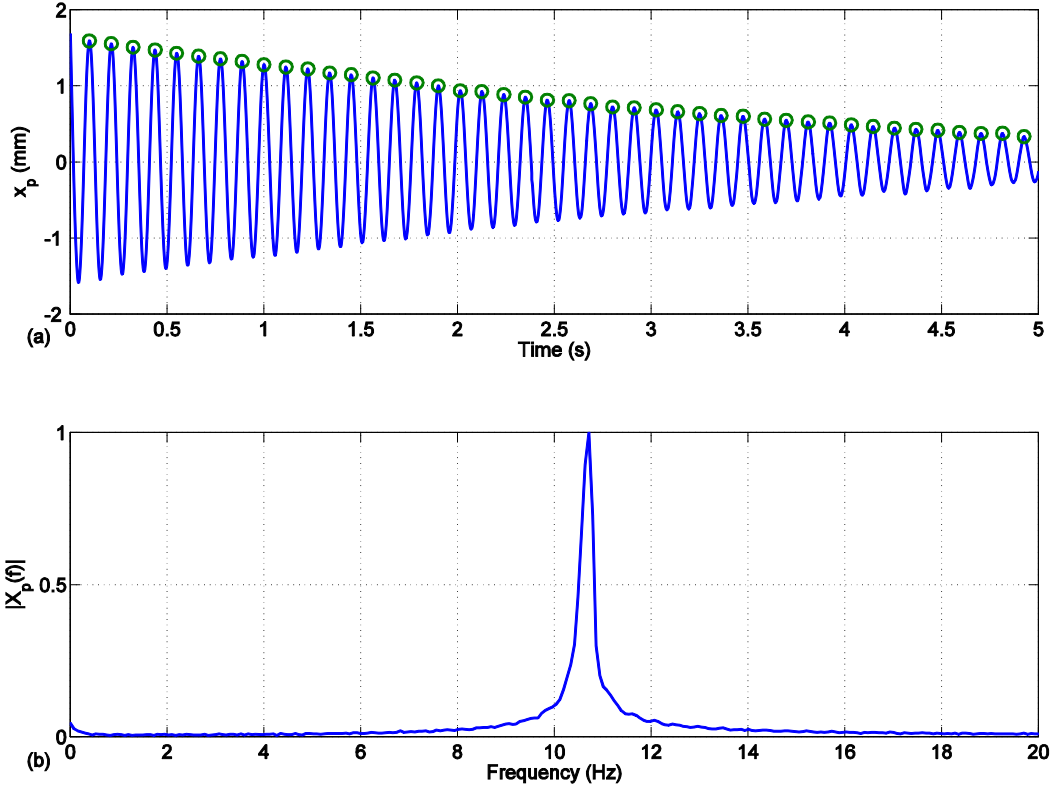


Figure 2.3 Experimental result of primary system: (a) Primary system free response with curve fitted damping curve; (b) FFT plot of free response $f_p = 10.71$ Hz

Table 2.2 Estimated parameter values of the primary system

Parameter	Estimated value
m_p	0.839 kg
k_p	3799.3 N/m
c_p	1.129 Ns/m
f_p	10.71 Hz

2.3.2 NES system parameter identification

To identify the restoring force of the NES spring, the equation of motion governing the NES system can be rewritten as,

$$F(z, \dot{z}) = -m_a \ddot{x}_a \quad (2.8)$$

where $F(z, \dot{z}) = c_a \dot{z} + k_1 z + k_3 z^3 + \theta V$. The NES mass is easily found to be $m_a = 0.0307$ kg. If \ddot{x}_a , \ddot{z} , and \dot{z} are available at discrete time interval k with a sampling time Δt , then a force surface can be generated using the method described in [54, 55]. To do this, the two side plates supporting the primary system mass are removed and the platform with the NES is fastened to the slip table directly. To fully excite the NES, the following slowly modulated periodic signal is used to perform this excitation,

$$y(t) = Y \cos(0.1\pi t) \cdot \cos(20\pi t) \quad (2.9)$$

where excitation amplitude is equal to $Y = 0.0005$ m.

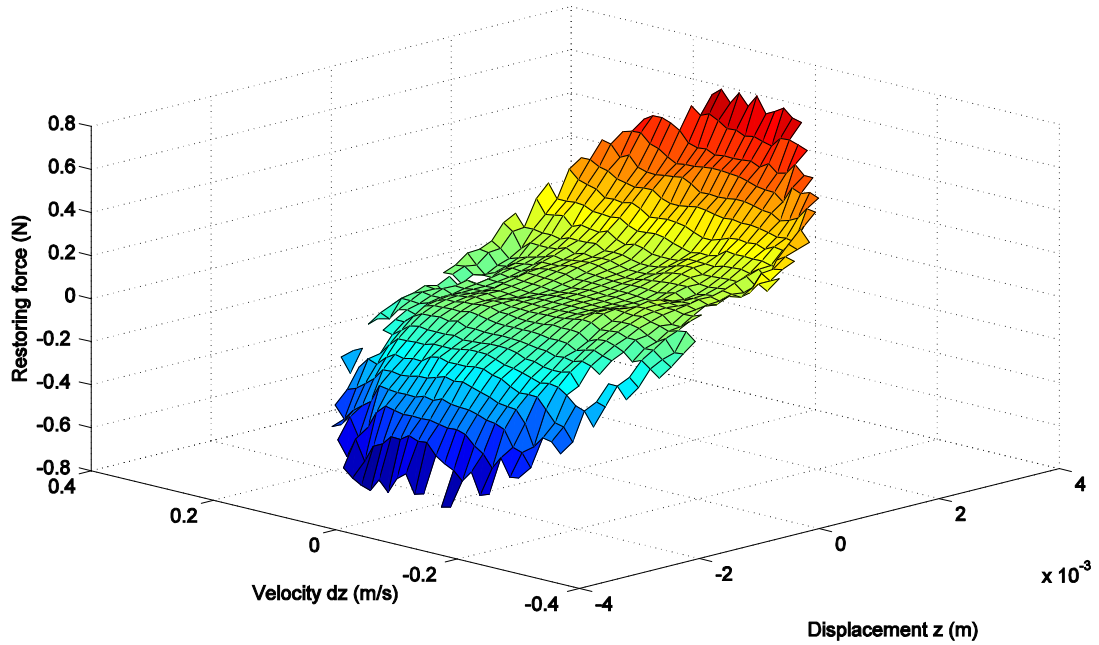


Figure 2.4 Restoring force $F(z, \dot{z})$ vs. relative displacement z and relative velocity \dot{z}

The displacements x_a and y are measured through the laser reflex sensors. Note that the $z = x_a - y$ in this case. The velocity and acceleration data are obtained by numerical differentiation. Figure 2.4 shows that the force surface obtained. It clearly shows that the NES spring possesses a nonlinear stiffness. As the displacement z increases, the restoring force F increases in a nonlinear manner. Figure 2.4 also shows that the NES has low mechanical damping as the force surface is quite flat at $z = 0$ plane along the velocity \dot{z} axis.

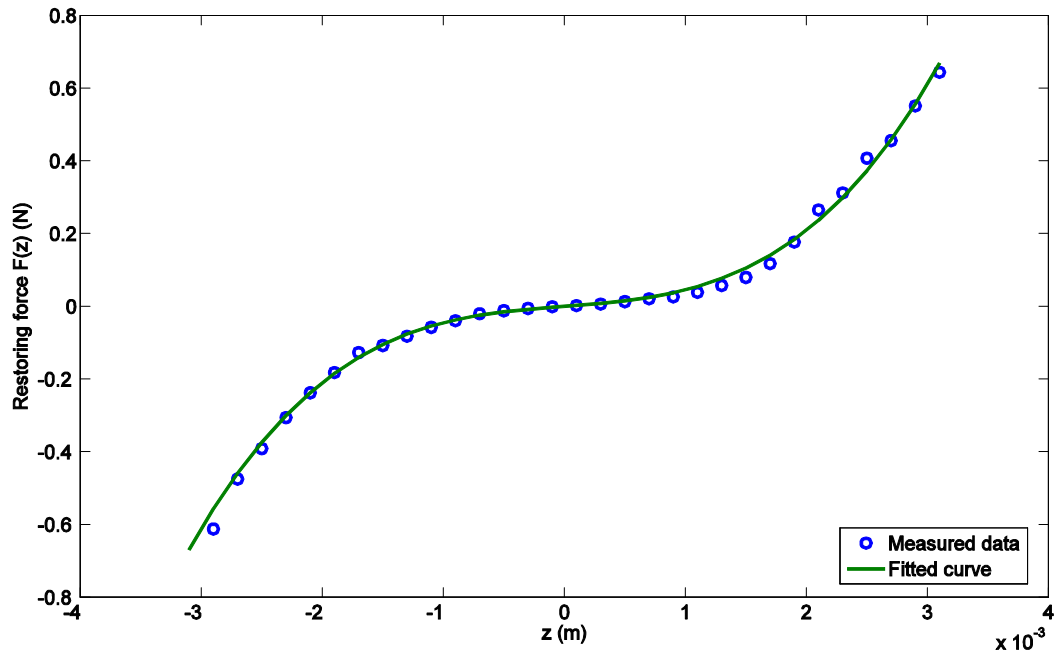


Figure 2.5 Restoring force $F(z, 0)$ vs. displacement z (circle: measured data; line: fitted curved)

On the section $\dot{z} = 0$, the restoring force is assumed to have the following format: $F(z, 0) = k_1 z + k_3 z^3 + \theta V$. In Figure 2.5, circles represent the values on this section. By applying short circuit condition, $V = 0$, and thus the term θV disappears. This leads the restoring force to $F(z, 0) = k_1 z + k_3 z^3$. By using this cubic function to curve-fit the points (circles) in Figure 2.5, it is found that $k_1 = 25.53 \text{ N/m}$ and $k_3 = 1.979 \times 10^7 \text{ N/m}^3$.

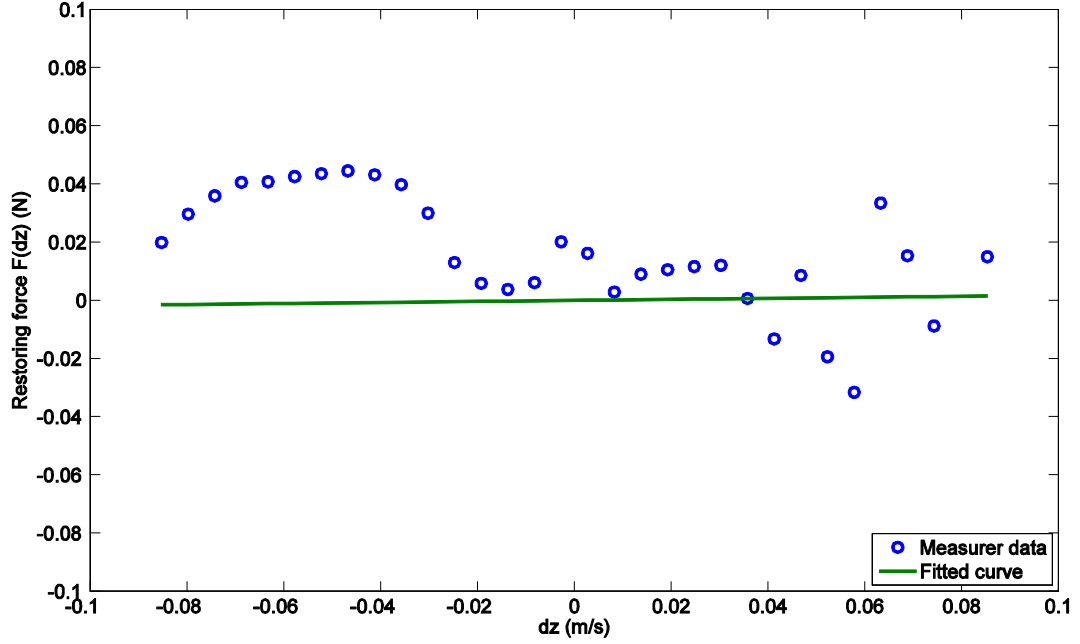


Figure 2.6 Restoring force $F(0, \dot{z})$ vs. velocity \dot{z} (circle: measured data; line: fitted curved)

On the section $z = 0$, the damping force is assumed to have the following format: $F(0, \dot{z}) = c_a \dot{z} + \theta V$. In Figure 2.6, circles represent the values on this section. By applying short circuit condition, $V = 0$, and thus the term θV disappears. This leads the damping force to $F(0, \dot{z}) = c_a \dot{z}$. By curve-fitting, it is found that $c_a = 1.770 \times 10^{-2}$ Ns/m .

The electromechanical coupling coefficient θ is a direct link between the mechanical system and piezoelectric system. The experiment is conducted to estimate this electromechanical coupling coefficient [19]. By setting the piezoelectric energy harvester into open circuit condition or $R = \infty$, Equation (2.3) becomes.

$$\dot{V} = \frac{\theta}{C^S} \dot{z} \quad (2.10)$$

By integrating Equation, it yields

$$V = \frac{\theta}{C^S} z + C \quad (2.11)$$

where C is the integration constant that is zero if the PEH is perfectly symmetric. An experiment is conducted to measure the relationship between the open-circuit voltage of the PEH and the deflection. Figure 2.7 shows the measured voltage values in a closed curve and the fitted curve in solid line with circle markers. By curve-fitting these values, the constant $\theta/C^S = 1.5521 \times 10^3$ is obtained. With the known value of C^S , the electromechanical coupling coefficient is found to be $\theta = 12.96 \times 10^{-5}$ N/V.

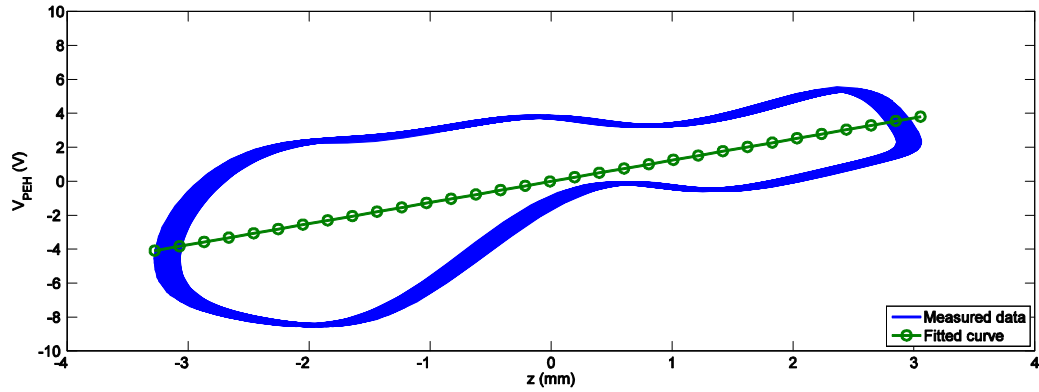


Figure 2.7 Piezoelectric energy harvester voltage vs. relative displacement $z = x_a - x_p$

2.4 Conclusion

An apparatus has been developed for the purpose of using the nonlinear energy sink to achieve the vibration suppression and energy harvesting. The system modeling has been addressed. A parameter identification has been conducted. The key findings are as follows. The NES spring possesses a cubic nonlinearity consisting of a linear term and nonlinear term. By compressing the NES beam axially, the linear term can be minimized so that the NES's natural frequency is much smaller than the primary system's one. Therefore, the NES system is weakly coupled to the primary system. It has been shown that the electromechanical coupling coefficient θ is a link between the mechanical system and electric system.

Chapter 3 Transient responses

3.1 Introduction

From the previous studies, it has been found that the NES possesses a good performance and effectiveness of vibration absorption when system responses are induced by initial disturbances [13, 15, 56, 57, 58]. This effectiveness of vibration absorption is achieved by the targeted energy transfer (TET). During the process of TET, vibration energy is transferred to the NES and is localized. This localized energy in the NES is then dissipated through damping. In the case of energy harvesting, the localized energy is converted to electrical energy that is dissipated through the load resistors. One of the important features of TET is 1:1 resonance. In this case, the NES is oscillating at the frequency of the primary system, resulting efficient energy transfer.

As the NES does not possess linear stiffness, it is capable of 1:1 resonance capture such that it can respond to a wide bandwidth of frequencies. As shown in Chapter 2, the proposed apparatus is not a true NSE as it has a hardening spring. The previous studies [53] have shown that if the linear natural frequency of the NES is much smaller than that of the primary system, the behaviours similar to those of a true NES can still be obtained. Different from the study in [53], the present apparatus uses a piezoelectric energy harvester. Therefore, it is of importance to study its performance. In this chapter, the transient behaviours of the developed apparatus will be investigated by computer simulation and experimental study.

3.2 Simulation results

As transient responses are considered, the base is fixed, that is, $y(t) = 0$. Hence, the governing equations of the system are rewritten as,

$$\begin{cases} m_p \ddot{x}_p + c_p \dot{x}_p + k_p x_p - [c_a \dot{z} + (k_1 z + k_3 z^3) + \theta V] = 0 \\ m_a \ddot{z} + (1 + \mu) [c_a \dot{z} + (k_1 z + k_3 z^3) + \theta V] - \mu [c_p \dot{x}_p + k_p x_p] = 0 \\ \frac{V}{R} + C^S \dot{V} - \theta \dot{z} = 0 \end{cases} \quad (3.1)$$

To generate transient responses, the following initial conditions are used $x_p(0) = X$, $x_a(0) = X$, $\dot{x}_p(0) = 0$, $\dot{x}_a(0) = 0$. In this case, the relative displacement is intentionally set to be zero to ensure that the total initial system energy is only contained within the primary system and is given by:

$$E_{ini} = E_{tot}(0) = E_p(0) = \frac{1}{2}k_p X^2 \quad (3.2)$$

To measure the effectiveness of the TET phenomenon, the percentage of the instantaneous energy in the NES is defined as follows:

$$D(t) = \frac{E_{NES}(t)}{E_p(t) + E_{NES}(t)} \times 100\% \quad (3.3)$$

where $E_{NES}(t)$ is the instantaneous energy in the NES at time t and defined as follows,

$$E_{NES}(t) = \frac{m_a \dot{x}_a(t)^2}{2} + \frac{k_1 [x_a(t) - x_p(t)]^2}{2} + \frac{k_3 [x_a(t) - x_p(t)]^4}{4} \quad (3.4)$$

and $E_p(t)$ is the total energy in the primary system at time t and defined as the follows:

$$E_p(t) = \frac{1}{2}m_p \dot{x}_p(t)^2 + \frac{1}{2}k_p x_p(t)^2 \quad (3.5)$$

To measure the total accumulated energy, $E_h(t)$ is defined as the follows:

$$E_h(t) = \int_0^t \frac{V(t)^2}{R} dt \quad (3.6)$$

where t is the time duration, R is the resistance value of load resistor, and $V(t)$ is the instantaneous voltage across the load resistor R .

Four different initial energy levels are used. They are $X = 0.52$ mm, $X = 1.42$ mm, $X = 2.65$ mm, $X = 4.45$ mm and named as low, medium, medium high, high energy level, respectively. First, open circuit condition is considered in which the load resistance is set to a significantly large value $R = 100$ M Ω .

Figure 3.1 shows the simulation results with the low initial energy level. It can be seen that it takes a long time for the primary system response to die out, the percentage of the instantaneous energy in the NES is low, and the open circuit voltage is low as well. Clearly at this initial energy level, the TET and energy localization in the NES do not occur. Figure 3.2 shows the contour plots of the wavelet transform spectrum of x_p and x_a , respectively, and complex morlet is used in this wavelet transform. Obviously, the primary mass and NES mass oscillate at different frequencies. Furthermore, it is noted that each of the masses oscillates at a frequency that is close to its own natural frequency.

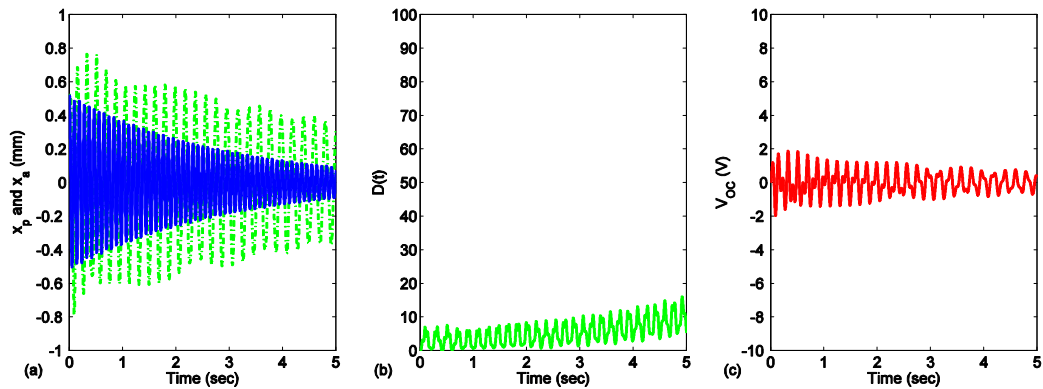


Figure 3.1 Simulation results with $X = 0.52$ mm: (a) displacements (Solid line: primary; Dotted line: NES), (b) the the percentage of instantaneous energy in NES, and (c) open circuit voltage of PEH

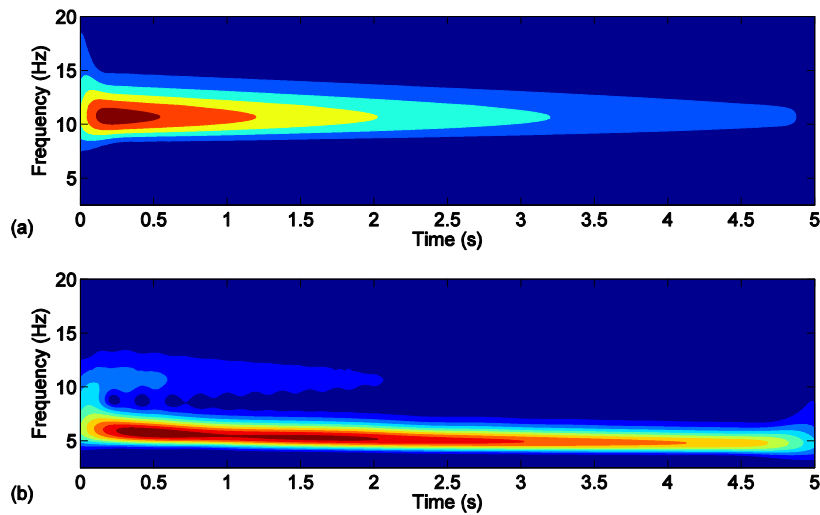


Figure 3.2 Wavelet transform spectra for simulation results with $X = 0.52$ mm: (a) x_p and (b) x_a

Figure 3.3 and Figure 3.4 show the simulation results with the medium initial energy. It can be seen that at this energy level, the NES is engaged. With TET, the vibration energy is quickly localized in the NES. A significant increase is noted in the open circuit voltage. Figure 3.4(a) shows that the dominant oscillating frequency of the primary mass is still very close to f_p indicating that the NES's oscillation has little effect on the primary system. Figure 3.4(b) shows a clear nonlinear behaviour in which the instantaneous frequency gradually reduces and eventually becomes close to f_a . However, it should be also noted that the existence of the beat-like waveform, showing that the TET is not fully established. Figure 3.5 and Figure 3.6 show the results with the medium-high initial energy level. The system behaves similarly to the previous medium initial energy case.

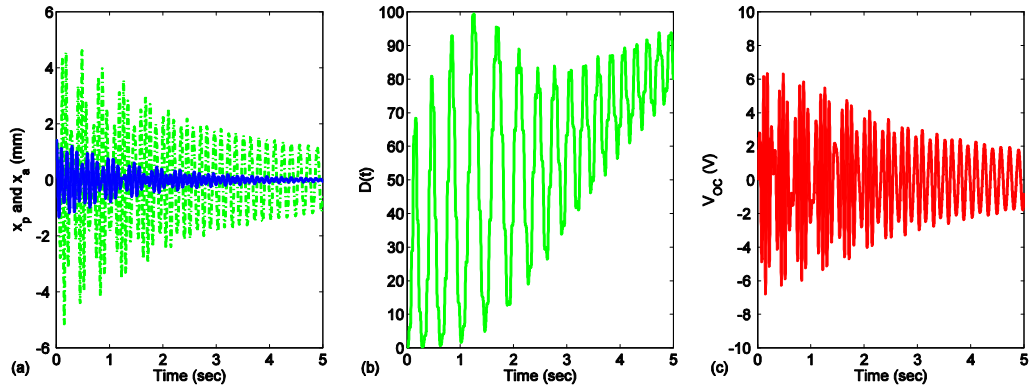


Figure 3.3 Simulation results with $X = 1.42$ mm: (a) displacements (Solid line: primary system; Dotted line: NES), (b) the percentage of instantaneous energy in NES, and (c) open circuit voltage of PEH.

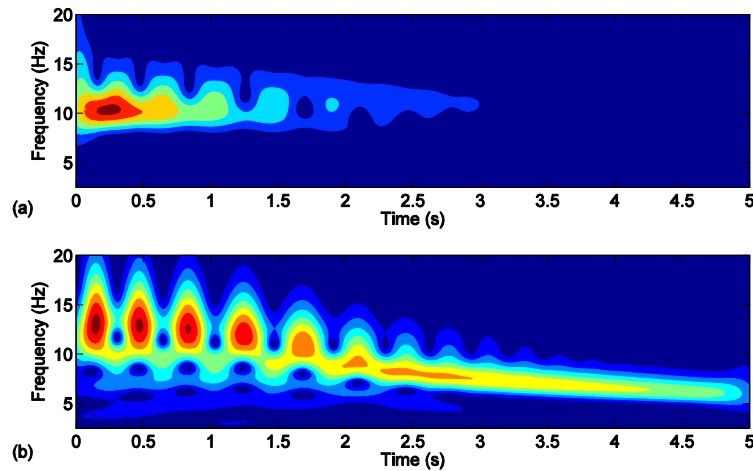


Figure 3.4 Wavelet transform spectra for simulation results with $X = 1.42$ mm: (a) x_p and (b) x_a

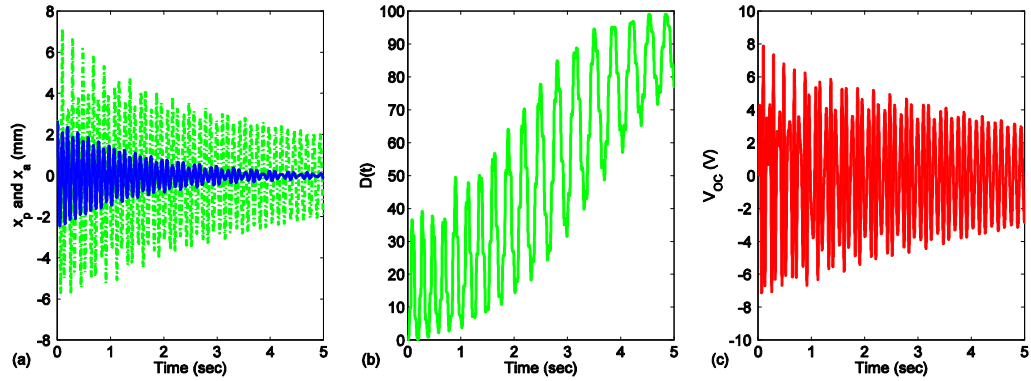


Figure 3.5 Simulation results with $X = 2.65$ mm: (a) displacements (Solid line: primary system; Dotted line: NES), (b) the percentage of instantaneous energy in NES, and (c) open circuit voltage of PEH.

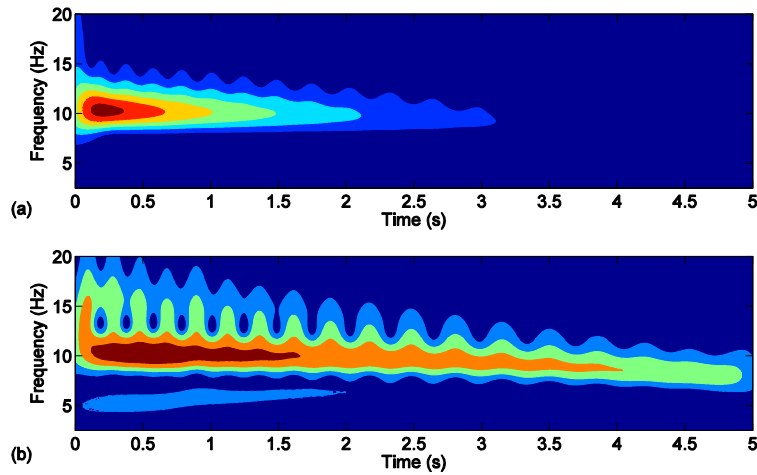


Figure 3.6 Wavelet transform spectra for simulation results with $X = 2.65$ mm: (a) x_p and (b) x_a

Figure 3.7 and Figure 3.8 show the simulation results with the high initial energy level. The desired TET still occurs, but becomes slightly slower than the previous two cases. This indicates that the best performance of the NES exists in a certain range of initial energy levels, which is a typical behaviour of the nonlinear system. Figure 3.8(a) shows a less modulated response of the primary system, and Figure 3.8(b) indicates that the NES is in 1:1 resonance.

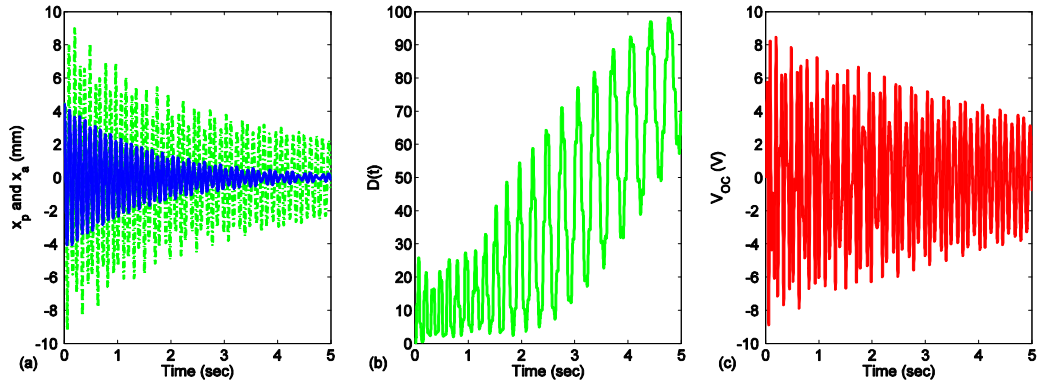


Figure 3.7 Simulation results with $X = 4.45$ mm: (a) displacements (Solid line: primary system; Dotted line: NES), (b) the percentage of instantaneous energy in NES, and (c) open circuit voltage of PEH.

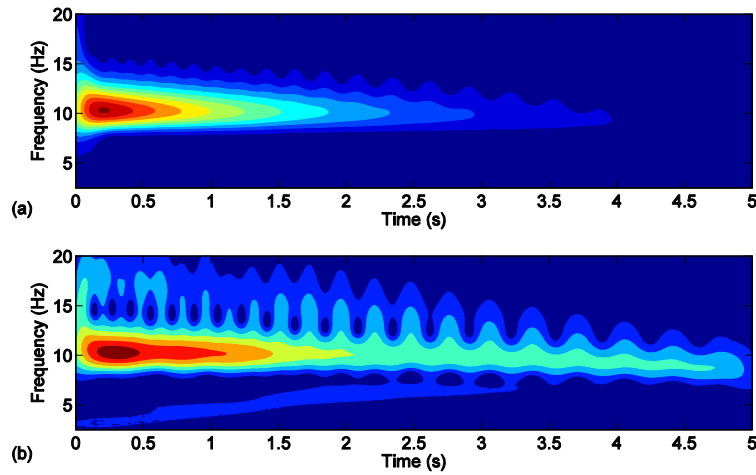


Figure 3.8 Wavelet transform spectra for simulation results with $X = 4.45$ mm: (a) x_p and (b) x_s

To investigate the load effect on the energy harvesting, the circuit is closed by connecting a resistor. The vibration is induced by the high initial energy level $X = 4.45$ mm. Figure 3.9 shows the results for five different load resistance values, namely, $R = 50, 100, 500, 1000, 5000$ K Ω . Figure 3.9(a) is the percentage of instantaneous energy in the NES defined previously in Equation (3.4). Figure 3.9(b) is the accumulated energy harvested by the PEH defined in Equation (3.6). Figure 3.9(c) is the ratio of the accumulated harvested energy over the maximum kinetic energy in the NES. Figure 3.9(b) and (c) show that the accumulated energy in the NES $E_h(t)$ is the highest when the resistance $R = 100$ K Ω among the five resistances.

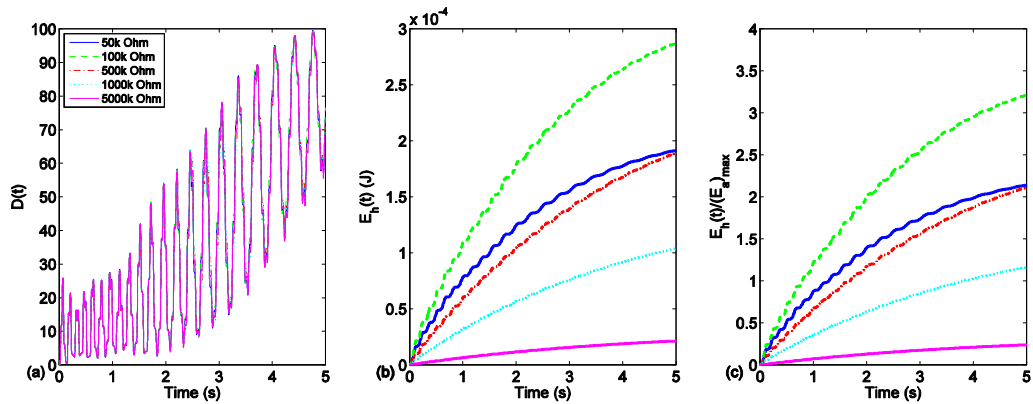


Figure 3.9 Simulation results with $X = 4.45$ mm: (a) the percentage of instantaneous energy in NES, (b) accumulated energy in NES, and (c) ratio of accumulated energy in NES to maximum of kinetic energy of NES.

3.3 Experimental results

For the comparison purpose, experiments are conducted to validate the simulation results. The experimental setup is shown in Figure 3.10 except that the base is fixed and RF sensor for measuring the base motion is unused. Figure 3.11 and Figure 3.12 show the results with the low initial energy level. It is noted that the NES is not engaged. The desired 1:1 resonance and energy localization in the NES clearly do not occur in this case. It is also noted that the generated voltage from the PEH is quite low. These observations are similar to the simulation results shown in Figure 3.1 and Figure 3.2. Figure 3.12 clearly shows that the primary mass and the NES mass vibrate at different frequencies.

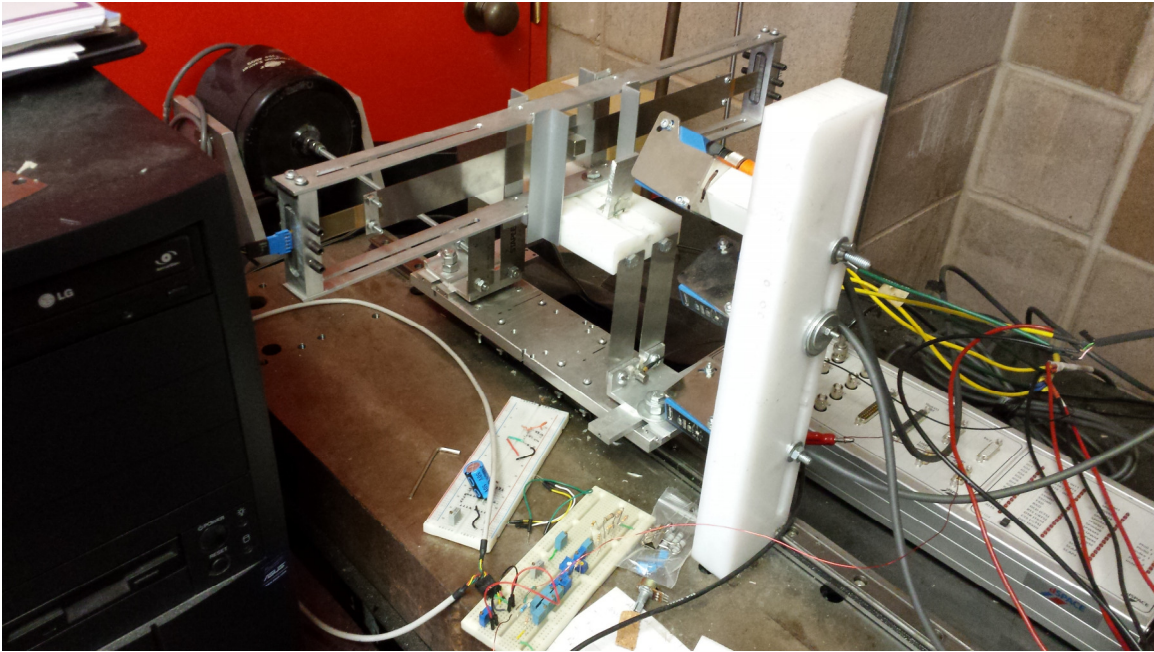


Figure 3.10 Testing apparatus setup

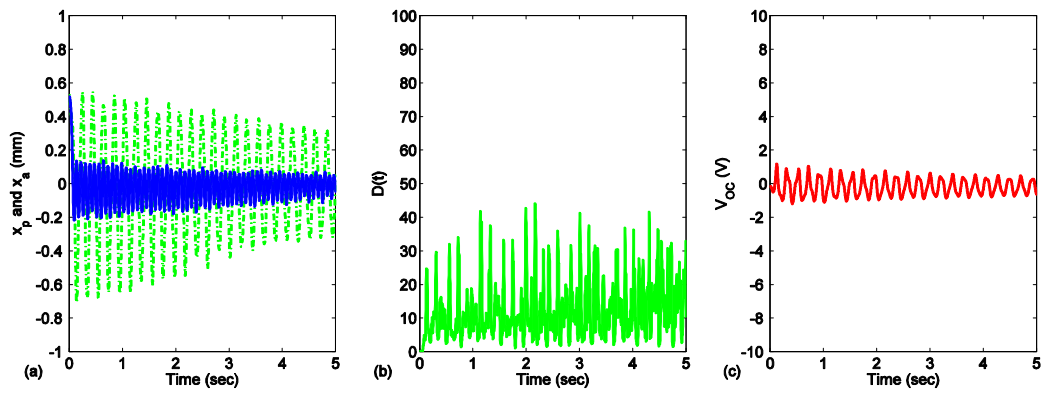


Figure 3.11 Experimental results with $X = 0.52$ mm: (a) displacements (Solid line: primary system; Dotted line: NES), (b) the percentage of instantaneous energy in NES, and (c) open circuit voltage of PEH.

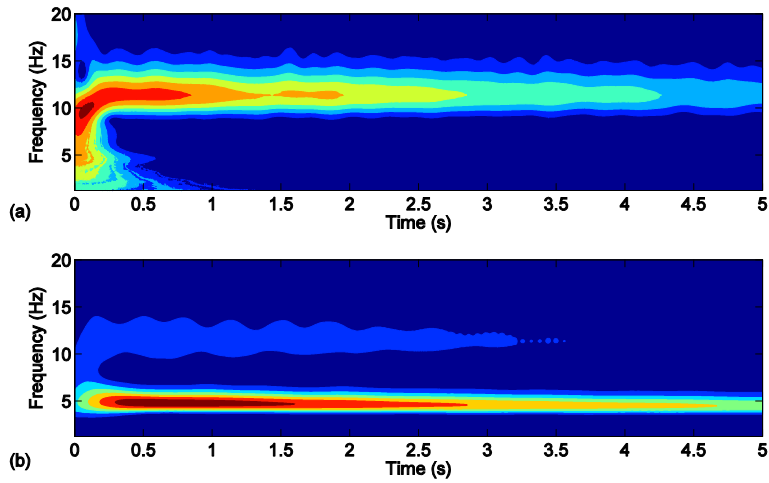


Figure 3.12 Wavelet transform spectra for experimental results with $X = 0.52$ mm: (a) x_p and (b) x_a

Figure 3.13 and Figure 3.14 show the results with the medium initial energy level. Similar to the simulation results in Figure 3.3 and Figure 3.4, the NES is engaged and a visible 1:1 resonance occurs. The energy is being transferred to the NES. The oscillation of the NES clearly shows a nonlinear nature as indicated by Figure 3.14(b). The bear-like waveform of the primary system indicated that the TET is not fully established. The open circuit voltage from the PEH is significantly enhanced compared to that in the previous low initial energy case.

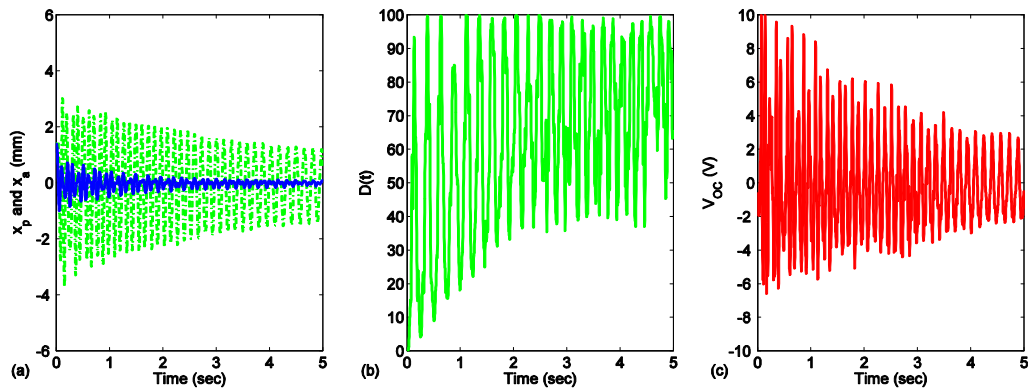


Figure 3.13 Experimental results with $X = 1.42$ mm: (a) displacements (Solid line: primary system; Dotted line: NES), (b) the percentage of instantaneous energy in NES, and (c) open circuit voltage of PEH.

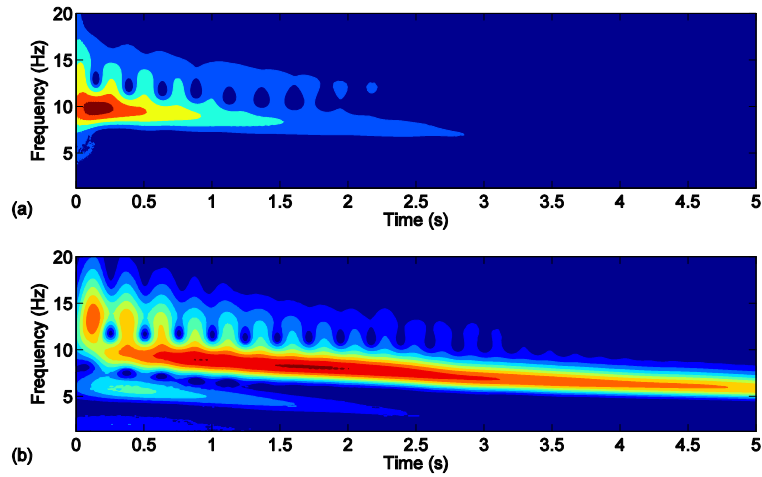


Figure 3.14 Wavelet transform spectra for experimental results with $X = 1.42$ mm: (a) x_p and (b) x_a

Figure 3.15 and Figure 3.16 show the results with the medium-high initial energy level while Figure 3.17 and Figure 3.18 show the results with the high initial energy level. In both the cases, the NES is activated and 1:1 resonance clearly takes place along with the desired TET. After the energy is transferred to the NES, the vibration of the primary system is suppressed quickly, and the NES vibrates somewhat independently as evidenced by its varying frequency which follows the nonlinear manner.

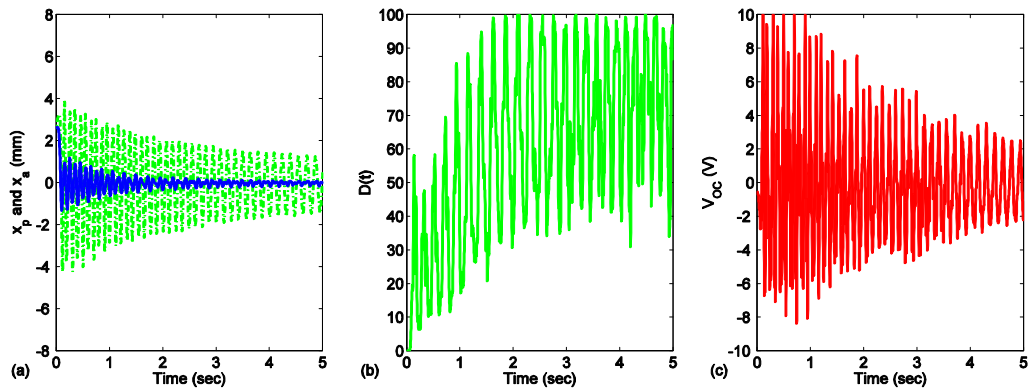


Figure 3.15 Experimental results with $X = 2.65$ mm: (a) displacements (Solid line: primary system; Dotted line: NES), (b) the percentage of instantaneous energy in NES, and (c) open circuit voltage of PEH.

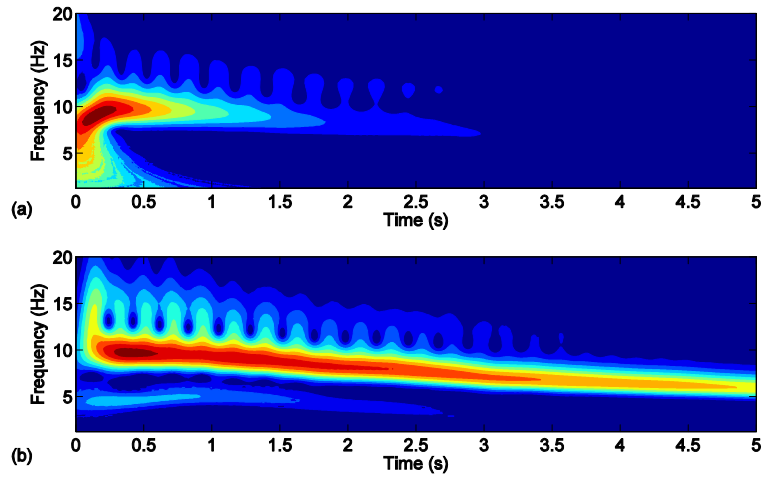


Figure 3.16 Wavelet transform spectra for experimental results with $X = 2.65$ mm: (a) x_p and (b) x_a

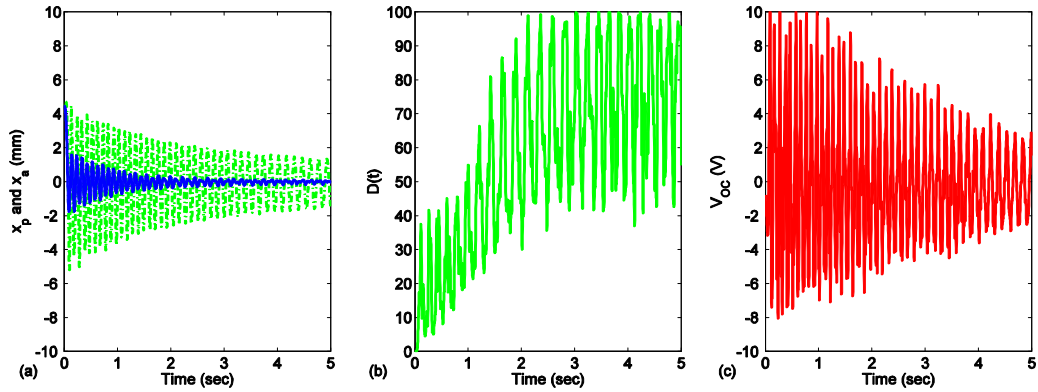


Figure 3.17 Experimental results with $X = 4.45$ mm: (a) displacements (Solid line: primary system; Dotted line: NES), (b) the percentage of instantaneous energy in NES, and (c) open circuit voltage of PEH.

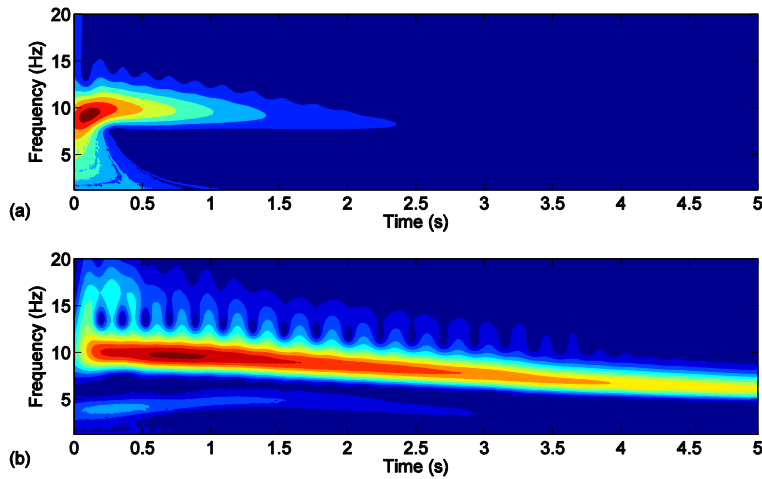


Figure 3.18 Wavelet transform spectra for experimental results with $X = 4.45$ mm: (a) x_p and (b) x_a

To validate the simulation results shown in Figure 3.9, experiments are conducted with the five different load resistances of 50, 100, 500, 1000, and 5000 K Ω . Figure 3.19 shows the results obtained with the high initial energy level of $X = 4.45$ mm. Figure 3.19(a) shows the percentage of the instantaneous energy in the NES defined in Equation (3.4). Figure 3.19(b) is the instantaneous accumulated energy harvested by one PEH. Figure 3.19(c) is the ratio of the instantaneous accumulated harvested energy over the maximum kinetic energy of the NES. Compared to the results shown in Figure 3.9, the similar trends are observed and the highest accumulated energy $E_h(t)$ is obtained with load resistance of 100 K Ω , as predicted by the simulation.

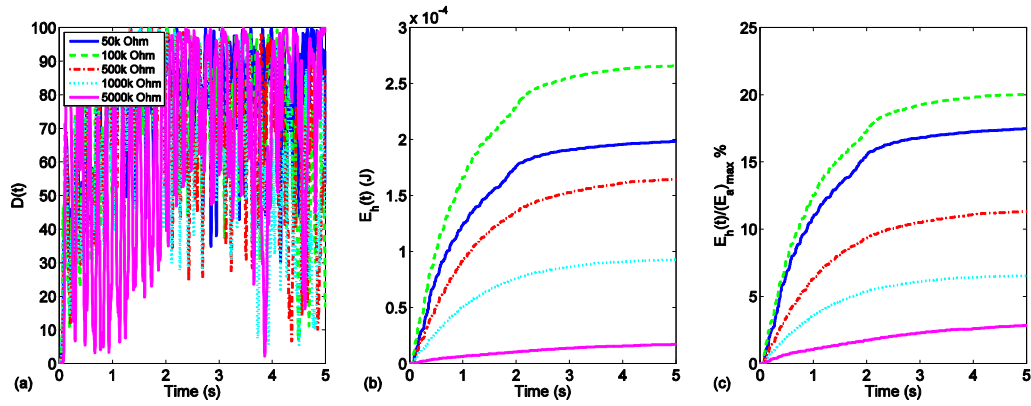


Figure 3.19 Experimental results with $X = 4.45$ mm: (a) the percentage of instantaneous energy in NES, (b) accumulated energy in NES, and (c) ratio of accumulated energy in NES to maximum of kinetic energy of NES.

3.4 Nonlinear normal mode analysis

From the previous section, it is observed that there is an initial energy threshold requirement in order to fully engage the NES into 1:1 resonance. Therefore, it can be assumed that there is a relationship between the oscillation frequency and this energy threshold. To investigate this relationship between the threshold and 1:1 resonance, a concept of nonlinear normal mode (NNM) and periodic orbits is employed [22]. For this purpose, the underlying Hamiltonian system is considered,

$$\begin{cases} m_p \ddot{x}_p + k_p x_p - k_1 z - k_3 z^3 = 0 \\ m_a \ddot{z} + (1 + \mu)(k_1 z + k_3 z^3) - \mu k_p x_p = 0 \end{cases} \quad (3.7)$$

The NNM analysis starts with introducing new complex variables as follows,

$$\psi_1 = \dot{x}_p + j\omega x_p \text{ and } \psi_2 = \dot{x}_a + j\omega x_a \quad (3.8)$$

where ω is the dominant frequency or also known as the fast frequency of oscillation and $j = \sqrt{-1}$. By rearranging these new complex variables, displacements and accelerations of the primary system and NES system are obtained as,

$$x_p = \frac{\psi_1 - \bar{\psi}_1}{2j\omega}, \quad \ddot{x}_p = \dot{\psi}_1 - \frac{j\omega}{2}(\psi_1 + \bar{\psi}_1) \quad (3.9)$$

$$x_a = \frac{\psi_2 - \bar{\psi}_2}{2j\omega}, \quad \ddot{x}_a = \dot{\psi}_2 - \frac{j\omega}{2}(\psi_2 + \bar{\psi}_2) \quad (3.10)$$

where the overhead bar represents its complex conjugate. Since periodic orbits are sought, it is assumed that the primary system and NES oscillate with the same fast frequency ω , the previously introduced complex variables in Equation (3.8) are approximately expressed in terms of the fast frequency ω , $e^{j\omega t}$ and modulated by slowly varying amplitudes $\phi_i(t)$, $i = 1, 2$ as

$$\psi_1(t) = \phi_1(t)e^{j\omega t} \text{ and } \psi_2(t) = \phi_2(t)e^{j\omega t} \quad (3.11)$$

Substituting Equations (3.9) - (3.11) into Equation (3.7) yields,

$$\begin{aligned} & m_p \left(\frac{d}{dt} (\phi_1(t)e^{j\omega t}) - \frac{j\omega}{2} (\phi_1(t)e^{j\omega t} + \bar{\phi}_1(t)e^{-j\omega t}) \right) - \frac{jk_p}{2\omega} (\phi_1(t)e^{j\omega t} - \bar{\phi}_1(t)e^{-j\omega t}) \dots \\ & - \frac{jk_1}{2\omega} \left((\phi_1(t)e^{j\omega t} - \bar{\phi}_1(t)e^{-j\omega t}) - (\phi_2(t)e^{j\omega t} - \bar{\phi}_2(t)e^{-j\omega t}) \right) \dots \\ & + \frac{jk_3}{8\omega^3} \left((\phi_1(t)e^{j\omega t} - \bar{\phi}_1(t)e^{-j\omega t}) - (\phi_2(t)e^{j\omega t} - \bar{\phi}_2(t)e^{-j\omega t}) \right)^3 = 0 \end{aligned} \quad (3.12)$$

$$\begin{aligned}
& m_a \left[\left(\frac{d}{dt}(\phi_2(t)e^{j\omega t}) - \frac{j\omega}{2}(\phi_2(t)e^{j\omega t} + \bar{\phi}_2(t)e^{-j\omega t}) \right) \right] \dots \\
& \left[- \left(\frac{d}{dt}(\phi_1(t)e^{j\omega t}) - \frac{j\omega}{2}(\phi_1(t)e^{j\omega t} + \bar{\phi}_1(t)e^{-j\omega t}) \right) \right] \dots \\
& + (1+\mu) \left[\frac{jk_1}{2\omega} \left((\phi_1(t)e^{j\omega t} - \bar{\phi}_1(t)e^{-j\omega t}) - (\phi_2(t)e^{j\omega t} - \bar{\phi}_2(t)e^{-j\omega t}) \right) \right. \\
& \left. - \frac{jk_3}{8\omega^3} \left((\phi_1(t)e^{j\omega t} - \bar{\phi}_1(t)e^{-j\omega t}) - (\phi_2(t)e^{j\omega t} - \bar{\phi}_2(t)e^{-j\omega t}) \right)^3 \right] \dots \quad (3.13) \\
& + \frac{j\mu k_p}{2\omega} (\phi_1(t)e^{j\omega t} - \bar{\phi}_1(t)e^{-j\omega t}) = 0
\end{aligned}$$

The above equations are simplified further, and only terms associated with the fast frequency ω are kept. And, higher order frequency terms associated with $e^{j3\omega t}$ and $e^{j5\omega t}$ are ignored. Collecting the terms only associated with $e^{j\omega t}$ yields a set of complex modulating equations as

$$\begin{aligned}
& m_p \left(\dot{\phi}_1 + \frac{j\omega}{2} \phi_1 \right) - \frac{jk_p}{2\omega} \phi_1 + \frac{jk_1}{2\omega} (\phi_2 - \phi_1) \dots \\
& + \frac{3jk_3}{8\omega^3} (\phi_1^2 \bar{\phi}_2 - \bar{\phi}_1 \phi_2^2 - \bar{\phi}_1 \phi_1^2 + \phi_2^2 \bar{\phi}_2 - 2\phi_1 \phi_2 \bar{\phi}_2 + 2\phi_1 \bar{\phi}_1 \phi_2) = 0 \quad (3.14)
\end{aligned}$$

$$\begin{aligned}
& m_a \left[\left(\dot{\phi}_2 + \frac{j\omega}{2} \phi_2 \right) - \left(\dot{\phi}_1 + \frac{j\omega}{2} \phi_1 \right) \right] + \frac{j\mu k_p}{2\omega} \phi_1 - \frac{jk_1}{2\omega} (1+\mu) (\phi_2 - \phi_1) \dots \\
& - \frac{3jk_3}{8\omega^3} (1+\mu) (\phi_1^2 \bar{\phi}_2 - \bar{\phi}_1 \phi_2^2 - \bar{\phi}_1 \phi_1^2 + \phi_2^2 \bar{\phi}_2 - 2\phi_1 \phi_2 \bar{\phi}_2 + 2\phi_1 \bar{\phi}_1 \phi_2) = 0 \quad (3.15)
\end{aligned}$$

where dot denotes the derivative with respect to time. Furthermore, the polar form of complex amplitudes is introduced as $\phi_1 = a(t)e^{j\alpha(t)}$ and $\phi_2 = b(t)e^{j\beta(t)}$, where $a(t)$ and $b(t)$ are real amplitudes and $\alpha(t)$ and $\beta(t)$ are real phases. Substituting the polar forms into Equations (3.14) and (3.15), and separating the real and imaginary parts yields the following equations,

$$\begin{aligned}
\dot{a} &= \frac{1}{8m_p \omega^3} (-3k_3 a^2 b - 3k_3 b^3 - 4k_1 b \omega^2) \sin(\alpha - \beta) \dots \\
& + \frac{3}{8m_p \omega^3} (k_3 a b^2) \sin(2\alpha - 2\beta) \quad (3.16)
\end{aligned}$$

$$\begin{aligned}
\dot{\alpha} &= \frac{1}{8m_p a \omega^3} (-9k_3 a^2 b - 3k_3 b^3 - 4k_1 b \omega^2) \cos(\alpha - \beta) \dots \\
&+ \frac{3}{8m_p \omega^3} (k_3 b^2) \cos(2\alpha - 2\beta) \dots \\
&+ \frac{1}{8m_p a \omega^3} (4k_p a \omega^2 - 4am_p \omega^4 + 4k_1 a \omega^2 + 3k_3 a^3 + 6k_3 ab^2)
\end{aligned} \tag{3.17}$$

$$\dot{b} = \frac{1}{8m_a \omega^3} (4k_1 a \omega^2 + 3k_3 a^3 + 3k_3 ab^2) \sin(\alpha - \beta) - \frac{3}{8m_a \omega^3} (k_3 a^2 b) \sin(2\alpha - 2\beta) \tag{3.18}$$

$$\begin{aligned}
\dot{\beta} &= \frac{1}{8m_a b \omega^3} (-9k_3 ab^2 - 4k_1 a \omega^2 - 3k_3 a^3) \cos(\alpha - \beta) \dots \\
&+ \frac{3}{8m_a \omega^3} (k_3 a^2) \cos(2\alpha - 2\beta) \dots \\
&+ \frac{1}{8m_a b \omega^3} (4k_1 b \omega^2 - 4m_a b \omega^4 + 6k_3 a^2 b + 3k_3 b^3)
\end{aligned} \tag{3.19}$$

Since periodic solutions are being sought, these solutions shall be found in the steady-state. Thus, the derivatives of α and β with respect to time in Equations (3.17) and (3.19) are to be set to zero. Furthermore, the system is assumed to oscillate in phase, then $\alpha = \beta$. Equations (3.17) and (3.19) are therefore reduced to a set of two coupled nonlinear algebraic equations defining the amplitudes of the system,

$$\begin{aligned}
0 &= \frac{1}{8m_p a \omega^3} (-9k_3 a^2 b - 3k_3 b^3 - 4k_1 b \omega^2) + \frac{3}{8m_p \omega^3} (k_3 b^2) \dots \\
&+ \frac{1}{8m_p a \omega^3} (4k_p a \omega^2 - 4m_p a \omega^4 + 4k_1 a \omega^2 + 3k_3 a^3 + 6k_3 ab^2)
\end{aligned} \tag{3.20}$$

$$\begin{aligned}
0 &= \frac{1}{8m_a b \omega^3} (-9k_3 ab^2 - 3k_3 a^3 - 4k_1 a \omega^2) + \frac{3}{8m_a \omega^3} (k_3 a^2) \dots \\
&+ \frac{1}{8m_a b \omega^3} (4k_1 b \omega^2 - 4m_a b \omega^4 + 3k_3 b^3 + 6k_3 a^2 b)
\end{aligned} \tag{3.21}$$

The two equations are numerically solved for a and b by specifying a frequency ω . In general, the periodic responses can be expressed as follows,

$$x_p(t) \approx X_p \cos(\omega t) = \frac{\psi_1 - \bar{\psi}_1}{2j\omega} = \frac{a}{\omega} \cos(\omega t) \quad (3.22)$$

$$x_a(t) \approx X_a \cos(\omega t) = \frac{\psi_2 - \bar{\psi}_2}{2j\omega} = \frac{b}{\omega} \cos(\omega t) \quad (3.23)$$

In order to find the relationship between energy and frequency, the total energy of the system is defined by its potential energy as follows,

$$E = \frac{1}{2}k_p X_p^2 + \frac{1}{2}k_1 Z^2 + \frac{1}{4}k_3 Z^4 \quad (3.24)$$

where $Z = X_a - X_p$ denotes the relative displacement amplitude.

Figure 3.20 is the so-called frequency-energy plot (FEP) in which the amplitudes and obtained by solving Equations (3.20) and (3.21) are plotted as a function of the total energy defined by Equation (3.24) and frequency. There exist two backbone branches of NNMs, an in-phase branch, S11+, originating from the natural frequency $f_a = 4.587$ Hz of the NES and an out-of-phase one, S11-, originating from the natural frequency $f_p = 10.71$ Hz of the primary system. The energy threshold of the system, shown in Figure 23, represents the minimum energy required to set the system into oscillation along the S11+ curve. If the energy is lower than this threshold, the system will be attracted to the S11- curve.

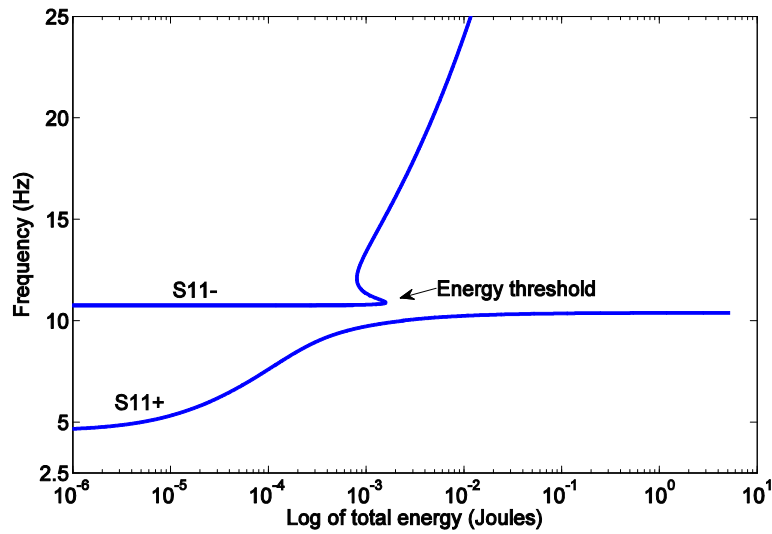


Figure 3.20 Frequency energy plot: backbone curves S11±

To illustrate this effect, a wavelet transform is applied to the relative displacements corresponding to the four initial energy levels. At each time t , the total energy level of the responses is determined so that the corresponding time is matched to this energy level. Then, the contour of the wavelet spectra defined by the frequency and energy level is superimposed on top of the backbone curves of the frequency energy plot. Figure 3.21 shows the plots obtained with the simulation results. As shown in Figure 3.21(a), for the low initial energy level, the system tends to be attracted to the $S11^-$ curve. The system exhibits a weak nonlinearity so that there is little energy exchange between the primary mass and NES mass, noting the existence of the energy concentration around the low frequencies that are close to the natural frequency of the NES. This is attributed to the fact that the NES is not essentially nonlinear.

Shown in Figure 3.21(b), as the initial energy exceeds the threshold level, the higher frequency components are present at the higher energy level region, revealing by the initial nonlinear beating phenomena. Once the nonlinear beating becomes less dominant, the fundamental TET due to 1:1 transient resonance capture is triggered, as the transient dynamics traces approximately the in-phase backbone branch $S11^+$. This indicates that the energy is gradually localized in the NES.

Figure 3.21(c) shows the case of the medium-high initial energy level while Figure 3.21(d) showing the case of the high initial energy level. The higher frequency components still appear, and however only last for a short period of time at the higher energy level region. The beat-like wavelet transform is significantly less dominant comparing to the previous case. At those energy levels, the responses are firmly in 1:1 resonance and attracted to the $S11^+$ backbone curve. The energy is rapidly transferred to the NES.

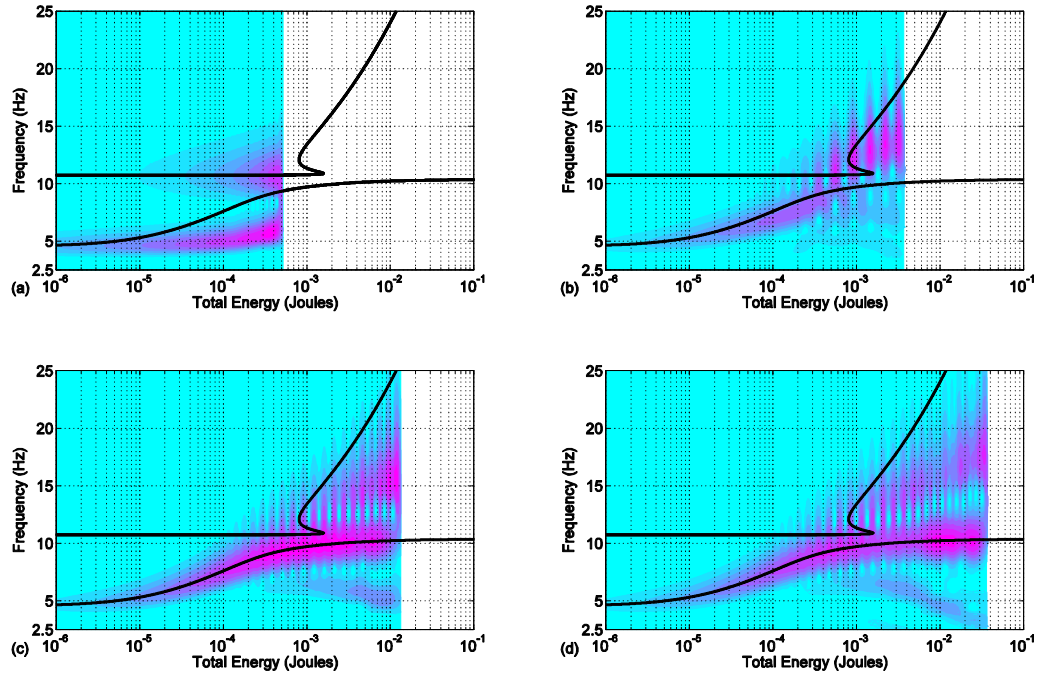


Figure 3.21 Frequency energy plots and wavelet transforms of relative displacement $x_a - x_p$ from the simulation results for $f_p = 10.71$ Hz: (a) low initial energy $X = 0.52 \times 10^{-3}$ (m); (b) medium initial energy $X = 1.42 \times 10^{-3}$ (m); (c) medium-high initial energy $X = 2.65 \times 10^{-3}$ (m) and; (d) high initial energy $X = 4.45 \times 10^{-3}$ (m).

Figure 3.22 show the plots obtained using the experimental results. In Figure 3.22(a), for the low initial energy level below the energy threshold, it can be seen that energy is primarily concentrated around f_a and f_p similar to that in Figure 3.21(a). In Figure 3.22(b), as the initial energy level increases above the energy threshold, higher frequency components are present at higher frequency region. And, now the energy is shifted and concentrated along the backbone curve $S11+$.

Figure 3.22(c) and Figure 3.22(d) show the case of the medium-high and high initial energy level, respectively. The higher frequency components appear but are not dominating comparing to low frequency components. It can still be seen that the energy is concentrated primarily along the backbone curve $S11+$, and the nonlinear beating effect are not present in these plots. This indicates that the TET is activated. The energy is following the backbone curve $S11+$ and towards to the lower frequency region with less high frequency components, and this indicates that the energy is gradually localized in the NES

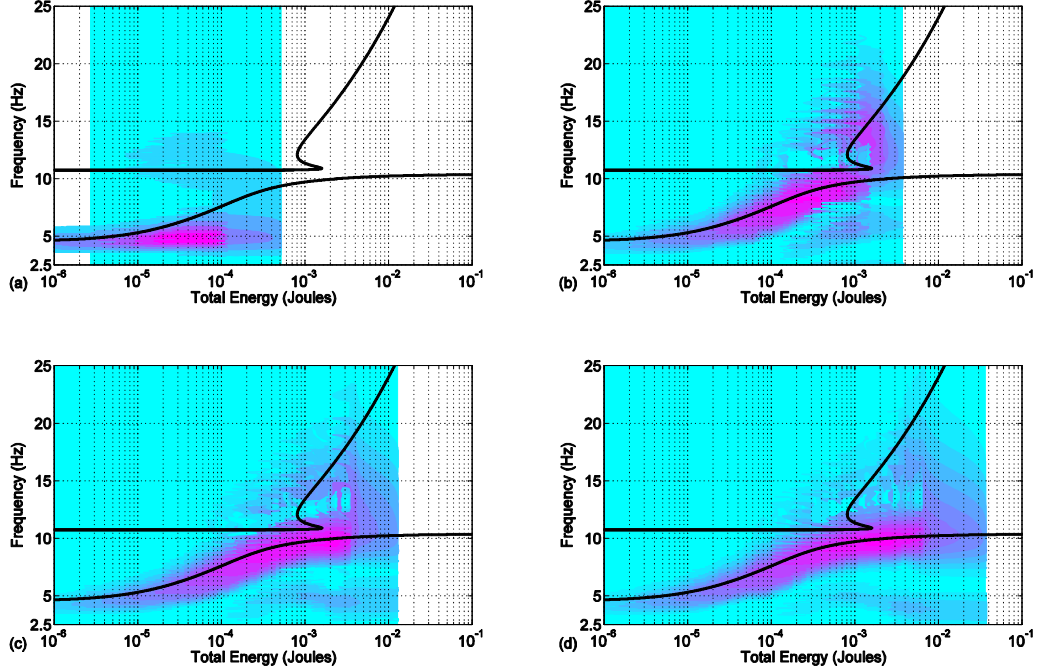


Figure 3.22 Frequency energy plots and wavelet transforms of relative displacement $x_a - x_p$ from the experimental results for $f_p = 10.71$ Hz: (a) low initial energy $X = 0.52 \times 10^{-3}$ (m); (b) medium initial energy $X = 1.42 \times 10^{-3}$ (m); (c) medium-high initial energy $X = 2.65 \times 10^{-3}$ (m) and; (d) high initial energy $X = 4.45 \times 10^{-3}$ (m).

3.5 Comparison of three systems

As pointed out previously, the developed apparatus is not a true NES as it possesses a linear stiffness. The simulation results have indicated that the apparatus acts similarly when its linear natural frequency is much lower than that of the primary system. In this section, three systems are compared in order to examine how the linear natural frequency of the NES affects its behaviours. For this purpose, the equations of motion derived in the previous chapter are reformulated by defining several dimensionless variables and time in a similar way used in [30, 55, 56, 57]. The equations of motion presented in Chapter 2 are represented below,

$$m_p \ddot{x}_p + c_p \dot{x}_p + k_p x_p - \left[c_a \dot{z} + (k_1 z + k_3 z^3) + \theta V \right] = 0 \quad (3.25)$$

$$m_a \ddot{z} + (1 + \mu) \left[c_a \dot{z} + (k_1 z + k_3 z^3) + \theta V \right] - \mu \left[c_p \dot{x}_p + k_p x_p \right] = 0 \quad (3.26)$$

$$\frac{V}{R} + C^S \dot{V} - \theta \dot{z} = 0. \quad (3.27)$$

By dividing Equation (3.25) by and Equation (3.26) by respectively, it yields,

$$\ddot{x}_p + \frac{c_p}{m_p} \dot{x}_p + \frac{k_p}{m_p} x_p - \frac{c_a}{m_p} \dot{z} - \frac{k_1}{m_p} z - \frac{k_3}{m_p} z^3 - \frac{\theta}{m_p} V = 0 \quad (3.28)$$

$$\ddot{z} + (1 + \mu) \left[\frac{c_a}{m_a} \dot{z} + \frac{k_1}{m_a} z + \frac{k_3}{m_a} z^3 + \frac{\theta}{m_a} V \right] - \mu \left[\frac{c_p}{m_a} \dot{x}_p + \frac{k_p}{m_a} x_p \right] = 0 \quad (3.29)$$

By simplifying Equations (3.28) and, it leads to,

$$\ddot{x}_p + 2\zeta_p \omega_p \dot{x}_p + \omega_p^2 x_p - 2\mu \zeta_a \omega_a \dot{z} - \mu \omega_a^2 z - \frac{k_3}{m_p} z^3 - \frac{\theta}{m_p} V = 0 \quad (3.30)$$

$$\ddot{z} + (1 + \mu) \left[2\zeta_a \omega_a \dot{z} + \omega_a^2 z + \frac{k_3}{m_a} z^3 + \frac{\theta}{m_a} V \right] - \mu \left[\frac{1}{\mu} 2\zeta_p \omega_p \dot{x}_p + \frac{1}{\mu} \omega_p^2 x_p \right] = 0 \quad (3.31)$$

where,

$$\omega_p = \sqrt{\frac{k_p}{m_p}}, \quad \zeta_p = \frac{c_p}{2m_p \omega_p}, \quad \omega_a = \sqrt{\frac{k_1}{m_a}}, \quad \zeta_a = \frac{c_a}{2m_a \omega_a}, \quad \mu = \frac{m_a}{m_p}$$

A dimensionless time τ is defined as $\tau = \omega_p t$, thus

$$\frac{d\tau}{dt} = \omega_p \quad (3.32)$$

$$\frac{d}{dt} x_p(t) = \frac{dx_p}{d\tau} \frac{d\tau}{dt} = \omega_p \frac{d}{d\tau} x_p(\tau) = \omega_p x_p' \quad (3.33)$$

$$\frac{d^2}{dt^2} x_p(t) = \omega_p^2 \frac{d^2}{d\tau^2} x_p(\tau) = \omega_p^2 x_p'' \quad (3.34)$$

where prime denotes differentiation with respect to τ . Similarly,

$$\frac{d}{dt} z(t) = \frac{dz}{d\tau} \frac{d\tau}{dt} = \omega_p \frac{d}{d\tau} z(\tau) = \omega_p z' \quad (3.35)$$

$$\frac{d^2}{dt^2} z(t) = \omega_p^2 \frac{d^2}{d\tau^2} z(\tau) = \omega_p^2 z'' \quad (3.36)$$

$$\frac{d}{dt} V(t) = \omega_p \frac{d}{d\tau} V(\tau) = \omega_p V' \quad (3.37)$$

By substituting Equations (3.33) to (3.37) into Equations (3.30) and (3.31), this leads to,

$$\omega_p^2 x_p'' + 2\zeta_p \omega_p^2 x_p' + \omega_p^2 x_p - 2\mu \zeta_a \omega_a \omega_p z' - \mu \omega_a^2 z - \frac{k_3}{m_p} z^3 - \frac{\theta}{m_p} V = 0 \quad (3.38)$$

$$\omega_p^2 z'' + (1 + \mu) \left[2\zeta_a \omega_a \omega_p z' + \omega_a^2 z + \frac{k_3}{m_a} z^3 + \frac{\theta}{m_a} V \right] - \mu \left[\frac{1}{\mu} 2\zeta_p \omega_p^2 x_p' + \frac{1}{\mu} \omega_p^2 x_p \right] = 0 \quad (3.39)$$

$$\frac{V}{R} + C^S \omega_p V' - \theta \omega_p z' = 0 \quad (3.40)$$

Dividing Equations (3.38) and (3.39) by ω_p^2 and dividing Equation (3.40) by ω_p^2 , this leads to,

$$x_p'' + 2\zeta_p x_p' + x_p - 2\mu \zeta_a \eta z' - \mu \eta^2 z - \bar{k}_3 z^3 - \bar{\theta} V = 0 \quad (3.41)$$

$$z'' + (1 + \mu) \left[2\zeta_a \eta z' + \eta^2 z + \frac{1}{\mu} \bar{k}_3 z^3 + \frac{1}{\mu} \bar{\theta} V \right] - 2\zeta_p x_p' - x_p = 0 \quad (3.42)$$

$$\frac{V}{k_p \omega_p R} + \frac{C^S}{k_p} V' - \bar{\theta} z' = 0 \quad (3.43)$$

where,

$$\eta = \frac{\omega_a}{\omega_p}, \bar{k}_3 = \frac{k_3}{k_p}, \bar{\theta} = \frac{\theta}{k_p}$$

The variable η is called the frequency ratio that can be used to represent the linear coupling between the primary system and NES system. If $\eta = 0$, the system becomes a true NES. If $\eta = 1$, the system becomes a nonlinear vibration absorber. In what follows, the linear natural frequency of the NES is fixed as $f_a = 4.5$ Hz, three different values for η will be used, i.e., $\eta_i = [0.3 \ 0.5 \ 1]$. This leads to,

$$\eta_i = \frac{\omega_a}{\omega_p} \Rightarrow \omega_p = \frac{\omega_a}{\eta_i} \Rightarrow \sqrt{\frac{(k_p)_i}{m_p}} = \frac{\omega_a}{\eta_i} \Rightarrow (k_p)_i = m_p \left(\frac{\omega_a}{\eta_i} \right)^2 \quad (3.44)$$

$$(k_p)_i = [7752.32 \quad 2790.84 \quad 697.71] \text{ N/m} \quad (3.45)$$

$$(\omega_p)_i = [15 \quad 9 \quad 4.5] \text{ Hz} \quad (3.46)$$

To have a fair comparison of the systems with different η values, the free responses are generated by keeping the initial potential energy equal or $E_p = \frac{1}{2}(k_p)_i (X_p)_i^2$. The primary system with the natural frequency of 9 Hz is used as a baseline to determine beam deflection for the specified initial energy level. From experiments trials, the maximum initial deflection for the baseline system is 4.45 mm. Thus, the initial energy is $E_p = \frac{1}{2}k_p X_p^2 = 0.02736 \text{ J}$. Therefore, for two different systems with η_1 and η_2 , respectively, their initial displacements of the primary systems $(X_p)_1$ and $(X_p)_2$ are related by

$$\begin{aligned} E_p &= \frac{1}{2}(k_p)_1 (X_p)_1^2 = \frac{1}{2}(k_p)_2 (X_p)_2^2 \\ \Rightarrow (X_p)_2 &= \sqrt{\frac{(k_p)_1}{(k_p)_2}} (X_p)_1 \Rightarrow (X_p)_2 = (X_p)_1 \frac{(\omega_p)_1}{(\omega_p)_2} \end{aligned} \quad (3.47)$$

Using the primary system with $f_p = 9 \text{ Hz}$ as a base line system or $E_p = 0.02736 \text{ J}$, the initial displacements for the three systems are found to be $(X_p)_i = [2.67 \quad 4.45 \quad 8.9] \text{ mm}$.

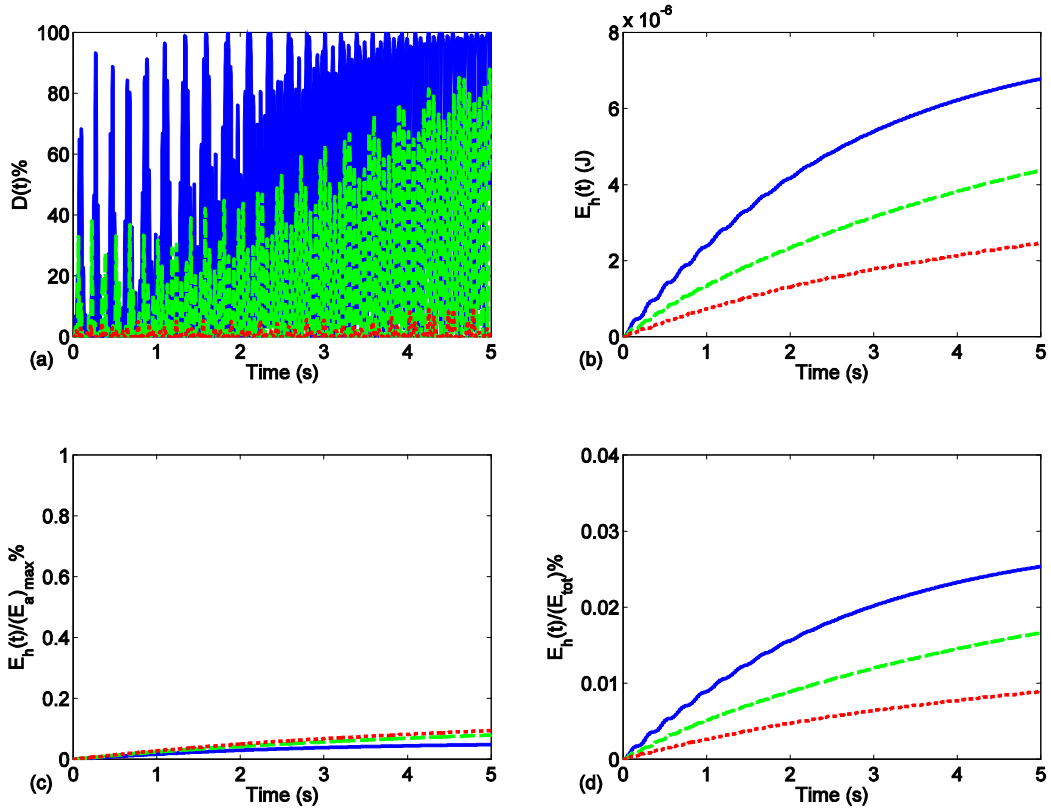


Figure 3.23 Simulation results of non-dimensional system: (a) the percentage of instantaneous energy in NES, (b) accumulated energy in NES, (c) ratio of accumulated energy in NES to maximum of kinetic energy in NES, and (d) ratio of accumulated energy in NES to total system energy, (solid blue line: $\eta = 0.3$ or $f_p = 15$ Hz, dash green line: $\eta = 0.5$ or $f_p = 9$ Hz, and red dotted line: $\eta = 1$ or $f_p = 4.5$ Hz).

Figure 3.23 shows the simulation results for the three systems. Figure 3.23(a) indicates the percentage of the instantaneous energy in the NES over the instantaneous total system energy. At $\eta=0.3$ or $f_p=15$ Hz, the general trend of this curve rapidly increases comparing to the other two curves. Figure 3.23(b) shows that the harvested energy in joules over time at a resistance value of $R = 100$ K Ω , and it shows that the amount of the harvested energy is inverse proportional to the frequency ratio. Figure 3.23(c) and Figure 3.23(d) show the ratio of the accumulated energy in the NES to the maximum kinetic energy of the NES and the ratio of the accumulated energy in the NES to the total system energy at the open circuit condition, respectively. In Figure 3.23(c), it is observed that the ratio is overall decreasing when increasing frequency ratio η ; however, Figure 3.23(d) shows that the ratio of accumulated energy in NES to total system energy is higher with increasing frequency ratio η .

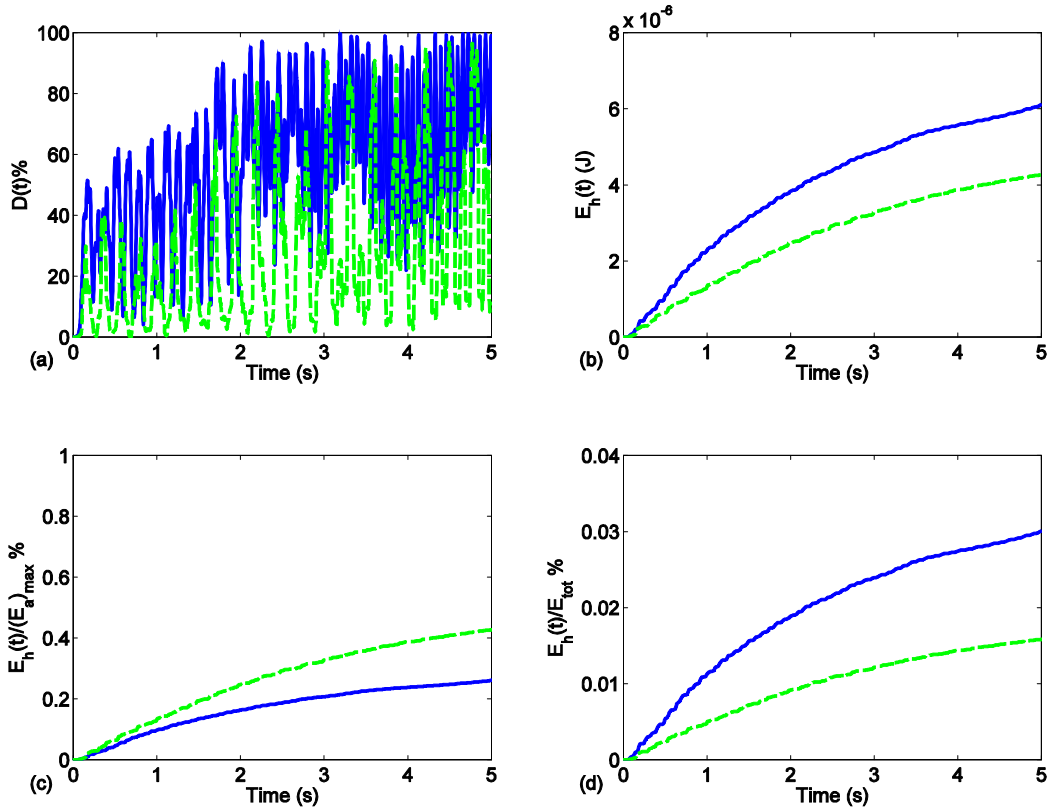


Figure 3.24 Experimental results of non-dimensional system: (a) the percentage of instantaneous energy in NES, (b) accumulated energy in NES, (c) ratio of accumulated energy in NES to maximum of kinetic energy in NES, and (d) ratio of accumulated energy in NES to total system energy, (solid blue line: $\eta = 0.3$ or $f_p = 15$ Hz, dash green line: $\eta = 0.5$ or $f_p = 9$ Hz).

Experiments are conducted and presented in Figure 3.24 to compare with Figure 3.23. However, only primary systems of 9 Hz and 15 Hz are used in experiments and shown in Figure 3.24.

Figure 3.25(a) and (b) shown below is the frequency energy plot (FEP) in which the amplitudes X_p and X_a obtained by solving Equations (3.20) and (3.21) are plotted as a function of the total energy defined by Equation (3.24) and frequency ω for $\eta = 0.5$ and $\eta = 0.3$ respectively. There exist two backbone branches of NNMs as an out-of-phase branch $S11^-$ and an in-phase branch $S11^+$ in both (a) and (b), while system total energy decreases, the in-phase branch terminates toward to the linear natural frequency $f_a = 4.5$ Hz of the NES and an out-of-phase one, $S11^-$, terminates toward to the natural frequency $f_p = 9$ Hz and $f_p = 15$ Hz of the

primary system respectively. The energy threshold of the system, shown in Figure 3.25, represents the minimum energy required to set the system into oscillation along the $S11+$ curve. If the energy is lower than this threshold, the system energy will be attracted to the $S11-$ curve. The energy threshold shown in Figure 3.25(a) and (b) are referred as tongue discussed in [22], and it is observed that the tongue is leaping toward to higher energy value as primary system natural frequency f_p increasing while maintaining NES linear natural frequency constant.

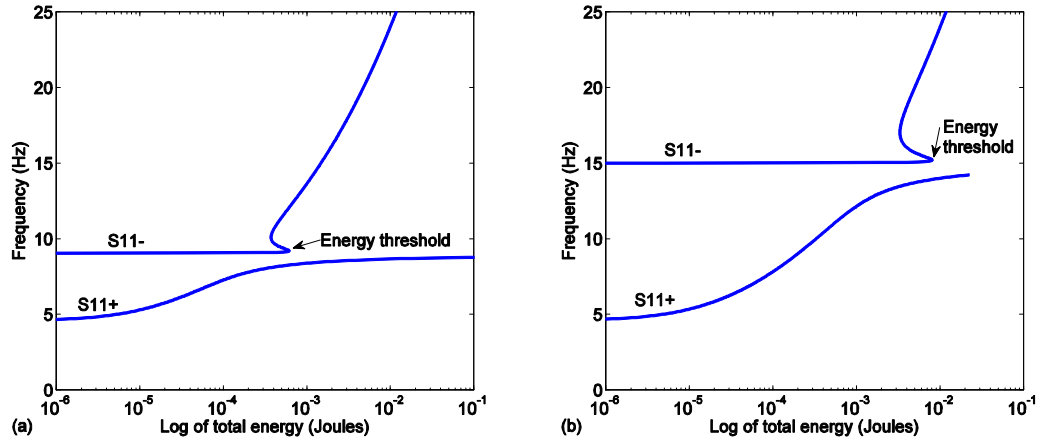


Figure 3.25 Frequency energy plot: backbone curves $S11\pm$ for (a) $f_p = 9$ Hz, (b) $f_p = 15$ Hz

Figure 3.26 shows frequency energy plots superimposed by the contours of the wavelet spectra of the relative displacements obtained with the simulation results for $f_p = 9$ Hz. As shown in Figure 3.26(a), for the low initial energy level, the system tends to oscillate with the $S11-$ curve. The system exhibits a weak nonlinearity so that there is little energy exchange between the primary mass and NES mass, noting the existence of the energy concentration around the low frequencies that are close to the natural frequency of the NES. This is attributed to the fact that the NES is not essentially nonlinear.

Shown in Figure 3.26(b), as the initial energy exceeds the threshold level, the higher frequency components are present at the higher energy level region, revealing by the initial nonlinear beating phenomena. Once the nonlinear beating becomes less dominant, the fundamental TET due to 1:1 transient resonance capture is triggered, as the transient dynamics traces approximately the in-phase backbone branch. This indicates that the energy is gradually localized in the NES.

Figure 3.26(c) shows the case of the medium-high initial energy level, and Figure 3.26(d) the case of the high initial energy level. The higher frequency components still appear, and however only last for a short period of time at the higher energy level region. The beat-like wavelet transform is significantly less dominant comparing to the previous case. At those energy levels, the responses are firmly in 1:1 resonance and attracted to the S_{11+} backbone curve. The energy is rapidly transferred to the NES.

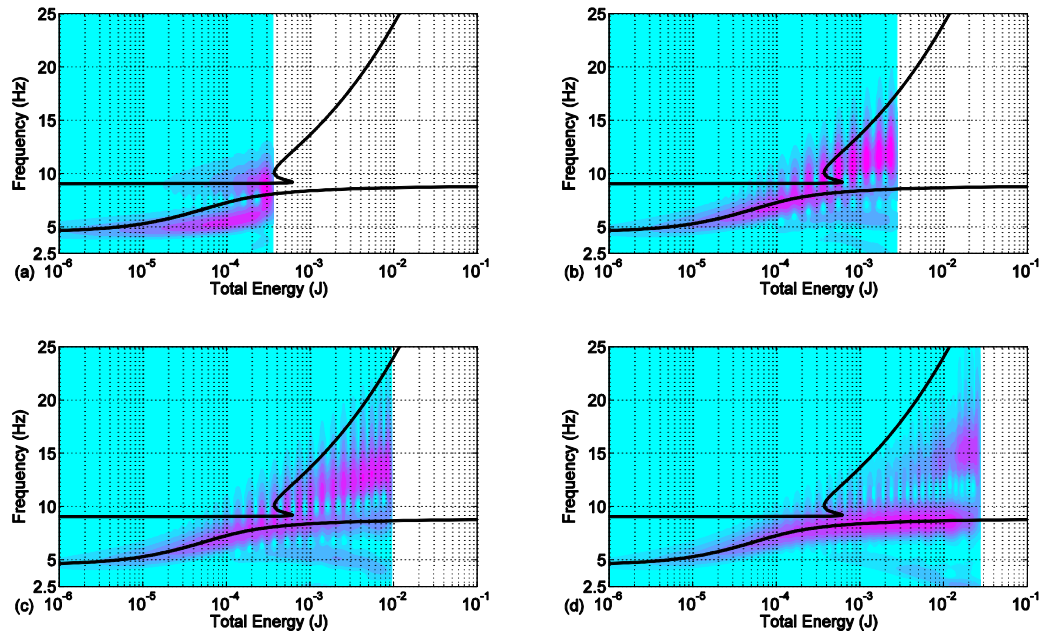


Figure 3.26 Frequency energy plots and wavelet transform of relative displacement $x_a - x_p$ from the simulation results for $f_p = 9$ Hz: (a) low initial energy $X = 0.52 \times 10^{-3}$ (m); (b) medium initial energy $X = 1.42 \times 10^{-3}$ (m); (c) medium-high initial energy $X = 2.65 \times 10^{-3}$ (m) and (d) high initial energy $X = 4.45 \times 10^{-3}$ (m).

Figure 3.27 shows the experimental results. As shown in Figure 3.27(a), for the initial energy level that is below the energy threshold, the energy is primarily concentrated around f_p and f_a , respectively, that is similar to that revealed in Figure 3.26(a). As shown in Figure 3.27(b), when the initial energy level increases above the energy threshold, higher frequency components are present at higher energy region. As a result, the energy is concentrated along the backbone curve S_{11+} .

Figure 3.27(c) and Figure 3.27(d) show the case of the medium-high and high initial energy level, respectively. The higher frequency components appear but are not dominant

comparing to low frequency components. It can still be seen that the energy is concentrated primarily along the backbone curve $S11+$, and the nonlinear beating effect is not apparently present in these plots. This indicates that the TET is activated. As the time progresses, the energy is reduced by following the backbone curve $S11+$. This indicates that the energy is gradually localized in the NES.

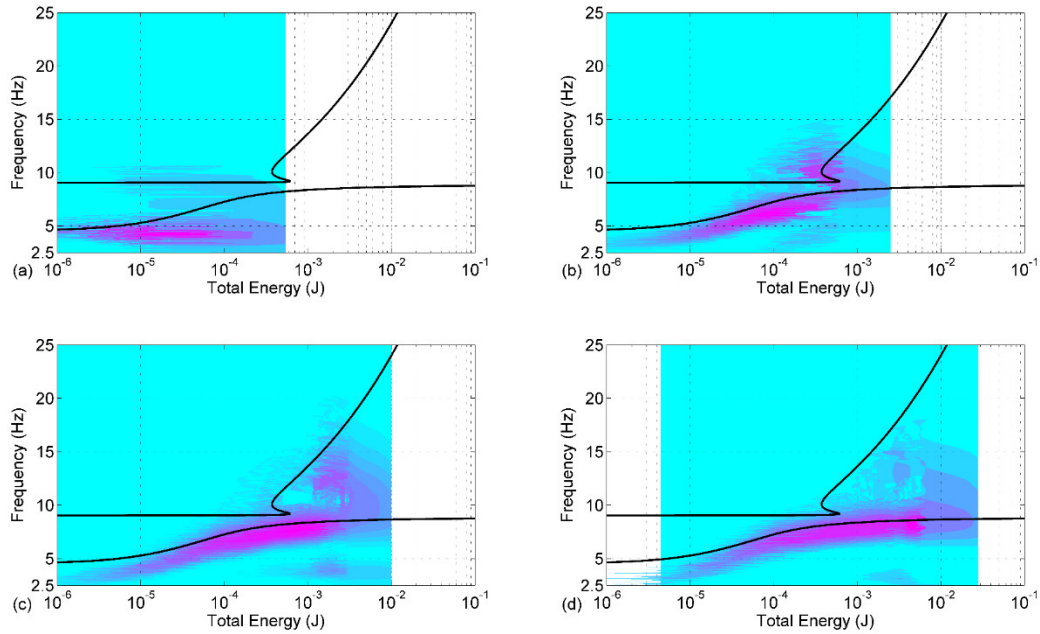


Figure 3.27 Frequency energy plots and wavelet transforms of relative displacement $x_a - x_p$ from the experimental results for $f_p = 9$ Hz: (a) low initial energy $X = 0.52 \times 10^{-3}$ (m); (b) medium initial energy $X = 1.42 \times 10^{-3}$ (m); (c) medium-high initial energy $X = 2.65 \times 10^{-3}$ (m) and (d) high initial energy $X = 4.45 \times 10^{-3}$ (m).

Figure 3.28 shows the simulation results for $f_p = 15$ Hz. As shown in Figure 3.28(a), for the initial energy level which is much lower than the energy threshold, the energy is primarily concentrated around f_a and f_p , respectively. Figure 3.28(b) shows the case for the medium initial energy level. It is observed that in the beginning, the system's energy is primarily concentrated around f_p . It is also noted that as the initial energy level gets close to the energy threshold, the oscillation energy quickly switches to a curve that is bent toward to the in-phase backbone curve $S11+$. However, the NES is not yet fully activated. Figure 3.28(c) shows the case that the initial energy level gets just above the energy threshold level. It can be seen that the NES is now activated and the vibration energy follows the $S11+$ curve. However,

the nonlinear beating phenomenon appears at the beginning. Figure 3.28(d) shows the case for the high initial energy level. Again, the NES is activated. The nonlinear beating is less dominant and only lasts a short period of time comparing to Figure 3.28(c). The TET and 1:1 resonance capture are triggered. As a result, the system's energy follows the $S11+$ curve.

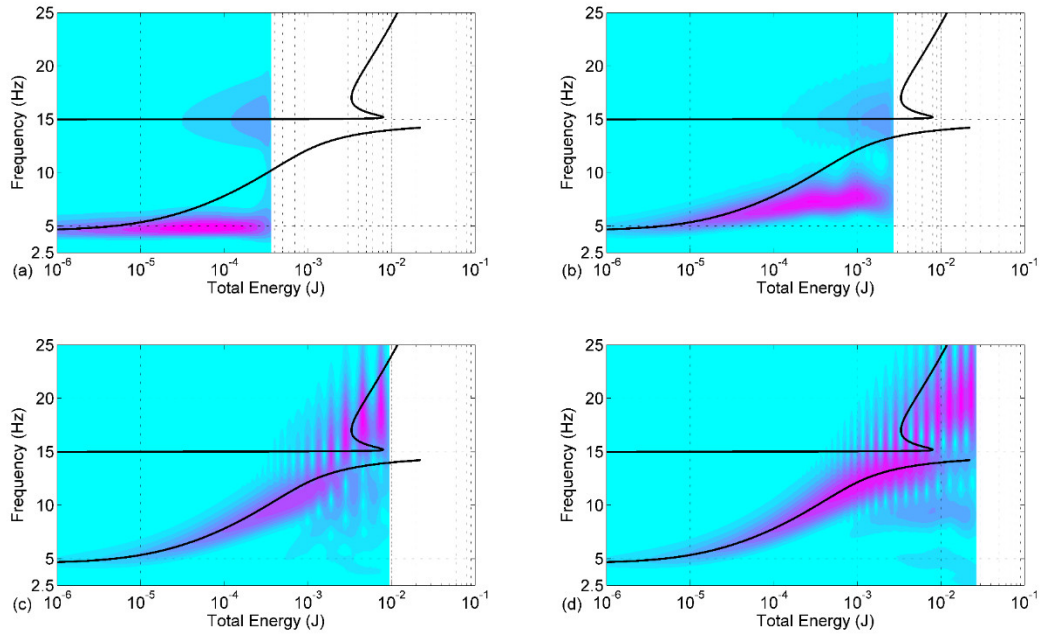


Figure 3.28 Frequency energy plots and wavelet transforms of relative displacement $x_a - x_p$ from the simulation results for $f_p = 15$ Hz: (a) low initial energy $X = 0.312 \times 10^{-3}$ (m); (b) medium initial energy $X = 0.852 \times 10^{-3}$ (m); (c) medium-high initial energy $X = 1.59 \times 10^{-3}$ (m) and (d) high initial energy $X = 2.67 \times 10^{-3}$ (m).

Figure 3.29 shows the experimental results for $f_p = 15$ Hz. Figure 3.29(a) and (b) are similar to the simulation results shown in Figure 3.27(a) and (b). The initial energy levels both are below the energy threshold; hence, the NES is not activated in both the scenarios. As shown in Figure 3.29(c) and (d) when the initial energy level is above the energy threshold and the NES is activated. It can be noted that although the system's energy follows a general trend similar to the in-phase curve $S11+$, there is lag between the energy concentration and backbone curve $S11+$. The reason that causes this lag requires a further investigation.

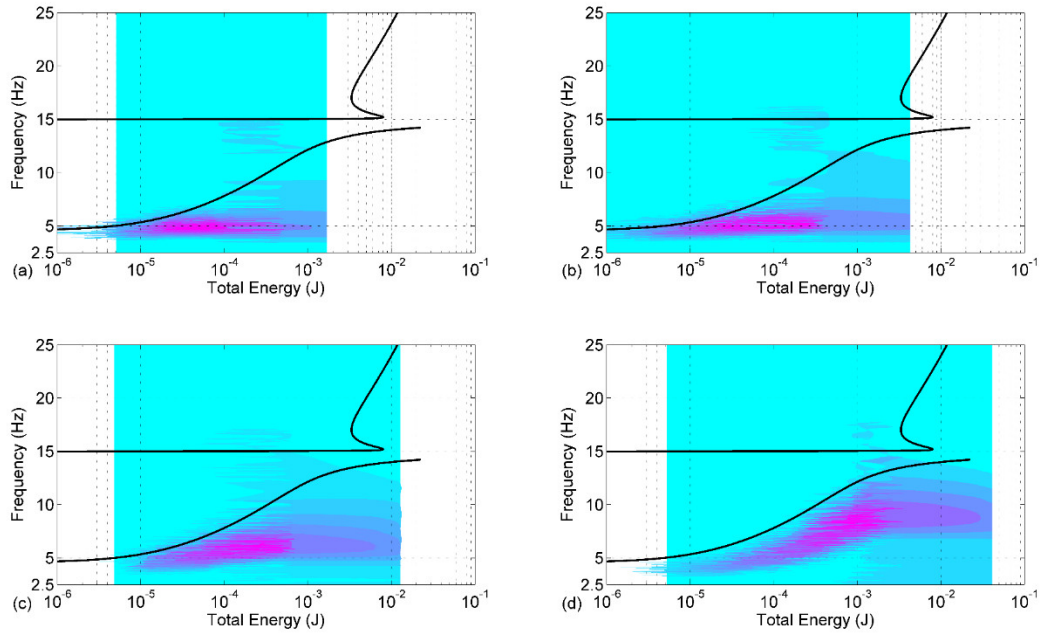


Figure 3.29 Frequency energy plots and wavelet transforms of relative displacement $x_a - x_p$ from the experimental results for $f_p = 15$ Hz: (a) low initial energy $X = 0.312 \times 10^{-3}$ (m); (b) medium initial energy $X = 0.852 \times 10^{-3}$ (m); (c) medium-high initial energy $X = 1.59 \times 10^{-3}$ (m) and (d) high initial energy $X = 2.67 \times 10^{-3}$ (m).

3.6 Conclusion

In this chapter, the transient behaviours of the system are investigated. It has shown that the developed apparatus demonstrates characteristics similar to those of the NES. It has been shown that there is an energy threshold needs to be reached in order to engage the NES in 1:1 resonance, and the initial energy levels slightly greater than the energy threshold has excellent vibration suppression and energy harvesting. Higher initial energy levels also result in excellent performance in system's response and enhancing the energy pumping. It has been also found that the energy threshold increases as the natural frequency of the primary system increases, and it results in higher initial energy level required in order to activate the NES.

Chapter 4 Harmonically forced responses

4.1 Analytical solution of harmonically forced responses

Commonly the method of complexification [59] is used to analyze the harmonically forced responses of the NES systems. With this method, the system dynamics are broken into the slow and fast parts similar to the steps taken in Section 3.4. Assuming a response of 1:1 frequency matching, a harmonic balance method is used to average the response and bifurcation analysis are performed. This method is tedious to implement and the obtained results are difficult to interpret. In the following study, a mixed Multiple Scales/Harmonic Balance Method (MSHBM) proposed in [59] is used to obtain the differential equations describing the steady-state responses of the system subject to a harmonic base excitation. The elegance of this method is that the final equations are presented in the real coordinates. The results also prove to be highly accurate for the purpose of identifying saddle nodes and bifurcations. The equations of motion for the system subject to a base excitation are defined as

$$m_p \ddot{x}_p + c_p \dot{x}_p + k_p x_p - [c_a \dot{z} + k_1 z + k_3 z^3 + \theta V] = -m_p \ddot{y} \quad (4.1)$$

$$m_a (\ddot{z} + \ddot{x}_p) + c_a \dot{z} + k_1 z + k_3 z^3 + \theta V = -m_a \ddot{y} \quad (4.2)$$

$$\frac{V}{R} + C^S \dot{V} - \theta \dot{z} = 0 \quad (4.3)$$

where x_p is the displacement of the primary mass relative to the base, x_a is the displacement of the NES mass relative to the base, and $z = x_a - x_p$ is the displacement of NES relative to the primary mass, $\ddot{y} = -\Omega^2 Y \cos(\Omega t)$ is the acceleration of the base with Ω as the excitation frequency and Y as the amplitude of the base motion.

Introducing a frequency ratio $\omega = \frac{\Omega}{\omega_p}$ where ω_p is the natural frequency of the primary system. And, a dimensionless time scale is introduced as $\tau = \omega_p t$. The derivative of this new time scale is $\frac{d\tau}{dt} = \omega_p$. The derivatives of $x(t)$ with respect to τ are given as follows,

$$x' = \frac{d}{d\tau} x(t) = \frac{dx(t)}{dt} \frac{dt}{d\tau} = \frac{\dot{x}}{\omega_p} \quad (4.4)$$

$$x'' = \frac{d^2}{d\tau^2} x(t) = \frac{d^2 x(t)}{dt^2} \frac{dt^2}{d\tau^2} = \frac{\ddot{x}}{\omega_p^2} \quad (4.5)$$

where $(\bullet)'$ denotes the derivative of $x(t)$ with respect to dimensionless time τ . This yields,

$$\dot{x} = \omega_p x', \quad \ddot{x} = \omega_p^2 x'' \quad (4.6)$$

Substituting Equation (4.6) into Equations (4.1) to (4.3) and also normalize by dividing the mass of the primary system,

$$x_p'' + (\omega^2 + \sigma)x_p + \Lambda x_p' - \lambda(z') - \kappa(z) - \mathbb{K}(z)^3 - \theta V = -\frac{1}{\omega_p^2} y'' \quad (4.7)$$

$$\rho(z'' + x_p'') + \lambda(z') + \kappa(z) + \mathbb{K}(z)^3 + \theta V = -\rho \frac{1}{\omega_p^2} y'' \quad (4.8)$$

$$\frac{V}{R\omega_p} + C^S V' - \theta z' = 0 \quad (4.9)$$

where,

$$\Lambda = \frac{c_p}{m_p \omega_p}, \quad \lambda = \frac{c_a}{m_p \omega_p}, \quad \kappa = \frac{k_1}{m_p \omega_p^2}, \quad \mathbb{K} = \frac{k_3}{m_p \omega_p^2}, \quad \theta = \frac{\Theta}{m_p \omega_p^2}$$

$$\rho = \frac{m_a}{m_p}, \quad \omega = \frac{\Omega}{\omega_p}, \quad \omega_p = \sqrt{\frac{k_p}{m_p}}, \quad \sigma = 1 - \omega^2, \quad z = x_a - x_p$$

Using the method of multiple scale, a small parameter ε is introduced that $\varepsilon \ll 1$. Equations (4.7) to (4.9) are transformed as follows,

$$x_p'' + (\varepsilon\sigma + \omega^2)x_p + \varepsilon\Lambda x_p' - \varepsilon\lambda(z') - \varepsilon\kappa(z) - \varepsilon\mathbb{K}(z)^3 - \varepsilon\theta V = -\varepsilon A_c \cos(\omega\tau) \quad (4.10)$$

$$\varepsilon\rho(z'' + x_p'') + \varepsilon\lambda(z') + \varepsilon\kappa(z) + \varepsilon\mathbb{K}(z)^3 + \varepsilon\theta V = -\varepsilon\rho A_c \cos(\omega\tau) \quad (4.11)$$

$$\varepsilon \frac{V}{R\omega_p} + \varepsilon C^S V' - \varepsilon \theta z' = 0 \quad (4.12)$$

where $A_c = \frac{\Omega^2}{\omega_p^2} Y = \omega^2 Y$.

Following the MSHBM, define the fast and slow time scales $T_0 = \varepsilon^0 \tau = \tau$, $T_1 = \varepsilon \tau$, and $T_2 = \varepsilon^2 \tau$. The derivatives are then changed to:

$$\frac{d}{d\tau} = \frac{dT_0}{d\tau} \frac{\partial}{\partial T_0} + \varepsilon \frac{dT_1}{d\tau} \frac{\partial}{\partial T_1} + \varepsilon^2 \frac{dT_2}{d\tau} \frac{\partial}{\partial T_2} + \dots = D_0 + \varepsilon D_1 + \varepsilon^2 D_2 + \dots \quad (4.13)$$

$$\frac{d^2}{d\tau^2} = D_0^2 + 2\varepsilon D_0 D_1 + \varepsilon^2 (D_1^2 + 2D_0 D_2) + \dots \quad (4.14)$$

Approximate solutions of Equations (4.10) to (4.12) are assumed to be the following formats,

$$\begin{aligned} x_p &= x_{p0}(T_0, T_1, T_2) + \varepsilon x_{p1}(T_0, T_1, T_2) + \dots \\ z &= z_0(T_0, T_1, T_2) + \varepsilon z_1(T_0, T_1, T_2) + \dots \\ V &= v_0(T_0, T_1, T_2) + \varepsilon v_1(T_0, T_1, T_2) + \dots \end{aligned} \quad (4.15)$$

Substituting Equation (4.15) into Equations (4.10) to (4.12), and collecting terms associated with the same order of ε result in

Order of ε^0 :

$$D_0^2 x_{p0} + \omega^2 x_{p0} = 0 \quad (4.16)$$

Order of ε^1 :

$$\begin{aligned} D_0^2 x_{p1} + \omega^2 x_{p1} + \sigma x_{p0} + 2D_0 D_1 x_{p0} + \lambda D_0 x_{p0} - \lambda D_0 z_0 - \kappa z_0 - \mathbb{K} z_0^3 - \theta v_0 \dots \\ + A_c \cos(\omega T_0) = 0 \end{aligned} \quad (4.17)$$

$$\rho(D_0^2 z_0 + D_0^2 x_{p0}) + \lambda D_0 z_0 + \kappa z_0 + \mathbb{K} z_0^3 + \theta v_0 + \rho A_c \cos(\omega T_0) = 0 \quad (4.18)$$

$$v_0 + R\omega_p C^S D_0 v_0 - R\omega_p \theta D_0 z_0 = 0 \quad (4.19)$$

Order of ε^2 :

$$\begin{aligned}
& D_0^2 x_{p2} + D_1^2 x_{p0} + \omega^2 x_{p2} + \Lambda D_0 x_{p1} + \Lambda D_1 x_{p0} + 2D_0 D_1 x_{p1} + \sigma x_1 \dots \\
& - \lambda D_0 z_1 - \lambda D_1 z_0 - 3\mathbb{K}z_0^2 z_1 - \kappa z_1 - \theta v_1 = 0
\end{aligned} \tag{4.20}$$

$$\begin{aligned}
& \rho(D_0^2 z_1 + D_0^2 x_{p1}) + 2\rho D_1 D_0 x_{p0} + 2\rho D_1 D_0 z_0 + \lambda D_0 z_1 + \lambda D_1 z_0 \dots \\
& + 3\mathbb{K}z_0^2 z_1 + \kappa z_1 + \theta v_1 = 0
\end{aligned} \tag{4.21}$$

$$v_0 + R\omega_p C^S (D_0 v_1 + D_1 v_0) - R\omega_p \theta (D_0 z_1 + D_1 z_0) = 0 \tag{4.22}$$

It is observed that there are no nonlinear terms or damping terms in Equation (4.16) for the order of ε^0 . It describes the motion of the undamped primary system that has a solution in the form of:

$$x_{p0}(T_0, T_1, \dots) = A(T_1, T_2, \dots)e^{j\omega T_0} + c.c. \tag{4.23}$$

where $A(T_1, T_2, \dots)$ is unknown complex function, j is the imaginary number and $c.c.$ stands for the complex conjugate. From this point an important assumption must be made regarding the dynamics of the NES. Similar to the transient responses, one can expect that the NES will have a 1:1 internal resonance, and will oscillate with frequency ω . With this assumption, the assumed first order solution for the relative motion is

$$z_0(T_0, T_1, \dots) = B(T_1, T_2, \dots)e^{j\omega T_0} + c.c. \tag{4.24}$$

where $B(T_1, T_2, \dots)$ is unknown complex function. From Equation (4.19), the assumed first-order complete solution for the voltage is given by

$$v_0(T_0, T_1, \dots) = \frac{j\omega\omega_p \theta R}{1 + j\omega\omega_p \theta RC^S} B(T_1, T_2, \dots)e^{j\omega T_0} + E(T_1, T_2, \dots)e^{-\frac{T_0}{RC^S}} + c.c. \tag{4.25}$$

It is noted that the first term and second term on the right-hand side of the above equation are the particular solution and homogenous solution to Equation (4.19), respectively.

Substituting Equations (4.23), (4.24), and (4.25) into Equations (4.17) and (4.18) yields,

$$A' = \frac{1}{4\omega} \left(\begin{array}{l} 2j\sigma A + 2\lambda B\omega - 2\Lambda A\omega + jA_c - 6jKB^2\bar{B} - 2j\kappa B\dots \\ + 2\theta \frac{j\omega\omega_p\theta R}{1+j\omega\omega_p\theta C^S} B \end{array} \right) \quad (4.26)$$

$$\begin{aligned} & (\lambda + 2j\rho\omega)B' + 2j\rho A'\omega + 3KB^2\bar{B} + (-\rho\omega^2 + j\lambda\omega + \kappa)B\dots \\ & -\rho A\omega^2 + \theta \frac{j\omega\omega_p\theta R}{1+j\omega\omega_p\theta C^S} B + \frac{1}{2}\rho A_c = 0 \end{aligned} \quad (4.27)$$

Note that in the above substitution, the homogenous solution in Equation (4.25) was dropped as the steady-state solutions are sought. The terms $A(T_1, T_2, \dots)$ and $B(T_1, T_2, \dots)$ in Equations (4.23) and (4.24) are assumed to have the form of the following format:

$$A(T_1, T_2, \dots) = \frac{1}{2}a(T_1, T_2, \dots)e^{j\alpha t} \quad (4.28)$$

$$B(T_1, T_2, \dots) = \frac{1}{2}b(T_1, T_2, \dots)e^{j\beta t} \quad (4.29)$$

Equations (4.28) and (4.29) describe the real amplitudes of the primary system and the relative displacement (a, b) and (α, β) is the phase of each respectively. Substituting Equations (4.28) and (4.29) into Equations (4.26) and (4.27), and it yields,

$$\begin{aligned} 8(\dot{a} + ja\dot{\alpha})\omega e^{j\alpha t} = & \left[-3jKb^3 + \left(4\lambda\omega - 4j\kappa + 4\theta \frac{j\omega\omega_p\theta R}{1+j\omega\omega_p\theta C^S} \right) b \right] e^{j\beta t} \dots \\ & + 4a(j\alpha - \Lambda\omega)e^{j\alpha t} + 4jA_c \end{aligned} \quad (4.30)$$

$$\frac{1}{4b} \left[\begin{array}{l} 8\omega \left(-\frac{1}{2}a\omega + j\dot{a} - a\dot{\alpha} \right) \rho e^{-j(\beta-\alpha)t} + 4(-2\rho\omega + j\lambda)b\dot{\beta}\dots \\ + (4\lambda + 8j\rho\omega)\dot{b}\dots \\ + 4 \left(\frac{3}{4}b^2K - \rho\omega^2 + \kappa + j\lambda\omega + \theta \frac{j\omega\omega_p\theta R}{1+j\omega\omega_p\theta C^S} \right) b + 4\rho A_c e^{-j\beta t} \end{array} \right] = 0 \quad (4.31)$$

Separating Equations (4.30) and (4.31) into the real and imaginary parts and solving for the derivatives of each term, complex amplitude modulation equations (AME) ruling the slow dynamics of the primary system and NES can be obtained,

$$\begin{aligned} \dot{a} = & \frac{1}{8} \left(\frac{-3b^3\kappa - 4\kappa b + 4\theta^2 \frac{\omega\omega_p R}{1 + \omega^2\omega_p^2 R^2 C^{S2}} b}{\omega} \right) \sin(\alpha - \beta) \dots \\ & + \frac{\lambda\omega b + \theta^2 \frac{\omega^2\omega_p^2 R^2 C^S}{1 + \omega^2\omega_p^2 R^2 C^{S2}} b}{2\omega} \cos(\alpha - \beta) + \frac{1}{8} \frac{[-4A_c \sin(-\alpha) - 4\Lambda a\omega]}{a\omega} \end{aligned} \quad (4.32)$$

$$\begin{aligned} \dot{\alpha} = & \frac{\lambda\omega b + \theta^2 \frac{\omega^2\omega_p^2 R^2 C^S}{1 + \omega^2\omega_p^2 R^2 C^{S2}} b}{2\omega} \frac{\sin(\alpha - \beta)}{a} \dots \\ & + \frac{1}{8} \left(\frac{-3b^3\kappa - 4\kappa b + 4\theta^2 \frac{\omega\omega_p R}{1 + \omega^2\omega_p^2 R^2 C^{S2}} b}{a\omega} \right) \cos(\alpha - \beta) \dots \\ & + \frac{1}{8} \frac{[4\sigma a + 4A_c \cos(-\alpha)]}{a\omega} \end{aligned} \quad (4.33)$$

$$\dot{b} = -\frac{1}{4} \frac{1}{\lambda^2 + 4\rho^2\omega^2} \left\{ \begin{array}{l} -8\rho \left[\rho\omega^2\Lambda + \frac{1}{2}\lambda(\omega^2 + \sigma) \right] a \cos(\alpha - \beta) \dots \\ -8\rho\omega a \left[(\omega^2 + \sigma)\rho - \frac{1}{2}\Lambda\lambda \right] \sin(\alpha - \beta) \dots \\ +3b \left[\frac{8}{3}\rho^2\omega^2 + \left(\kappa b^2 + \frac{4}{3}\omega^2 + \frac{4}{3}\kappa + \frac{4}{3}\theta^2 \frac{\omega^2\omega_p^2 R^2 C^S}{1 + \omega^2\omega_p^2 R^2 C^{S2}} \right) \rho \dots \right. \\ \left. + \kappa b^2 + \frac{4}{3}\kappa + \frac{4}{3}\theta^2 \frac{\omega^2\omega_p^2 R^2 C^S}{1 + \omega^2\omega_p^2 R^2 C^{S2}} \right] \lambda \end{array} \right\}$$

$$(4.34)$$

$$\dot{\beta} = \frac{1}{2} \frac{1}{\lambda^2 + 4\rho^2\omega^2} \left\{ \begin{array}{l} -4\rho a \left[(\omega^2 + \sigma^2)\rho - \frac{1}{2}\Lambda\lambda \right] \omega \cos(\alpha - \beta) \dots \\ +4\rho a \left[\rho\omega^2\Lambda + \frac{1}{2}\lambda(\omega^2 + \sigma^2) \right] \sin(\alpha - \beta) \dots \\ +3\omega b \left[\left(\frac{4}{3}\kappa + \frac{4}{3}\theta^2 \frac{\omega^2\omega_p^2 R^2 C^S}{1 + \omega^2\omega_p^2 R^2 C^{S2}} + Kb^2 - \frac{4}{3}\omega^2 \right) \rho^2 \dots \right. \\ \left. + \left(Kb^2 + \frac{4}{3}\kappa + \frac{4}{3}\theta^2 \frac{\omega^2\omega_p^2 R^2 C^S}{1 + \omega^2\omega_p^2 R^2 C^{S2}} - \frac{2}{3}\lambda^2 \right) \rho - \frac{2}{3}\lambda^2 \right] \end{array} \right\} \quad (4.35)$$

Equations (4.32) to (4.35) describe the amplitudes and phases for $A(T_1, T_2, \dots)$ and $B(T_1, T_2, \dots)$. These equations need to be solved so that the derivatives on the left-hand sides are equal to zero. Once the solutions are obtained, the steady-state responses can be reconstituted as follows:

$$x_p(t) = a \cos(\Omega t + \alpha) \quad (4.36)$$

$$z(t) = b \cos(\Omega t + \beta) \quad (4.37)$$

$$V(t) = \frac{\omega\omega_p\theta R}{\sqrt{1 + (\omega\omega_p RC^S)^2}} z(t) = \frac{\Omega\theta R}{\sqrt{1 + (\Omega RC^S)^2}} b \cos(\Omega t + \beta) \quad (4.38)$$

4.2 Simulation results

4.2.1 Frequency response plot

Equations (4.32) to (4.35) are a set of coupled highly nonlinear differential equations with multiple solutions at different excitation frequencies. In this study, the continuation software Matcont [60] is used to solve them. The use of the software involves finding the steady-state solutions to Equations (4.32) to (4.35), and then finding neighboring equilibrium points by continuing with a single parameter, in this case the forcing frequency. By sweeping the forcing

frequency forward and backward, respectively the so-called frequency response plot (FRP) can be generated. The advantage of such an approach lies in the fact that during continuation, stability can be determined from the eigenvalues of the system equations, as well as determining the type of bifurcation at points of lost stability. In this section, Matcont simulation results are presented.

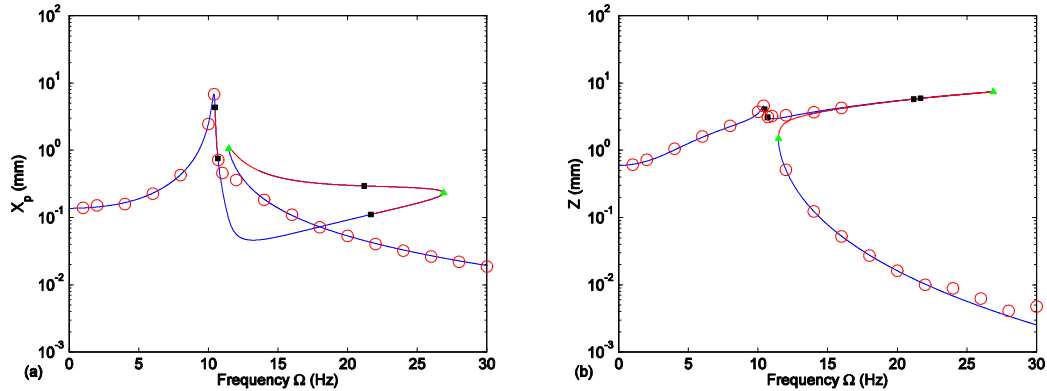


Figure 4.1 FRP for $A_y = 0.6 \text{ m/s}^2$ and $R = 1000 \Omega$: (a) primary displacement X_p and (b) relative displacement Z . Blue line indicates stable periodic orbits. Red lines are unstable indicating non-periodic orbits. Black squares are Hopf bifurcation points and green triangles are Limit points. Red circles are from numerical integration of Equations (4.1) to (4.3)

The parameter values obtained in Chapter 2 are used in the Matcont solution. In addition to specifying the frequency sweeping range, the excitation amplitude $A_y = \Omega^2 Y$ and the load resistance R are given. Figure 4.1 shows the FRPs with $A_y = 0.6 \text{ m/s}^2$ and $R = 1000 \Omega$. In the figures the following conventions are used, the blue line indicates the stable solutions, the red line indicates the unstable solutions, the green triangle symbols represent the limit points, and it is noted that between these two points there exists multiple solutions at a same excitation frequency. The curve between the limit points shown in red colour are obtained only through numerical integration, being an unstable saddle region. In real applications, responses will be attracted to one of the other two points at the same frequency. The black squares indicate the Hopf bifurcation points. The responses within this unstable region is modulated periodic ones.

To verify the solutions obtained by Matcont, Equations (4.1) to (4.3) are numerically integrated using Matlab ODE45 function. The Matcont simulation results show multiple solutions at frequency range from 11.46 to 26.9 Hz, and it is possible to obtain from numerical

integration from Matlab ODE45 by carefully choosing initial conditions. However, it would require numerous attempts. Therefore, Monte Carlo method [36] is used to seek these multiple steady-state responses throughout the frequency sweeping region. With 50 sets of randomly generated initial conditions fed into Matlab ODE45 for numerical integration, the system responses are obtained. It is observed that in general there exist two groups of responses: low amplitude and high amplitude. Therefore, along the Monte Carlo method, these responses are separated the integration results into low and high amplitude for the frequency range where multiple solutions exist. These results are indicated in Figure 4.1(a) and (b) as red circles. In Figure 4.1(b), in the frequency range of 12 to 16 Hz multiple solutions shown in circles are seen. As shown, these multiple solution points are located in two branches: high amplitude branch and low amplitude branch. It is noted that among 50 sets of random initial conditions, only a few sets of the system response belong to high amplitude branch and the rest belong to low amplitude branch. Coexistence of these high and low amplitude solutions are considered to be a typical jumping phenomenon found in harmonically forced responses of nonlinear systems [51]. It is also noted that high amplitude responses in the frequency range of 16 to 27 Hz are not found.

In order to verify the Matcont results, the exciting frequency at $\Omega = 10.58$ Hz, which is within the Hopf bifurcation points, is selected to compare Matcont and Matlab ODE45 results. Therefore, it is expected that the system responses should be so-called strongly modulated response (SMR) [36] shown in Figure 4.2. Figure 4.2(a) shows the primary displacement amplitude a and relative displacement amplitude b , and Figure 4.2(b) shows the reconstituted primary displacement and relative displacement using Equations (4.36) and (4.37). And, Figure 4.2(c) shows Matlab ODE45 numerical integration results of the primary displacement and relative displacement. It shows a good match between Figure 4.2(b) and Figure 4.2(c), and it also shows a sign of strongly modulation response (SMR).

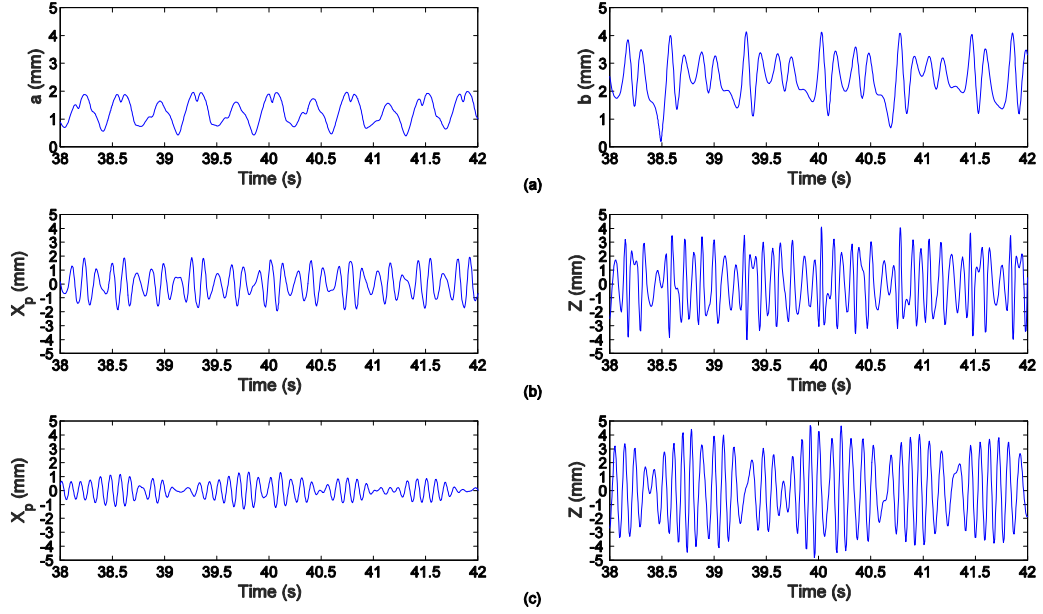


Figure 4.2 Time response of strongly modulated response with $A_y = 0.6 \text{ m/s}^2$, $R = 1000 \Omega$, and $\Omega = 10.58 \text{ Hz}$:
(a) amplitudes by solving Equations (4.32) to (4.35) with Matcont; (b) reconstituted responses defined by Equations (4.36) and (4.37); (c) responses by numerically integrating Equations (4.1) to (4.3).

4.2.2 Frequency sweeping direction

The Matcont solution generates FRPs by sweeping the exciting frequency forward and backward, respectively. Figure 4.3 uses arrows to show the frequency response curve obtained by sweeping the exciting frequency forward. Figure 4.4 shows the case obtained by sweeping the exciting frequency backward. Note that from hereinafter the displacement transmissibility ratio (T.R.) for the primary mass displacement is defined as X_p/X_{pst} while the displacement transmissibility ratio for the NES relative displacement is defined as Z/X_{pst} where $X_{pst} = m_p \Omega^2 Y / k_p$ is the static deflection of the primary spring when a force $m_p \Omega^2 Y$ is applied. As shown in Figure 4.3, both the responses jump from high amplitude to low amplitude when the forward sweeping reaches the right limit point. As shown in Figure 4.4, X_p/X_{pst} jumps to low amplitude while Z/X_{pst} jumps to high amplitude when the backward sweep reaches the left limit point.

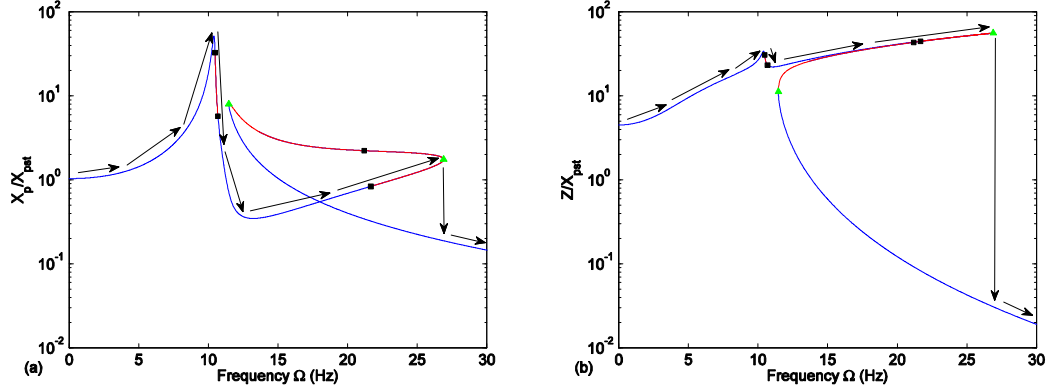


Figure 4.3 FRPs obtained by forward frequency sweeping with $A_y = 0.6 \text{ m/s}^2$: arrows indicate the response path.
 (a) X_p/X_{pst} , (b) Z/X_{pst}

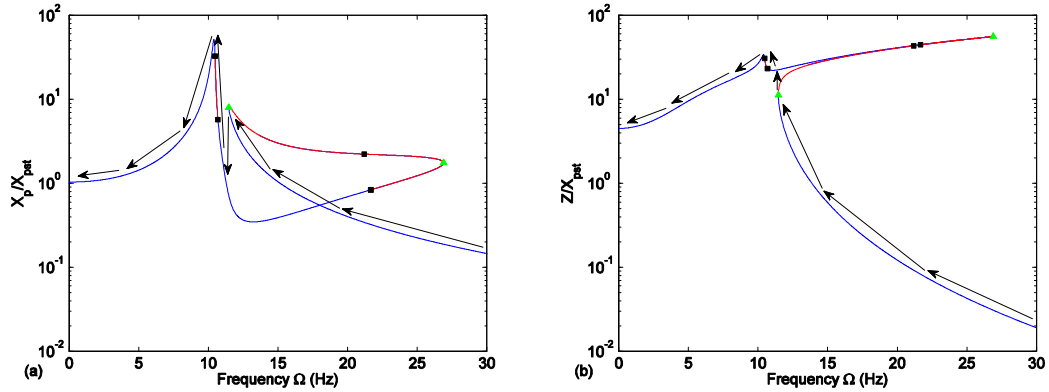


Figure 4.4 FRPs obtained by backward frequency sweeping with $A_y = 0.6 \text{ m/s}^2$: arrows indicate the response path. (a) X_p/X_{pst} , (b) Z/X_{pst}

4.2.3 Interpretation of FRPs

From the previous transient study, it was found that the behaviours of the NES depend on initial energy level. Naturally it is expected that the NES exhibits the similar characteristics under harmonic forcing excitations. Figure 4.5 compares the FRPs for three cases: the green line is the FRP for the primary mass without the NES; curve A is the FRP obtained with a high amplitude excitation of $A_y = 1.8 \text{ m/s}^2$; curve B is the FRP obtained with a low amplitude excitation of $A_y = 0.6 \text{ m/s}^2$. It can be seen that while the NES has little effect on suppression of the peak amplitude, it does reduce the amplitude in the certain frequency region. It is also noted that the NES performs better for the low amplitude excitation than for the high amplitude excitation. Figure 4.6 shows the FRPs for three different acceleration levels: $A_y = 0.6, 1.2, 1.8 \text{ m/s}^2$.

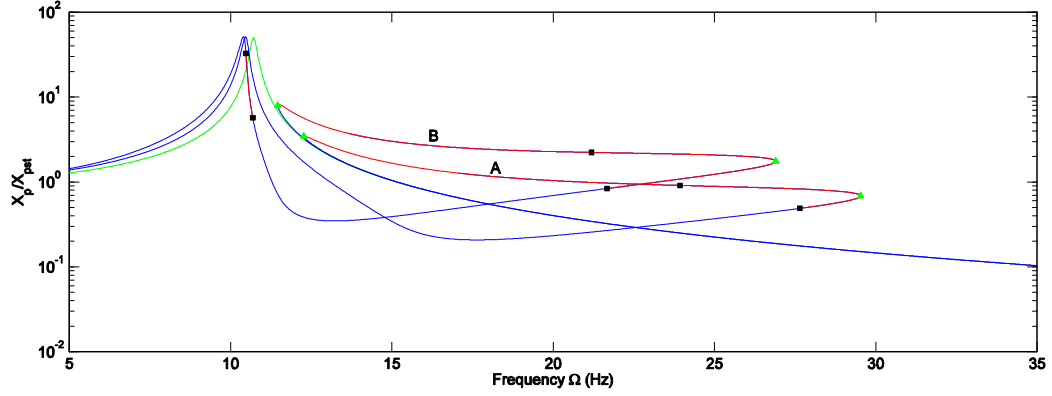


Figure 4.5 Comparison of FRPs for two excitation levels at $R = 1000 \Omega$. Curve A obtained with $A_y = 1.8 \text{ m/s}^2$; curve B obtained with $A_y = 0.6 \text{ m/s}^2$. Green line represents the FRP of the primary system with NES detached.

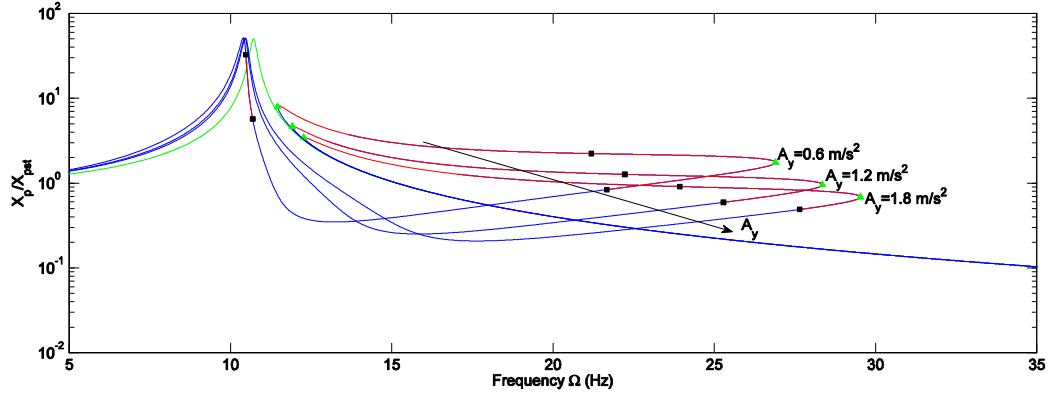


Figure 4.6 Comparison of FRPs for three excitation levels.

Various initial points are selected to test if the Matcont would generate different responses. Before Matcont starts the frequency sweeping continuation, it first conducts a time domain simulation. For the time domain simulation, a set of initial conditions should be provided. In this case, the selected initial conditions are $a = 1 \times 10^{-5}$, $\alpha = 0$, $b = 0$, and $\beta = -3.17$. After 5000 seconds of time domain simulation, Equations (4.32) to (4.35) converge to the steady-states $a = 4.1177 \times 10^{-4}$, $\alpha = 0$, $b = -5.2238 \times 10^{-2}$, and $\beta = -3.1582$. These steady-state values are used for the frequency sweeping to obtain Figure 4.7. It is noted that there exists a closed island of low amplitude comparable to the green line. This closed island consists of a stable solution in the frequency region of 8.19 to 9.56 Hz, and this actually shows a better vibration suppression performance.

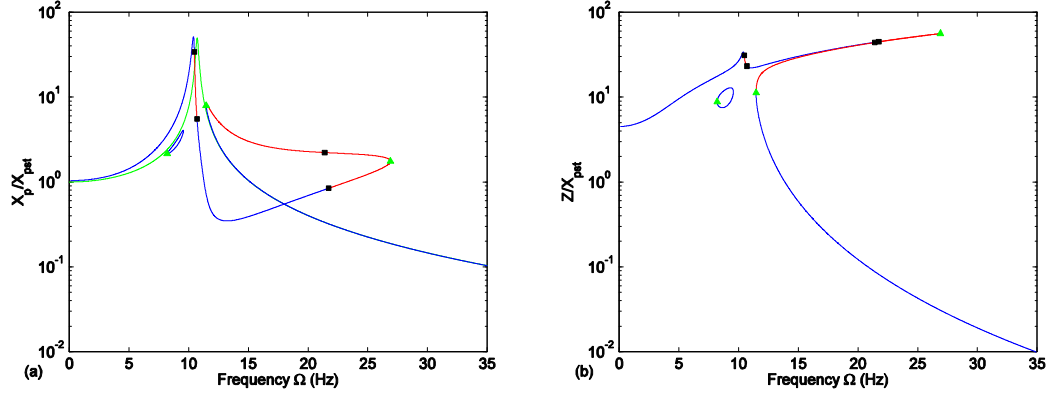


Figure 4.7 Closed island and FRP at $A_y = 0.6 \text{ m/s}^2$. (a) X_p/X_{pst} , (b) Z/X_{pst} . Green line represents the primary system with NES detached.

After finding the closed island at low acceleration $A_y = 0.6 \text{ m/s}^2$, a lower acceleration of $A_y = 0.3 \text{ m/s}^2$ is also attempted to examine if there exists this type of closed island. The steady-state points of $a = 6.5587 \times 10^{-4}$, $\alpha = -1.9105 \times 10^{-1}$, $b = 1.1015 \times 10^{-1}$, and $\beta = -3.2992$ are used for the frequency continuation. A closed island is found and shown in Figure 4.8 in dashed line. Comparing to the previous closed island shown in Figure 4.7, it covers much wider frequency band. This found closed island has a stable solution for the frequency region of 6.59 to 23.49 Hz. It shows better vibration suppression performance from 6.59 to 12.27 Hz. Higher accelerations of $A_y = 1.2$ and 1.8 m/s^2 are also attended and examined under various initial points, however, the closed island is not discovered.

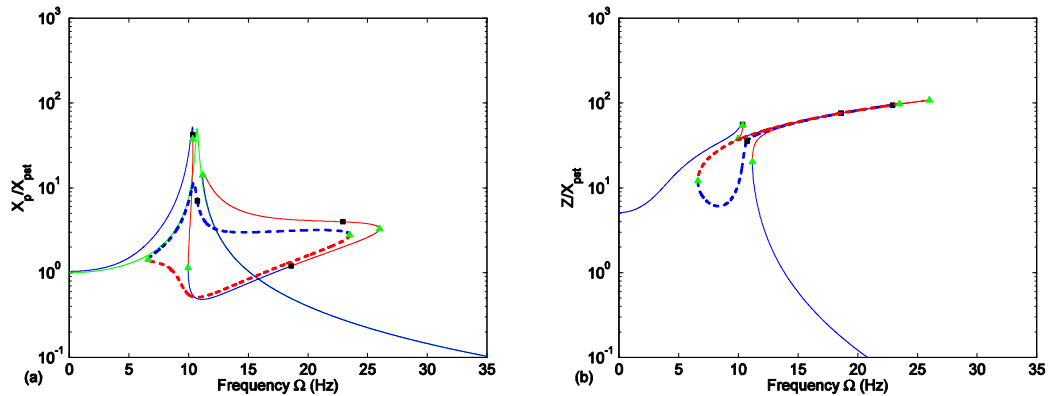


Figure 4.8 Closed island and FRP at $A_y = 0.3 \text{ m/s}^2$. (a) X_p/X_{pst} , (b) Z/X_{pst} . Green line represents the primary system with NES detached.

A group of acceleration levels $A_y = 0.1, 0.2, 0.3, 0.4, 0.5,$ and 0.6 m/s^2 are also examined. Initial conditions and steady-state points for time domain simulation and equilibrium simulation in Matcont are recorded and listed in Table 4.1 and Table 4.2 below.

Table 4.1 Initial condition for Matcont time domain (P_O) simulation.

	Initial condition					
Ω (rad/s)	64.5485	64.5485	64.5485	64.5502	53.4071	56.5487
A_y (m/s ²)	0.1	0.2	0.3	0.4	0.5	0.6
a	0.00001	0.00001	0.00001	0.00001	0.00001	0.00001
α	0	0	0	0	0	0
b	0	0	0	0	0	0
β	-3.17	-3.17	-3.17	-3.17	-3.17	-3.17

Table 4.2 Steady-state point for Matcont equilibrium (EP_EP) simulation.

	Steady-state point					
A_y (m/s ²)	0.1	0.2	0.3	0.4	0.5	0.6
a	2.4024×10^{-4}	4.6708×10^{-4}	6.5587×10^{-4}	6.8349×10^{-4}	2.8049×10^{-4}	4.1177×10^{-4}
α	-2.1020×10^{-1}	-2.0426×10^{-1}	-1.9105×10^{-1}	-1.4896×10^{-1}	-4.0334×10^{-2}	-5.2238×10^{-2}
b	3.3493×10^{-4}	6.8992×10^{-4}	1.1015×10^{-3}	1.7512×10^{-3}	7.3984×10^{-4}	1.0382×10^{-3}
β	-3.3207	-3.3141	-3.2992	-3.2495	-3.1475	-3.1582

In Table 4.2, it is noted that the result of $\alpha - \beta$ is slightly fluctuating around 3.107 on average for the detected closed island at the end of the equilibrium simulation. This indicates that the position of primary mass or NES mass is leading the other.

4.2.4 Energy harvesting

The generated voltage is related to the relative displacement defined in Equation (4.38). The peak power can be determined by the following,

$$P_{peak} = \frac{V^2}{R} \quad (4.39)$$

Substituting Equation (4.38) into Equation (4.39) and converting it back to the physical parameters yield,

$$P_{peak} = \frac{\Omega^2 \theta^2 R}{k_p^2 \left[1 + (\Omega R C^s)^2 \right]} b^2 \quad (4.40)$$

To obtain the maximum peak power, a first order derivative is applied to Equation (4.40) with respect to load resistance R . And, letting the first derivative equal to zero and solving R ,

$$\frac{dP_{peak}}{dR} = \frac{\Omega^2 \theta^2 b^2}{k_p^2 [1 + (\Omega R C^S)^2]} - \frac{2\Omega^4 \theta^2 R^2 C^{S2} b^2}{k_p^2 [1 + (\Omega R C^S)^2]^2} = 0 \quad (4.41)$$

It results in $R = \frac{1}{C^S \Omega}$. This is known as resistive impedance matching [61]. The resistive load value R is found to be inverse proportional to the capacitance of piezoelectric energy harvester C^S and the external excitation frequency Ω to reach maximum generated power. Because the external excitation frequency Ω is changing, this shows that resistive load R should be adjusted accordingly for maximum power.

Matcont simulations are performed under two acceleration levels of $A_y = 0.6$ and 1.8 m/s^2 at various load resistance values $R = 0, 1000, 10^5, 10^7 \Omega$. Figure 4.9 shows the FRP of the relative displacement and the peak power for various resistances at $A_y = 0.6$ m/s^2 . It appears that at $R = 10^5 \Omega$ it has a maximum peak power generated about 0.883 mW at $\Omega = 26.9$ Hz .

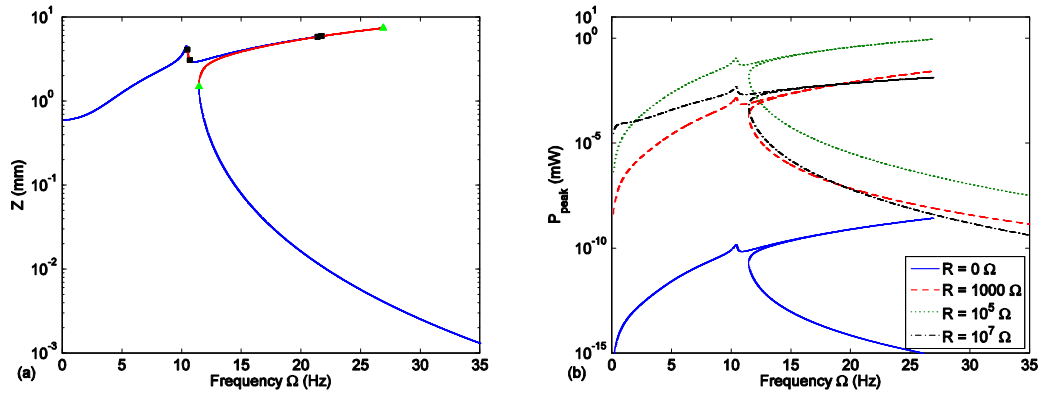


Figure 4.9 Relative displacement and peak power at acceleration $A_y = 0.6$ m/s^2 . (a) FRP for relative displacement and (b) peak power as a function of frequency at $R = 0, 1000, 10^5, 10^7 \Omega$.

Figure 4.10 shows the relative displacement and peak power at $A_y = 1.8$ m/s^2 . Similar to the previous case, it has a maximum peak power generated at $R = 10^5 \Omega$ about 1.135 mW at $\Omega = 29.5$ Hz . Both Figure 4.9 and Figure 4.10 have shown that the optimum load resistance is $R = 10^5 \Omega$ that somewhat agrees with the simulation and experimental results for the transient responses for maximum power in Figure 3.9 and Figure 3.19.

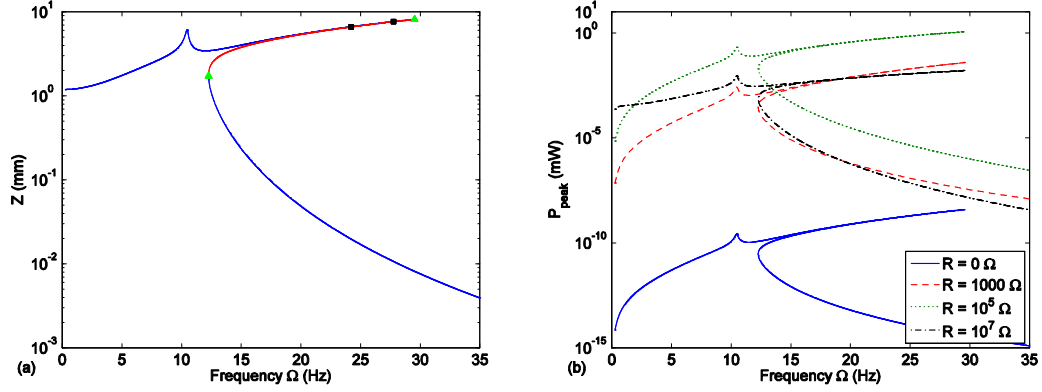


Figure 4.10 Relative displacement and peak power with $A_y = 1.8 \text{ m/s}^2$. (a) FRP for relative displacement and (b) peak power as a function of frequency at $R = 0, 1000, 10^5, 10^7 \Omega$.

4.3 Experiment results

Figure 4.11 shows the testing apparatus setup. Three reflex sensors are mounted vertically to ground to measure the displacements of the NES, primary mass, and the base respectively. An accelerometer is placed on the base to monitor the acceleration. The circuit is connected to the piezoelectric energy harvester, and a potentiometer is used to achieve a required resistance value.

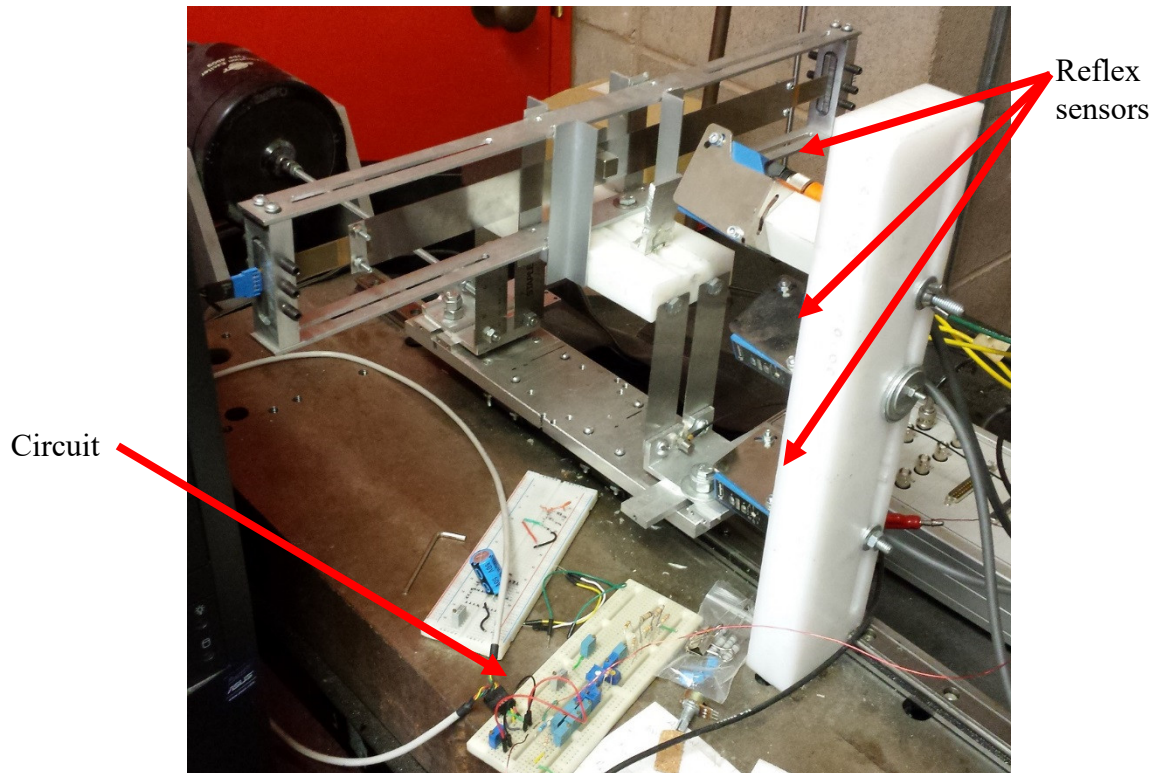


Figure 4.11 Testing apparatus setup

To conduct a sweeping harmonic base excitation, the challenge is to maintain a constant acceleration of the base. The base is mounted on two linear bearings that seat on a precision track. A shaker (Brüel & Kjær shaker model 2809) is used to drive the base through a stinger. A power amplifier (Brüel & Kjær power amplifier model 2718) is used to drive the shaker. By removing the NES mass from the apparatus, a series of tests are conducted to find relationship between voltage signal sent to the power amplifier and base acceleration at each excitation frequency. Three sets of the voltage signal amplitudes vs the exciting frequencies are recorded for acceleration $A_y = 0.6, 1.2, 1.8 \text{ m/s}^2$ correspondingly.

First, the NES mass is detached from the apparatus, a sweep excitation test is conducted. The T.R. X_p/X_{pst} is produced with the measured response of the primary mass. Figure 4.12 compared the measured T.R. (circles) with the analytical one (solid line). It can be seen that there is a good agreement between the experimental T.R. and analytical one.

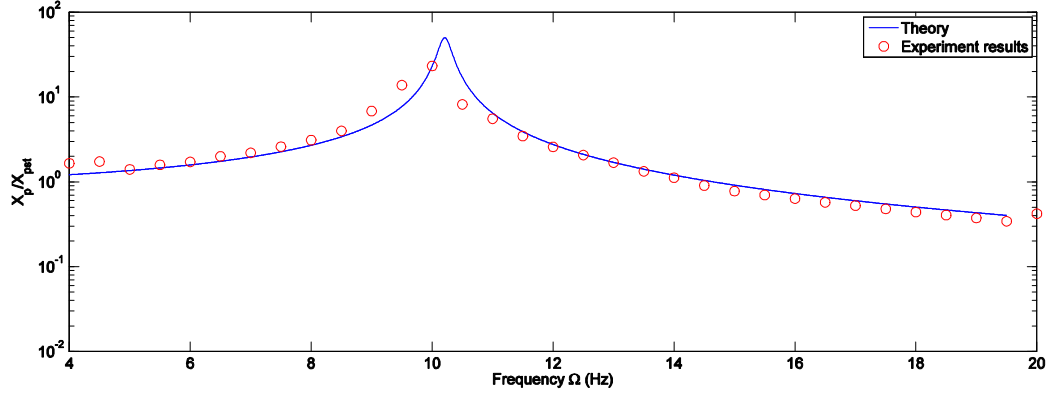


Figure 4.12 Comparison of the analytic T.R. and experimental T.R. of the primary system with $A_y = 0.6 \text{ m/s}^2$.

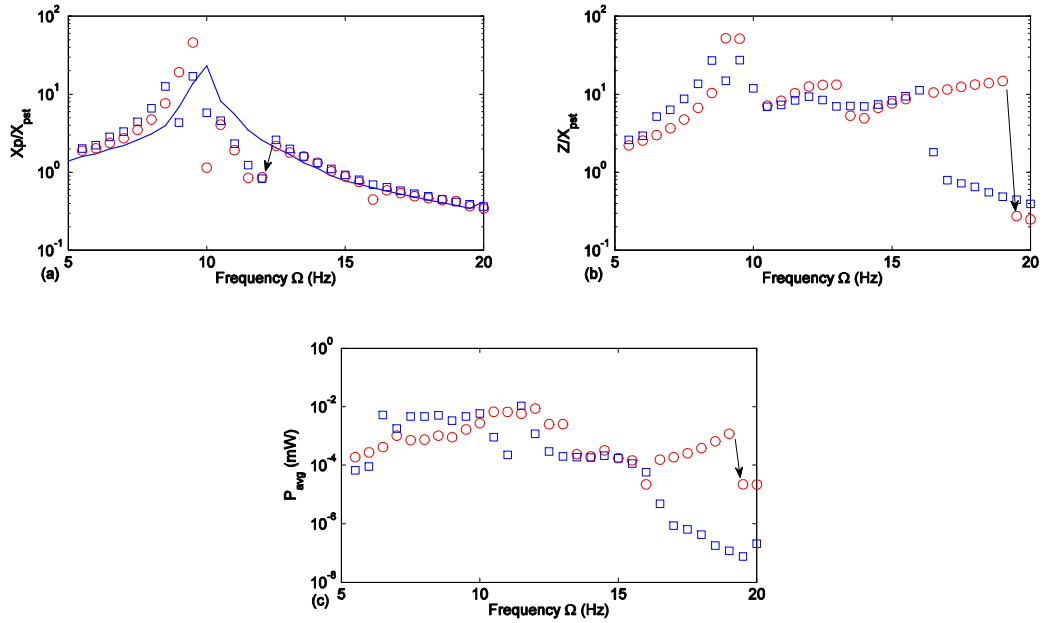


Figure 4.13 Test results with $A_y = 0.6 \text{ m/s}^2$ and $R = 1000 \Omega$. (a) X_p/X_{pst} , blue line indicates the experiment results with the NES removed; (b) Z/X_{pst} ; (c) the average harvested power. (Red circle: forward frequency sweeping; Blue square: backward frequency sweeping.)

With the NES mass attached, the forward and backward sweeping tests are conducted. The forward sweeping test starts from 5 Hz. When the steady-state is reached, the data are saved. With the steady-state kept, the exciting frequency is increased by 0.5 Hz and the voltage signal is adjusted to the corresponding level. Then the steady-state under the new exciting frequency is saved. The process is repeated until the exciting frequency of 20 Hz is reached. The backward sweeping test starts from 20 Hz and the exciting frequency is decreased by 0.5

Hz each time. Figure 4.13 shows the experimental results with acceleration $A_y = 0.6 \text{ m/s}^2$ and $R = 1000 \Omega$. It shows some degrees of vibration suppression around the natural frequency of the primary mass. Figure 4.13(a) shows a jump at around 12.5 Hz in comparison to the Matcont result shown in Figure 4.4(a). Both the results of the T.R. for the relative displacement in the forward and backward frequency sweepings in Figure 4.13(b) are similar to those in Figure 4.4(b). Figure 4.13(c) shows the average power dissipated across the resistor. It shows a peak average power of 0.105 mW at 10 Hz. However, the average peak power is in relative low amplitude, and the jump phenomenon does not appear.

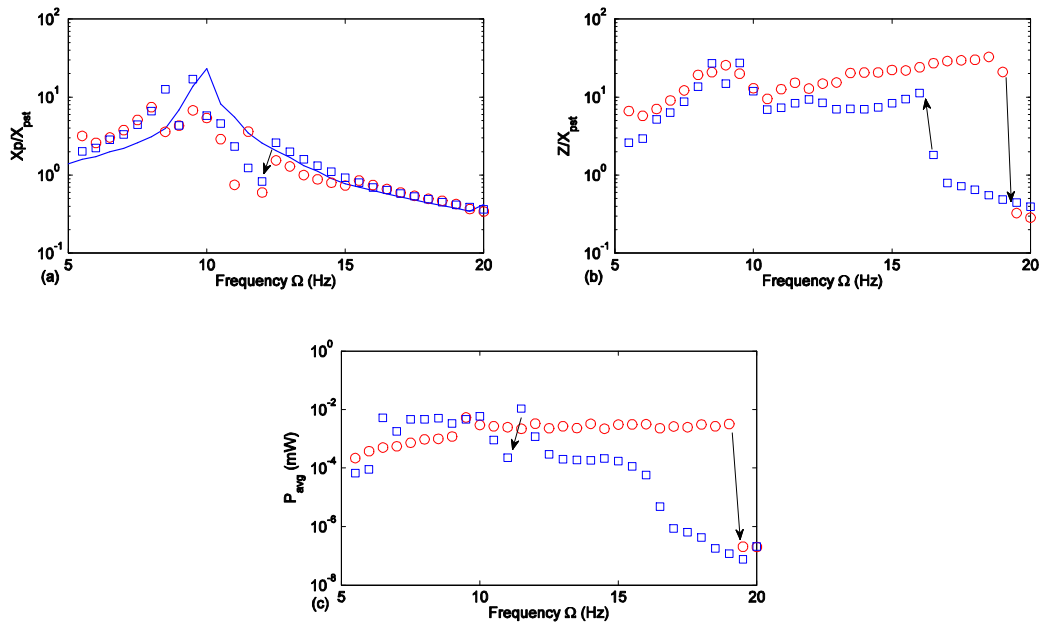


Figure 4.14 Test results with $A_y = 0.6 \text{ m/s}^2$ and $R = 2000 \Omega$. (a) X_p/X_{pst} , blue line indicates experiment results with NES removed; (b) Z/X_{pst} ; (c) the average harvested power. (Red circle: forward frequency sweeping; Blue square: backward frequency sweeping.)

Figure 4.14 shows the results with a high load resistance of $R = 2000 \Omega$. As shown in Figure 4.14(a), there is a slight vibration suppression around the natural frequency 10.71 Hz of the primary system only. Figure 4.14(a) also shows a jump on the backward frequency sweeping curve at 12.5 Hz. Figure 4.14(b) shows a jump on the forward frequency sweeping curve around 19 Hz, and it is slightly different from the Matcont prediction shown in Figure 4.3(b). On the backward frequency sweeping curve in Figure 4.14(b), the jump occurs at 16.5 Hz which is slightly skewed to the right comparing to the result in Figure 4.4(b). Figure 4.14(b)

shows that the relative displacement ratio stays in the low amplitude branch in the higher frequency region and a jump occurs when the exciting frequency is reduced from 16 Hz to 15.5 Hz. Figure 4.14(c) shows the average power dissipated across the resistor, and the dissipated power is low comparing to Figure 4.9(c). It shows a peak average power of 0.00536 mW at 9.5 Hz. It is also noted that changing of resistance does not affect the displacement ratios much.

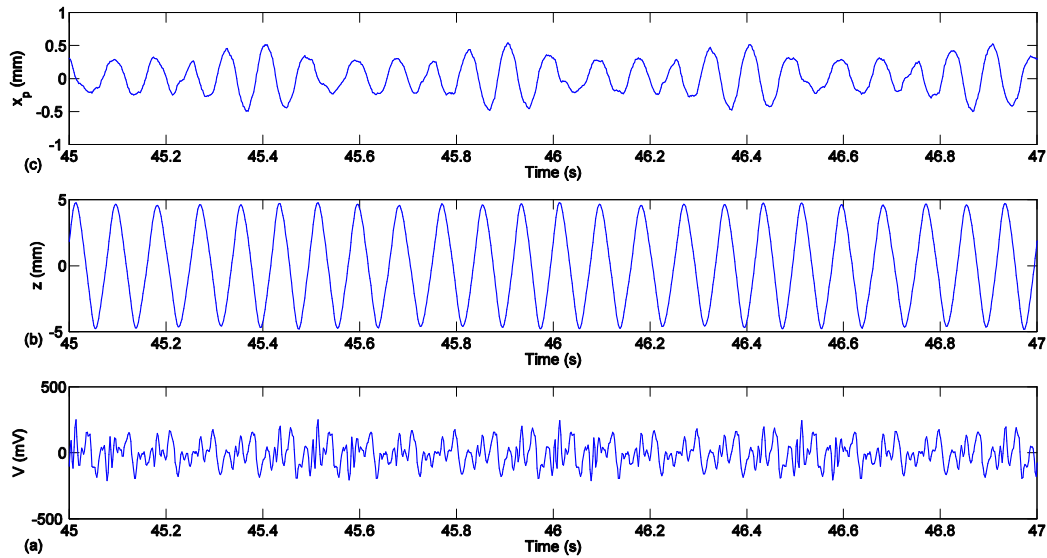


Figure 4.15 Experiment results of displacement response at acceleration $A_y = 0.6 \text{ m/s}^2$ and $R = 2000 \Omega$ and excitation frequency $\Omega = 12 \text{ Hz}$.

As pointed out, the strongly modulated response (SMR) [36] occurs when the exciting frequency falls within the Hopf bifurcation points. Figure 4.15 shows the time responses when the system is excited at 12 Hz. The primary mass displacement appears to be the SMR while the relative displacement appears in a weakly modulated response. It is noted that in the experiments, such the SMR only occurs occasionally.

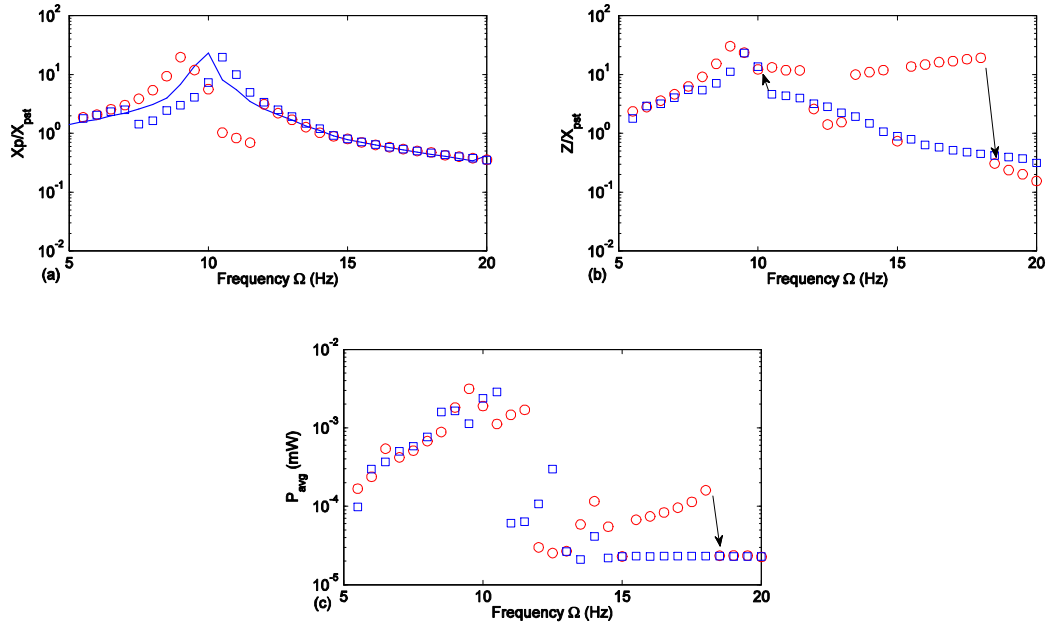


Figure 4.16 Test results with $A_y = 1.2 \text{ m/s}^2$ and $R = 1000 \Omega$. (a) X_p/X_{pst} , blue line indicates experiment results with NES removed; (b) Z/X_{pst} ; (c) the average harvested power. (Red circle: forward frequency sweeping; Blue square: backward frequency sweeping.)

Figure 4.16 shows the results with $A_y = 1.2 \text{ m/s}^2$, and the amplitudes experiences jumps in both the forward and backward frequency sweepings as predicted by the Matcont solution. Figure 4.17 shows the results with $A_y = 1.8 \text{ m/s}^2$. As shown in Figure 4.17(a) with the backward frequency sweeping, the primary mass displacement ratio experiences a jump at 13 Hz. As shown in Figure 4.17(b), with the forward frequency sweeping, the amplitudes jump from high amplitude to low amplitude at 19 Hz. However, jump is not observed in the as shown in Figure 4.17(c) in the forward frequency sweeping. The maximum power peaks 0.0107 mW at 11.5 Hz which is around the resonance frequency of the primary mass.

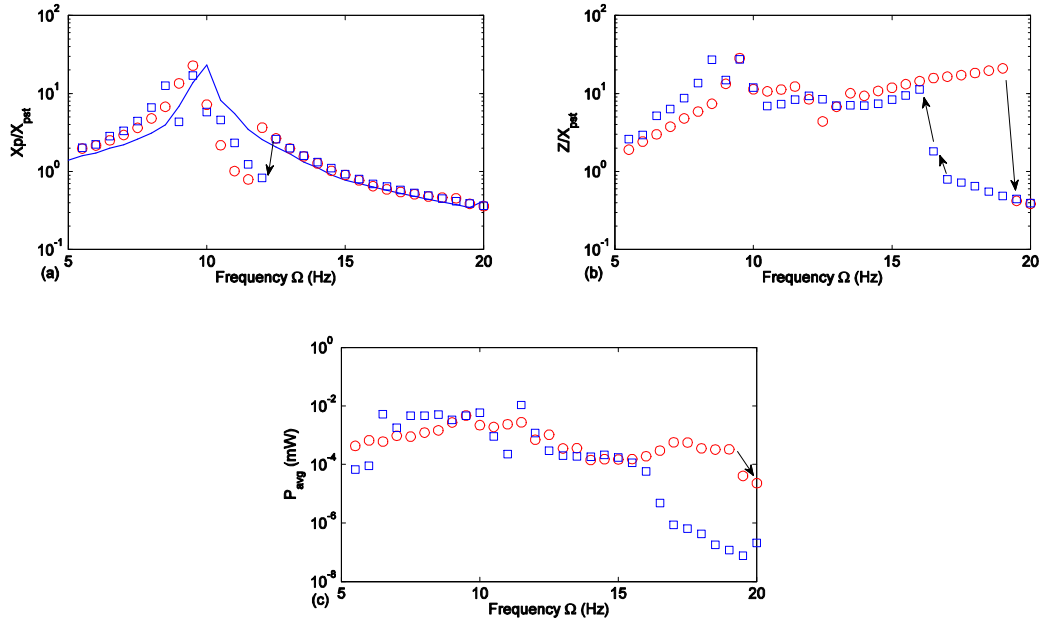


Figure 4.17 Test results with $A_y = 1.8 \text{ m/s}^2$ and $R = 1000 \Omega$. (a) X_p/X_{pst} , blue line indicates experiment results with NES removed; (b) Z/X_{pst} ; (c) the average harvested power. (Red circle: forward frequency sweeping; Blue square: backward frequency sweeping.)

4.4 Conclusion

The harmonically forced responses of the system have been investigated. The approximate analytical solutions of the steady-state responses have been derived using the MSHBM. The Matcont has been used to obtain the FRPs. These FRPs reveal the characteristics of the harmonically forced responses including the excitation level dependence, limit points, Hopf bifurcation points, amplitude jumping, strongly modulated response, etc. The power obtained by the piezoelectric energy harvester has been also examined. An experimental study has been conducted. The experimental results somewhat agree with the Matcont results. At high excitation levels, the experimental results match better with the Matcont results than those at low excitation levels. The typical behaviours such as amplitude jumping and strongly modulated responses have been observed.

Chapter 5 Conclusion

The intended goal of this study is to use the nonlinear energy sink (NES) for energy harvesting and vibration suppression. For this purpose, an apparatus has been developed. The apparatus description, system modeling and parameter identification have been addressed in Chapter 2. The key findings are as follows. The NES spring possesses a cubic nonlinearity consisting of a linear term and nonlinear term. By compressing the NES beam axially, the linear term can be minimized so that the NES's natural frequency is much smaller than the primary system's one. Therefore, the NES system is weakly coupled to the primary system. It has been shown that the electromechanical coupling coefficient θ is a link between the mechanical system and electric system.

The transient behaviours of the system have been investigated in Chapter 3. It has been shown that the developed apparatus demonstrates characteristics similar to those of the NES. There is an energy threshold needed to be reached in order to engage the NES in 1:1 resonance, and the initial energy levels slightly greater than the energy threshold has excellent vibration suppression and energy harvesting. Higher initial energy levels also result in excellent performance in the system's response and enhancing the energy pumping. It has been also found that the energy threshold increases as the natural frequency of the primary system increases, and it results in higher initial energy level required in order to activate the NES.

The harmonically forced responses of the system have been investigated in Chapter 4. The approximate analytical solutions of the steady-state responses have been derived using the MSHBM. The Matcont has been used to obtain the FRPs. These FRPs reveal the characteristics of the harmonically forced responses including the excitation level dependence, limit points, Hopf bifurcation points, amplitude jumping, strongly modulated response, etc. The power obtained by the piezoelectric energy harvester has been also examined. An experimental study has been conducted. The experimental results somewhat agree with the Matcont results. At high excitation levels, the experimental results match better with the Matcont results than those at low excitation levels. The typical behaviours such as amplitude jumping and strongly modulated responses have been observed.

Future work may include to optimize the testing apparatus. The current setup requires a skillful adjustment to properly control the beam buckling state. If the beam is compressed inappropriately, a bi-stable state may result. A better clamping device should be sought. An ideal clamping device should allow a better beam tension control when it is loosened and achieve a secure clamped-clamped support when it is tightened.

References

- [1] Beeby, S.P., Torah, R.N., Tudor, M.J., Glynne-Jones, P., O'Donnell, T., Saha, C.R. and Roy, S., 2007. A micro electromagnetic generator for vibration energy harvesting. *Journal of Micromechanics and Microengineering*, 17(7), pp.1257-1265.
- [2] Beeby, S.P., Tudor, M.J. and White, N.M., 2006. Energy harvesting vibration sources for microsystems applications. *Measurement Science and Technology*, 17(12), pp.175-195.
- [3] Unruh, J.F., 1988. Structure-borne noise control for propeller aircraft. *Journal of Aircraft*, 25(8), pp.752-757.
- [4] Johnson, C.D., 1995. Design of passive damping systems. *Journal of Vibration and Acoustics*, 117(B), pp.171-176.
- [5] Sun, J.Q., Jolly, M.R. and Norris, M.A., 1995. Passive, adaptive and active tuned vibration absorbers—a survey. *Journal of Mechanical Design*, 117(B), pp.234-242.
- [6] Williams, K., Chiu, G. and Bernhard, R., 2002. Adaptive-passive absorbers using shape-memory alloys. *Journal of Sound and Vibration*, 249(5), pp.835-848.
- [7] Inman, D. J., *Engineering Vibration*. Upper Saddle River, N.J.: Pearson Prentice Hall, 2008.
- [8] Den Hartog, J.P., *Mechanical Vibrations*. Courier Corporation, 1985.
- [9] Gendelman, O.V., Starosvetsky, Y. and Feldman, M., 2008. Attractors of harmonically forced linear oscillator with attached nonlinear energy sink I: Description of response regimes. *Nonlinear Dynamics*, 51(1-2), pp.31-46.
- [10] Starosvetsky, Y. and Gendelman, O.V., 2008. Attractors of harmonically forced linear oscillator with attached nonlinear energy sink. II: Optimization of a nonlinear vibration absorber. *Nonlinear Dynamics*, 51(1-2), pp.47-57.
- [11] Starosvetsky, Y. and Gendelman, O.V., 2009. Vibration absorption in systems with a nonlinear energy sink: nonlinear damping. *Journal of Sound and Vibration*, 324(3), pp.916-939.
- [12] Nayfeh, A. H. and Mook, D. T., *Nonlinear Oscillations*. New York; Toronto: Wiley, 1979.

- [13] Gendelman, O., Manevitch, L.I., Vakakis, A.F. and M'closkey, R., 2001. Energy pumping in nonlinear mechanical oscillators: Part I—Dynamics of the underlying Hamiltonian systems. *Journal of Applied Mechanics*, 68(1), pp.34-41.
- [14] Vakakis, A.F. and Gendelman, O., 2001. Energy pumping in nonlinear mechanical oscillators: part II—Resonance Capture. *Journal of Applied Mechanics*, 68(1), pp.42-48.
- [15] Gourdon, E., Alexander, N.A., Taylor, C.A., Lamarque, C.H. and Pernot, S., 2007. Nonlinear energy pumping under transient forcing with strongly nonlinear coupling: Theoretical and experimental results. *Journal of Sound and Vibration*, 300(3), pp.522-551.
- [16] Gourdon E, Lamarque C, Pernot S (2007), Contribution to efficiency of irreversible passive energy pumping with a strong nonlinear attachment, *Nonlinear Dynamics*, 50, pp.793-808.
- [17] Ottman, G.K., Hofmann, H.F. and Lesieutre, G.A., 2003. Optimized piezoelectric energy harvesting circuit using step-down converter in discontinuous conduction mode. *IEEE Transactions on Power Electronics*, 18(2), pp.696-703.
- [18] Lallart, M. and Guyomar, D., 2008. An optimized self-powered switching circuit for nonlinear energy harvesting with low voltage output. *Smart Materials and Structures*, 17(3), pp.035030.
- [19] Ramadass, Y.K. and Chandrakasan, A.P., 2010. An efficient piezoelectric energy harvesting interface circuit using a bias-flip rectifier and shared inductor. *IEEE Journal of Solid-State Circuits*, 45(1), pp.189-204.
- [20] Quinn, D.D., Gendelman, O., Kerschen, G., Sapsis, T.P., Bergman, L.A. and Vakakis, A.F., 2008. Efficiency of targeted energy transfers in coupled nonlinear oscillators associated with 1: 1 resonance captures: Part I. *Journal of Sound and Vibration*, 311(3), pp.1228-1248.
- [21] Sapsis, T.P., Vakakis, A.F., Gendelman, O.V., Bergman, L.A., Kerschen, G. and Quinn, D.D., 2009. Efficiency of targeted energy transfers in coupled nonlinear oscillators associated with 1: 1 resonance captures: Part II, analytical study. *Journal of Sound and Vibration*, 325(1), pp.297-320.

- [22] Vakakis, A.F., Gendelman, O.V., Bergman, L.A., McFarland, D.M., Kerschen, G. and Lee, Y.S., 2008. *Nonlinear Targeted Energy Transfer in Mechanical and Structural Systems* 156. Springer Science & Business Media.
- [23] Nguyen, T.A. and Pernot, S., 2012. Design criteria for optimally tuned nonlinear energy sinks—Part 1: transient regime. *Nonlinear Dynamics*, 69(1-2), pp.1-19.
- [24] Gatti, G. and Brennan, M.J., 2011. On the effects of system parameters on the response of a harmonically excited system consisting of weakly coupled nonlinear and linear oscillators. *Journal of Sound and Vibration*, 330(18), pp.4538-4550.
- [25] Gatti, G., Kovacic, I. and Brennan, M.J., 2010. On the response of a harmonically excited two degree-of-freedom system consisting of a linear and a nonlinear quasi-zero stiffness oscillator. *Journal of Sound and Vibration*, 329(10), pp.1823-1835.
- [26] Gourdon, E., Alexander, N.A., Taylor, C.A., Lamarque, C.H. and Pernot, S., 2007. Nonlinear energy pumping under transient forcing with strongly nonlinear coupling: Theoretical and experimental results. *Journal of Sound and Vibration*, 300(3), pp.522-551.
- [27] Kerschen, G., McFarland, D.M., Kowtko, J.J., Lee, Y.S., Bergman, L.A. and Vakakis, A.F., 2007. Experimental demonstration of transient resonance capture in a system of two coupled oscillators with essential stiffness nonlinearity. *Journal of Sound and Vibration*, 299(4), pp.822-838.
- [28] Kerschen, G., Kowtko, J.J., McFarland, D.M., Bergman, L.A. and Vakakis, A.F., 2007. Theoretical and experimental study of multimodal targeted energy transfer in a system of coupled oscillators. *Nonlinear Dynamics*, 47(1-3), pp.285-309.
- [29] McFarland, D.M., Bergman, L.A. and Vakakis, A.F., 2005. Experimental study of nonlinear energy pumping occurring at a single fast frequency. *International Journal of Non-Linear Mechanics*, 40(6), pp.891-899.
- [30] Jiang, X., McFarland, D.M., Bergman, L.A. and Vakakis, A.F., 2003. Steady state passive nonlinear energy pumping in coupled oscillators: theoretical and experimental results. *Nonlinear Dynamics*, 33(1), pp.87-102.

- [31] Anton, S.R. and Sodano, H.A., 2007. A review of power harvesting using piezoelectric materials (2003–2006). *Smart Materials and Structures*, 16(3), pp.1-21.
- [32] Yang, Y., Tang, L. and Li, H., 2009. Vibration energy harvesting using macro-fiber composites. *Smart Materials and Structures*, 18(11), pp.115025.
- [33] Gu, L. and Livermore, C., 2010. Passive self-tuning energy harvester for extracting energy from rotational motion. *Applied Physics Letters*, 97(8), pp.081904.
- [34] Lallart, M., Anton, S.R. and Inman, D.J., 2010. Frequency self-tuning scheme for broadband vibration energy harvesting. *Journal of Intelligent Material Systems and Structures*.
- [35] Challa, V.R., Prasad, M.G. and Fisher, F.T., 2011. Towards an autonomous self-tuning vibration energy harvesting device for wireless sensor network applications. *Smart Materials and Structures*, 20(2), pp.025004.
- [36] Tang, L., Yang, Y. and Soh, C.K., 2013. Broadband vibration energy harvesting techniques. In *Advances in Energy Harvesting Methods*, pp.17-61. Springer New York.
- [37] Tang, L., Yang, Y. and Wu, H., 2012, April. Modeling and experiment of a multiple-DOF piezoelectric energy harvester. In *SPIE Smart Structures and Materials+ Nondestructive Evaluation and Health Monitoring*, pp. 83411E-83411E. International Society for Optics and Photonics.
- [38] Arafa, M., Akl, W., Aladwani, A., Aldraihem, O. and Baz, A., 2011, March. Experimental implementation of a cantilevered piezoelectric energy harvester with a dynamic magnifier. In *SPIE Smart Structures and Materials+ Nondestructive Evaluation and Health Monitoring*, pp. 79770Q-79770Q. International Society for Optics and Photonics.
- [39] Jo, S.E., Kim, M.S. and Kim, Y.J., 2011, June. Passive-self-tunable vibrational energy harvester. In *2011 16th International Solid-State Sensors, Actuators and Microsystems Conference*, pp. 691-694. IEEE.
- [40] Kim, I.H., Jung, H.J., Lee, B.M. and Jang, S.J., 2011. Broadband energy-harvesting using a two degree-of-freedom vibrating body. *Applied Physics Letters*, 98(21), pp.214102.

- [41] Wu, H., Tang, L., Yang, Y. and Soh, C.K., 2012. A compact 2 degree-of-freedom energy harvester with cut-out cantilever beam. *Japanese Journal of Applied Physics*, 51(4R), pp.040211.
- [42] Tang, L., Yang, Y. and Soh, C.K., 2012. Improving functionality of vibration energy harvesters using magnets. *Journal of Intelligent Material Systems and Structures*, 23(13) pp.1433-1449.
- [43] Tang, L. and Yang, Y., 2012. A nonlinear piezoelectric energy harvester with magnetic oscillator. *Applied Physics Letters*, 101(9), pp.094102.
- [44] Gammaitoni, L., Neri, I. and Vocca, H., 2009. Nonlinear oscillators for vibration energy harvesting. *Applied Physics Letters*, 94(16), pp.164102.
- [45] Daqaq, M.F., 2010. Response of uni-modal duffing-type harvesters to random forced excitations. *Journal of Sound and Vibration*, 329(18), pp.3621-3631.
- [46] Erturk, A. and Inman, D.J., 2011. Broadband piezoelectric power generation on high-energy orbits of the bistable Duffing oscillator with electromechanical coupling. *Journal of Sound and Vibration*, 330(10), pp.2339-2353.
- [47] Harne, R.L. and Wang, K.W., 2013. A review of the recent research on vibration energy harvesting via bistable systems. *Smart materials and structures*, 22(2), pp.023001.
- [48] Quinn, D.D., Vakakis, A.F. and Bergman, L.A., 2007, January. Vibration-based energy harvesting with essential nonlinearities. In ASME 2007 International Design Engineering Technical Conferences and Computers and Information in Engineering Conference, pp.779-786. American Society of Mechanical Engineers.
- [49] Quinn, D.D., Triplett, A.L., Vakakis, A.F. and Bergman, L.A., 2011. Energy harvesting from impulsive loads using intentional essential nonlinearities. *Journal of Vibration and Acoustics*, 133(1), pp.011004.
- [50] Quinn, D.D., Triplett, A.L., Bergman, L.A. and Vakakis, A.F., 2011. Comparing linear and essentially nonlinear vibration-based energy harvesting. *Journal of Vibration and Acoustics*, 133(1), pp.011001.

- [51] Remick, K., Joo, H.K., McFarland, D.M., Sapsis, T.P., Bergman, L., Quinn, D.D. and Vakakis, A., 2014. Sustained high-frequency energy harvesting through a strongly nonlinear electromechanical system under single and repeated impulsive excitations. *Journal of Sound and Vibration*, 333(14), pp.3214-3235.
- [52] Ahmadabadi, Z.N. and Khadem, S.E., 2014. Nonlinear vibration control and energy harvesting of a beam using a nonlinear energy sink and a piezoelectric device. *Journal of Sound and Vibration*, 333(19), pp.4444-4457.
- [53] Kremer, D. and Liu, K., 2014. A nonlinear energy sink with an energy harvester: Transient responses. *Journal of Sound and Vibration*, 333(20), pp.4859-4880.
- [54] Worden, K., 1990. Data processing and experiment design for the restoring force surface method, part I: integration and differentiation of measured time data. *Mechanical Systems and Signal Processing*, 4(4), pp.295-319.
- [55] Worden, K., 1990. Data processing and experiment design for the restoring force surface method, part II: choice of excitation signal. *Mechanical Systems and Signal Processing*, 4(4), pp.321-344.
- [56] Gendelman, O.V., Sapsis, T., Vakakis, A.F. and Bergman, L.A., 2011. Enhanced passive targeted energy transfer in strongly nonlinear mechanical oscillators. *Journal of Sound and Vibration*, 330(1), pp.1-8.
- [57] Pham, T.T., Pernot, S. and Lamarque, C.H., 2010. Competitive energy transfer between a two degree-of-freedom dynamic system and an absorber with essential nonlinearity. *Nonlinear Dynamics*, 62(3), pp.573-592.
- [58] Bellet, R., Cochelin, B., Herzog, P. and Mattei, P.O., 2010. Experimental study of targeted energy transfer from an acoustic system to a nonlinear membrane absorber. *Journal of Sound and Vibration*, 329(14), pp.2768-2791.
- [59] Luongo, A. and Zulli, D., 2012. Dynamic analysis of externally excited NES-controlled systems via a mixed Multiple Scale/Harmonic Balance algorithm. *Nonlinear Dynamics*, 70(3), pp.2049-2061.

[60] Dhooge, A., Govaerts, W., Kuznetsov, Y.A., Mestrom, W., Riet, A.M. and Sautois, B., 2006. MATCONT and CL MATCONT: Continuation toolboxes in matlab. Universiteit Gent, Belgium and Utrecht University, The Netherlands.

[61] Kong, N.A., Ha, D.S., Erturk, A. and Inman, D.J., 2010. Resistive impedance matching circuit for piezoelectric energy harvesting. *Journal of Intelligent Material Systems and Structures*, pp.1293-1302.

Appendix A

Four equations describe the amplitudes and phases of the system under harmonically forced excitation is returned to physical coordinate and listed below.

$$\begin{aligned}
 \frac{d}{dt} a(t) = & \frac{1}{8} \frac{\left(-\frac{3b^3 k_3}{k_p} - \frac{4k_1 b}{k_p} + \frac{4\theta^2 \Omega R b}{k_p^2 \left((C^S \Omega R)^2 + 1 \right)} \right) \sqrt{\frac{k_p}{m_p}} \sin(\alpha - \beta)}{\Omega} \\
 & + \frac{1}{8} \frac{\left(\frac{c_a \Omega b}{k_p} + \frac{\theta^2 \Omega^2 R^2 C^S b}{k_p^2 \left((C^S \Omega R)^2 + 1 \right)} \right) \sqrt{\frac{k_p}{m_p}} \cos(\alpha - \beta)}{\Omega} \\
 & + \frac{1}{8} \frac{\left(-\frac{4A_y m_p \sin(\alpha)}{k_p} - \frac{4c_p a \Omega}{k_p} \right) \sqrt{\frac{k_p}{m_p}}}{a \Omega}
 \end{aligned} \tag{A.1}$$

$$\begin{aligned}
 \frac{d}{dt} \alpha(t) = & \frac{1}{2} \frac{\left(\frac{c_a \Omega b}{k_p} + \frac{\theta^2 \Omega^2 R^2 C^S b}{k_p^2 \left((C^S \Omega R)^2 + 1 \right)} \right) \sqrt{\frac{k_p}{m_p}} \sin(\alpha - \beta)}{a \Omega} \\
 & + \frac{1}{8} \frac{\left(-\frac{3b^3 k_3}{k_p} - \frac{4k_1 b}{k_p} + \frac{4\theta^2 \Omega R b}{k_p^2 \left((C^S \Omega R)^2 + 1 \right)} \right) \sqrt{\frac{k_p}{m_p}} \cos(\alpha - \beta)}{a \Omega} \\
 & + \frac{1}{8} \frac{\left(4a \left(-\frac{\Omega^2 m_p}{k_p} + 1 \right) - \frac{4A_y m_p \cos(\alpha)}{k_p} \right) \sqrt{\frac{k_p}{m_p}}}{a \Omega}
 \end{aligned} \tag{A.2}$$

$$\begin{aligned}
\frac{d}{dt}b(t) = & -\frac{1}{4} \frac{1}{\frac{4m_a^2\Omega^2}{m_p k_p} + \frac{c_a^2}{m_p k_p}} \left(\frac{8m_a \left(\frac{m_a \Omega^2 c_p}{m_p^2 \left(\frac{k_p}{m_p} \right)^{3/2}} + \frac{1}{2} \frac{c_a}{m_p \sqrt{\frac{k_p}{m_p}}} \right) a \cos(\alpha - \beta)}{m_p} \right. \\
& - \frac{8m_a \Omega a \left(\frac{m_a}{m_p} - \frac{1}{2} \frac{c_p c_a}{m_p k_p} \right) \sin(\alpha - \beta)}{m_p \sqrt{\frac{k_p}{m_p}}} \\
& \left. + \frac{1}{m_p \sqrt{\frac{k_p}{m_p}}} \left(3b + \frac{\left(\frac{8 m_a^2 \Omega^2}{3 m_p k_p} + \frac{\left(\frac{k_3 b^2}{k_p} + \frac{4 \Omega^2 m_p}{3 k_p} + \frac{4 k_1}{3 k_p} + \frac{4 \theta^2 \Omega^2 R^2 C^S}{3 k_p^2 \left((C^S \Omega R)^2 + 1 \right)} \right) m_a}{m_p} \right) c_a \right. \right. \\
& \left. \left. + \frac{k_3 b^2}{k_p} + \frac{4 k_1}{3 k_p} + \frac{4 \theta^2 \Omega^2 R^2 C^S}{3 k_p^2 \left((C^S \Omega R)^2 + 1 \right)} \right) \right)
\end{aligned}
\tag{A.3}$$

$$\begin{aligned}
\frac{d}{dt}\beta(t) = & \frac{1}{2} \frac{1}{\frac{4m_a^2\Omega^2}{m_p k_p} + \frac{c_a^2}{m_p k_p}} + \left(\frac{4m_a a \left(\frac{m_a}{m_p} - \frac{1}{2} \frac{c_p c_a}{m_p k_p} \right) \Omega \cos(\alpha - \beta)}{m_p \sqrt{\frac{k_p}{m_p}}} \right. \\
& + \frac{4m_a a \left(\frac{m_a \Omega^2 c_p}{m_p^2 \left(\frac{k_p}{m_p} \right)^{3/2}} + \frac{1}{2} \frac{c_a}{m_p \sqrt{\frac{k_p}{m_p}}} \right) \sin(\alpha - \beta)}{m_p} \\
& + \frac{1}{\sqrt{\frac{k_p}{m_p}}} \left(3\Omega b + \frac{\left(\frac{4 k_1}{3 k_p} + \frac{4}{3} \frac{\theta^2 \Omega^2 R^2 C^S}{k_p^2 \left((C^S \Omega R)^2 + 1 \right)} + \frac{k_3 b^2}{k_p} - \frac{4 \Omega^2 m_p}{3 k_p} \right) m_a^2}{m_p^2} \right. \\
& \left. + \frac{\left(\frac{k_3 b^2}{k_p} + \frac{4 k_1}{3 k_p} + \frac{4}{3} \frac{\theta^2 \Omega^2 R^2 C^S}{k_p^2 \left((C^S \Omega R)^2 + 1 \right)} - \frac{2 c_a^2}{3 m_p k_p} \right) m_a}{m_p} \right. \\
& \left. - \frac{2 c_a^2}{3 m_p k_p} \right)
\end{aligned}$$

(A.4)